

Effects of layering on the mechanical properties of cemented tailings backfill  
under unconfined compression

By

Nhleko Monique Chiloane

submitted in accordance with the requirements for the degree of

DOCTOR OF PHILOSOPHY

in the subject

MINING ENGINEERING

at the

UNIVERSITY OF SOUTH AFRICA

Supervisor: Prof Francois Mulenga

Co-Supervisor: Dr Fhatuwani Sengani

December 2022

## DECLARATION

Name: Nhleko Monique Chiloane

Student number: 11661895

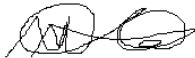
Degree: Doctor of Philosophy

Effects of layering on the mechanical properties of cemented tailings backfill under unconfined compression.

I declare that the above thesis is my own work and that all the sources that I have used or quoted have been indicated and acknowledged by means of complete references.

I further declare that I submitted the thesis to originality checking software and that it falls within the accepted requirements for originality.

I further declare that I have not previously submitted this work, or part of it, for examination at Unisa for another qualification or at any other higher education institution.



---

SIGNATURE

**13/01/2023**

---

DATE

## ABSTRACT

This study investigated the mechanical behaviour of layered cemented tailings backfill. Indeed, paste backfill in low stopes can be poured completely at once. However, this strategy is difficult in large stopes since it exerts excessive pressure on the barricade leading to the failure of the barricade. As result, layer-by-layer backfilling poured within a 24-hour interval is adopted. This practice leads to the stratification of the backfill structure which then results in a layered backfill body. Several studies on backfill bodies have neglected the effect of layering on the mechanical strength of the backfill structures. This study attempted to close this gap by incorporating the shear force between the layers in the estimation of the safety factor of the backfill structure.

In order to study the mechanical behaviour of layered cemented backfill, laboratory tests, numerical simulations and mathematical modelling were conducted. Uniaxial compressive strength tests were performed using an unconfined compression machine. The OPTUM G3 software package, on the other hand, was utilised for numerical analysis. The limit equilibrium wedge solution was used to evaluate the stability of layered cemented backfill while results from the laboratory tests were used to develop a deformation model of layered cemented backfill.

It was concluded from the deformation model that the strength of cemented backfill decreases with increasing layers of backfill at early age (14 days). Nonetheless, the strength of layered cemented backfill gradually increases when more layers are added. The limit equilibrium solution was also improved by incorporating the shear forces acting along the backfill-backfill interfaces and the sliding plane. The limit equilibrium solution also demonstrated a decreasing safety factor when the shear force along the backfill interfaces is included. In contrast, the safety factor decreased with increasing stope height. It is however recommended in future that advanced numerical analysis is explored to develop stability graphs that would predict the waiting period for the backfill body to set till the next blast. This would pave the way for improved safety and productivity of mines.

Keywords: Cemented tailings backfill, backfilled stope stability, layered backfill, UCS

## DEDICATION

Ndza khensa Nghala ya Judah

## ACKNOWLEDGEMENT

First and foremost, I would like to give all the glory to God, the Sovereign King for the strength, endurance, and ability He has given me to complete my thesis.

I also would like to thank my supervisor and co-supervisor, Professor Francois Mulenga and Dr Fhatuwani Sengani, for their splendid and magnificent guidance throughout the trajectory of my studies. May God continue to shower you with wisdom, knowledge, and understanding.

Moreover, I am very grateful for the financial support from the University of South Africa. The findings reported in this study were made possible by their financial support. I would also like to acknowledge the donation of cements provided by AfriSam, the donation made the experimental exercise of this study possible.

Not forgetting my wonderful husband, Mpho Chiloane, thank you for the endless support you always give me tirelessly. You were literally my strength in my entire study, it is your prayers that brought light and hope in the midst of difficulties.

Finally, I would like to acknowledge the assistance provided by Mr Thabelo Sivhe, for being my mathematical tutor even after hours. I am grateful for your assistance.

# TABLE OF CONTENTS

DECLARATION .....	i
ABSTRACT .....	ii
DEDICATION .....	iii
ACKNOWLEDGEMENT .....	iv
LIST OF FIGURES .....	ix
LIST OF TABLES .....	xiii
LIST OF SYMBOLS.....	xiv
LIST OF PUBLICATIONS .....	xvii
Chapter 1 Introduction.....	1
1.1 Context of the research .....	1
1.2 Problem statement .....	3
1.3 Research objectives .....	3
1.4 Contribution to the body of knowledge.....	4
1.5 Structure of the thesis.....	4
Chapter 2 Literature review.....	6
2.1 Overview of cemented tailings backfill .....	6
2.2 Rheological properties of cemented tailings backfill.....	8
2.3 Physical properties of cemented tailings backfill.....	10
2.4 Hydraulic properties of cemented tailings backfill.....	13
2.5 Thermal properties of cemented tailings backfill .....	14
2.6 Chemical properties of cemented tailings backfill.....	15
2.7 Mechanical properties of cemented tailings backfill .....	16
2.8 Effects of internal factors on the strength of cemented backfill.....	20
2.8.1 Effects of particle size distribution.....	20
2.8.2 Effects of mineral composition .....	21
2.8.3 Effects of binder-to-tailing ratio .....	24
2.8.4 Effects of moisture content, porosity and saturation.....	25
2.8.5 Effects of chemical admixtures .....	28
2.8.6 Effects of binder hydration .....	30
2.9 Effect of external factors on the strength of cemented backfill .....	31
2.9.1 Effects of curing conditions.....	31
2.9.2 Effects of stope layout/dimensions.....	33
2.9.3 Closing remarks.....	35
2.10 Stability analysis of backfilling body .....	35
2.10.1 Vertical exposed stopes.....	36

2.10.2	Limit Equilibrium Wedge model .....	37
2.10.3	Stability charts for open stope design .....	43
2.10.4	Modified Mathews stability charts .....	46
2.10.5	Dilution-based stability graph.....	50
2.10.6	Numerical methods.....	52
2.11	Successful and failures of backfill stopes – Case studies .....	54
2.12	Closing comments .....	55
2.13	Summary and future work.....	56
Chapter 3	Data collection procedure and research methodology used.....	58
3.1	Introduction.....	58
3.2	In-situ collection of the bulk tailings sample .....	59
3.3	Laboratory experiments.....	60
3.3.1	Particle size distribution .....	60
3.3.2	Atterberg's limits.....	62
3.3.3	X-Ray fluorescence spectrometer.....	64
3.3.4	Slump tests.....	64
3.3.5	Mixing and curing procedure.....	66
3.3.6	Mechanical compression tests.....	68
3.4	Development of simulation model.....	69
3.4.1	Meshing.....	70
3.4.2	Properties of the rock mass and backfill material .....	71
3.4.3	Initial stresses around the stope .....	72
3.4.4	Backfilling process.....	72
3.5	Challenges encountered with the experimental tests .....	73
Chapter 4	Effects of cement-to-tailings ratio and layering on the compressive strength of cemented tailings backfill. ....	75
4.1	Introduction.....	75
4.2	Particle size distribution of the tailings material collected .....	76
4.3	Atterberg's attributes of the tailings material .....	77
4.4	Mineral composition of the tailings material .....	80
4.5	Results of the slump tests.....	81
4.6	Mechanical properties of the CTB samples.....	81
4.6.1	Effect of curing time on the compressive strength and elastic modulus of CTB samples.....	82
4.6.2	Effect of binder content on the performance of CTB samples .....	84
4.6.3	Effect of layering on the performance of CTB samples .....	85

4.7	Significance of the findings .....	87
4.8	Conclusion.....	88
Chapter 5	Development of deformations model on the mechanical performance of layered backfill support system. ....	89
5.1	Introduction.....	89
5.2	Correlating the mechanical properties, curing time, binder content and layering of CTB cubes .....	89
5.2.1	Effect of curing time on the performance of CTB cubes .....	89
5.2.2	Effect of layering on the performance of CTB cubes .....	92
5.3	Development of a damage constitutive model for layered CTB.....	95
5.4	Determination of the parameters of the damage constitutive model.....	97
5.5	Validation of the constitutive model.....	98
5.6	Concluding remarks.....	101
Chapter 6	Developing stress distribution charts in the vicinity of layered and unlayered backfill stopes.....	102
6.1	Introduction.....	102
6.2	Governing equations for Mohr-Coulomb elastoplastic model .....	102
6.3	Results and discussions .....	105
6.3.1	Case 1: Open stope.....	105
6.3.2	Case 2: Non-layered backfilled stope .....	106
6.3.3	Case 3: Double layered backfilling.....	108
6.3.4	Case 4: Three-layered backfilling .....	109
6.3.5	Case 5: Four-layered backfilling .....	111
6.4	Deformation curves .....	112
6.5	Conclusion and future outlook .....	115
Chapter 7	Development of an analytical solution to assess the stability of exposed vertical layered backfill. ....	117
7.1	Introduction.....	117
7.2	Development of the proposed solution.....	118
7.3	Validation of analytical solution.....	121
7.4	Final remarks.....	126
Chapter 8	Conclusions and recommendations .....	128
8.1	Summary of the thesis .....	128
8.1.1	Laboratory experiments .....	129
8.1.2	Numerical modelling .....	129
8.1.3	Development of a damage model .....	130
8.1.4	Analytical solution for vertical exposed backfilled stope .....	130



8.2	Conclusion of the thesis.....	131
8.3	Recommendations for future work .....	132
	List of references .....	133
	APPENDICES .....	155
	Appendix A: Ethical clearance certificate .....	155
	Appendix B: Sample of calculations from Chapter 7 .....	156
	Appendix C Laboratory results.....	156
	Appendix D Data for the damage model .....	158
	Appendix E Numerical analysis data for stress-strain graph .....	159
	Appendix F Solution to Equation (5.20).....	159

## LIST OF FIGURES

Figure 2.1 (a) Effect of OPC on the strength of CTB overtime with different dosages, and (b) Effect of sodium silicate-activated neutral slag (NS-LSS) on the strength of CTB overtime with different dosages.....	7
Figure 2.2 Plasticity chart where C: clay; M: silt; L: low plasticity, I: intermediate plasticity, H: high plasticity, V; very high plasticity and E: extremely high plasticity .....	11
Figure 2.3 Particle size distribution curves for poorly and well-graded backfill material.....	12
Figure 2.4 A typical XRD chart showing the mineral composition of certain tailings .....	15
Figure 2.5 Stress-strain curve of CTB samples.....	16
Figure 2.6 Stress-strain curves of CTBs at 28 curing days for mixtures T2 (no fibre), T6 (No fibre), T2 (PP fibre) and T6 (PP fibre).....	18
Figure 2.7 Failure modes of CTB under various stages of the elastoplastic and post-rupture zones.....	19
Figure 2.8 Effect of initial sulphate content on the strength of CTB at an early age .....	22
Figure 2.9 Comparison of UCS values for sulphate-treated and sulphate-free CTBs .....	23
Figure 2.10 Relationship between UCS and sulphate content for CEM II/A-P pozzolan (C2) and CEM IV/A (C4) cements.....	24
Figure 2.11 Relationship between porosity and UCS for CTB .....	26
Figure 2.12 Relationship between UCS and water saturation for fly ash concrete .....	27
Figure 2.13 Relationship between UCS and water saturation for CTB material..	27
Figure 2.14 Strength evolution of CTB specimens with different poly naphthalene sulfonate dosages.....	30
Figure 2.15 Relationship between temperature and UCS of CTB .....	33
Figure 2.16 Side exposed backfill body during secondary stope extraction.....	36
Figure 2.17 Wedge block mechanism proposed by Mitchell et al. (1982).....	38
Figure 2.18 Backfill with a high height-to-width ratio containing plug pour at its base, when the sliding plane (a) remains within the plug, and (b) intersects the top surface of the plug .....	40

Figure 2.19 Mathews stability chart showing the three stability zones .....	44
Figure 2.20 Graphical determination of stress factor $A$ .....	45
Figure 2.21 Graphical determination of joint orientation factor $B$ .....	45
Figure 2.22 Graphical determination of gravity adjustment factor $C$ .....	46
Figure 2.23 Modified stability graph by Potvin using the modified stability number .....	47
Figure 2.24 Stability graph incorporating cable bolt.....	48
Figure 2.25 Modified stability chart .....	48
Figure 2.26 Modified stability graph .....	49
Figure 2.27 Extended Mathews stability graph.....	50
Figure 2.28 ELOS lines superimposed on the Potvin-Nickson graph .....	52
Figure 2.29 Vertical stress distribution contours within backfill and surrounding rocks.....	54
Figure 3.1 Location of tailing dumps where the samples were collected .....	59
Figure 3.2 (a) Collecting tailings samples; and (b) Samples stored in refuse bags .....	60
Figure 3.3 (a) Tailings placed in an oven for overnight drying; and (b) Putting tailings in a stack of sieves .....	61
Figure 3.4 (Left) Equipment used for the limit liquid test: (a) water bottle, (b) mixing bowl, (c) spatula, (d) weighing scale (e) Casagrande's cup. (Right) Tailings sample is split at the centre to observe the closing gap when tapping.....	62
Figure 3.5 Rolling of ellipsoidal paste for determining plastic index.....	64
Figure 3.6 (a) Equipment required for a slump test procedure; (b) Performing a slump test .....	65
Figure 3.7 (a) A concrete mixer used to mix CTB slurry; (b) Casting CTB slurry into a cubic mould .....	67
Figure 3.8 Step by step procedure from mixing the backfill to testing compressive strength .....	68
Figure 3.9 Illustration of the backfill modelling process .....	73
Figure 4.1 Gradation curve of the collected tailing sample .....	77
Figure 4.2 Liquid limit (moisture content) corresponding to 25 taps .....	78
Figure 4.3 Plasticity index chart to classify tailings type .....	79
Figure 4.4 Effects of binder content on the strength of CTB samples for various binder contents .....	85

Figure 4.5 Effect of layering on the UCS values of CTB specimens for 2.5 c/t, 2.3 c/t and 2.1 c/t mix ratios .....	86
Figure 5.1 Effect of curing on the uniaxial compressive strength at 2.5c/t mix ratio for three-layered CTB samples .....	90
Figure 5.2 Effect of curing time on elastic modulus at 2.5c/t mix ratio for three-layered CTB samples .....	91
Figure 5.3 Correlation between UCS values and the layering of cemented tailings backfill samples .....	93
Figure 5.4 Effect of layering on the elastic modulus of CTB specimens for 2.5 c/t .....	94
Figure 5.5 Comparison of the theoretical and experimental UCS values of CTB samples after 7 curing days .....	98
Figure 5.6 Comparison of the theoretical and experimental UCS values of CTB specimens after 14 curing days .....	99
Figure 5.7 Comparison of the theoretical and experimental UCS values of the CTB samples after 21 curing days .....	100
Figure 5.8 Comparison of the theoretical and experimental UCS values of the CTB samples after 28 curing days .....	100
Figure 5.9 The evolution of the damage/deformation of CTB with layering.....	101
Figure 6.1 The theoretical Mohr-coulomb elastoplastic model: (a) Yield surface in the mean (p) and deviatoric (q) stress space; and (b) Stress-strain curve.....	103
Figure 6.2 Distribution of the major principal stress ( $\sigma_1$ ) in the open stope .....	106
Figure 6.3 Distribution of the major principal stress ( $\sigma_1$ ), major strain stress ( $\epsilon_1$ ), and shear dissipation in a non-layered backfilled stope .....	107
Figure 6.4 Displacement of the backfilled stope in the x-, y- and z-directions...	108
Figure 6.5 Distribution of the major principal stress ( $\sigma_1$ ), major strain stress ( $\epsilon_1$ ), and shear dissipation in a two-layered backfilled stope.....	109
Figure 6.6 Displacement of the two-layered backfilled stope in the x-, y- and z-directions respectively .....	109
Figure 6.7 Distribution of major principal stress ( $\sigma_1$ ), major strain stress ( $\epsilon_1$ ), and shear dissipation in a three-layered backfilled stope .....	110
Figure 6.8 Displacement of the three-layered backfilled stope in the x-, y- and z-directions respectively .....	110
Figure 6.9 Distribution of major principal stress ( $\sigma_1$ ), major strain stress ( $\epsilon_1$ ), and shear dissipation in a three-layered backfilled stope .....	111

Figure 6.10 Displacement of the four-layered backfilled stope in the x-, y- and z- directions respectively .....	112
Figure 6.11 Stress vs strain curves for layered backfill.....	114
Figure 7.1 Decomposition of the forces acting on the layered backfill model ...	118
Figure 7.2 Variation of safety factor with overload pressure. Calculations done with $c = 80$ kPa, $H = 40$ m, $L = 10$ m $\gamma = 18$ kPa, $r_s = 0.5$ . .....	122
Figure 7.3 Variation of safety factor with stope height. Calculations done with $c = 80$ kPa, $L = 10$ m, $\gamma = 18$ kPa, $r_s = 0.5$ .....	123
Figure 7.4 Variation of FoS with different values of cohesion.....	124
Figure 7.5 Variation of safety factor with different values of adherence ratio $r_s$ . Calculations done with $c = 80$ kPa, $H = 40$ m, $\gamma = 18$ kPa, $r_s = 0.5$ , $\phi = \delta = 30^\circ$ . .....	125
Figure 7.6 Variation of safety factor with the number of layers. Calculations done with $c = 80$ kPa, $H = 40$ m, $\gamma = 18$ kPa, $r_s = 0.5$ . .....	126

## LIST OF TABLES

Table 3.1 Number of CTB specimens made per mixture design .....	67
Table 3.2 System requirements of OPTUM G3.....	69
Table 3.3 Properties of the rock mass used in the numerical modelling .....	71
Table 3.4 Properties of the backfill material used in the numerical modelling ....	72
Table 4.1 Mass fractions of tailings particles retained in different sieves.....	76
Table 4.2 Data recorded from Atterberg's tests.....	78
Table 4.3 Data recorded from the liquid limit tests .....	79
Table 4.4 Mineral composition of the tailings material by XRD analysis .....	80
Table 4.5 Slump test results .....	81
Table 4.6 Uniaxial compressive strength [in MPa] of CTB samples for different combinations of cement-to-tailings ratios, curing periods, and layering structures .....	82
Table 4.7 Elastic modulus [in MPa] of CTB samples for different combinations of cement-to-tailings ratios, curing periods, and layering structures .....	83
Table 5.1 The fitting and determinant coefficients associated with curing time and UCS of CTB of different combinations of c/t ratios and different layering patterns. ....	90
Table 5.2 The fitting and determinant coefficients associated with curing time and elastic modulus of CTB of different combinations of c/t ratios and different layering patterns .....	92
Table 5.3 The fitting coefficients associated with layering and UCS of CTB samples from 7-28 days of curing. ....	93
Table 5.4 The fitting coefficients associated with layering and elastic modulus of CTB samples from 7-28 days of curing. ....	95

## LIST OF SYMBOLS

$A$	Stress factor
$\alpha$	Angle between the wedge sliding and horizontal planes
$\alpha_p$	Parameter of the Drucker-Prager criterion
$a; b$	Fitting coefficients
$B$	Thickness of backfill stope
$B_1$	Joint orientation factor
$C_1$	Gravity factor
$c$	Cohesion of the backfill
$c'$	Adherence cohesion along with the interfaces between the backfill and the side walls
$C_u$	Coefficient of uniformity
$C_c$	Coefficient of curvature
$d$	Fitting coefficient associated with elastic modulus and layering
$E$	Elastic modulus
$\varepsilon$	Strain
$FoS$	Factor of safety
$f; k$	Fitting parameters associated with curing time and compressive strength
$g$	Gravity acceleration ( $m/s^2$ )
$h$	Depth from the top of the backfill
$H$	Overall height of exposed backfill
$H^*$	Height of wedge block
$H_s$	Elevation from the bottom of the plug pour to the line of intersection between the wedge and the sliding plane

$H_p$	Thickness of the plug pour
$H_f$	Thickness of the final pour
$I_1$	First stress invariant
$J_\eta$	Joint set number
$J_r$	Joint roughness number
$J_a$	Joint alteration number
$J_2$	Second invariant of the deviatoric stress tensor
$K = K_0$	Ground pressure co-efficient
$k_p$	Material parameter of the Drucker-Prager criterion
$L$	Length of the backfill
$LL$	Liquid limit
$MC$	Moisture content
$m$	Fittings coefficient associated with the compressive strength and layering
$n$	Flow index
$\eta$	Plastic viscosity coefficient
$N'$	Stability number
$N$	Number of taps
$n$	Number of layers
$p$	Mean stress
$PL$	Plastic limit
$PI$	Plastic index
$P_0$	Surcharge pressure
$q$	Deviatoric stress
$Q$	Plastic potential



$R^2$	Coefficient of determination
$RQD$	Rock quality designation
$S$	Shape factor / hydraulic radius
$t$	Curing period
$W$	Width of backfill
$W_n$	Net weight of sliding block
$w$	Fitting coefficient associated with elastic modulus and layering.
$X$	Shear rate
$z$	Fitting coefficient associated with UCS and layering
$\sigma_1, \sigma_2, \text{ and } \sigma_3$	Major, intermediate, and minor principal stresses
$\sigma_i$	Initial stress state
$\lambda$	Plastic multiplier
$\delta$	Friction angle of rock mass
$\tau_0$	Yield stress
$\gamma$	Unit weight
$\sigma$	Stress
$\sigma_v$	Vertical stress
$\phi$	Friction angle of backfill.
$\tau_s$	Shear strength along backfill-ROCK side walls
$\tau_a$	Shear strength along backfill-ROCK back wall
$r_p$	Interface adherence ratio of plug pour
$r_{ip}$	Interface adherence ratio of plug with side walls
$r_{if}$	Interface adherence ratio of final pour with sidewall
$n$	Flow index

## LIST OF PUBLICATIONS

Chiloane, N.M., Mulenga, F.K., 2023. Revisiting factors contributing to the strength of cemented backfill support system: A review. *Journal of Rock Mechanics and Geotechnical Engineering*, vol. 15, no. 6, pp. 1615 – 1624

Chiloane, N.M., Sengani, F., Mulenga, F.K., 2023. An experimental and numerical study of the strength development of layered cemented tailings backfill. *Construction and Building Materials*, under review

Chiloane, N.M., Sengani, F., Mulenga, F.K., 2023. Extension of analytical solution methods to the stability of exposed stratified cemented backfills. *International Journal of Rock Mechanics and Mining Science*, under review

Chiloane, N.M., Sengani, F., Mulenga, F.K., 2023. Deformation characteristics and damage constitutive model of layered cemented tailings backfill. *Rock Mechanics and Rock Engineering*, under review

# Chapter 1 Introduction

## 1.1 Context of the research

The mineral processing plant generates large volumes of tailings which then pose a threat to the environment if not disposed of appropriately. Furthermore, to alleviate this environmental problem, the mining industry has adopted the strategy of disposing of mine tailings in underground mined voids through backfill (Benzaanzoua et al., 2004; Nasir and Fall 2010; Yilmaz et al., 2009). It is in this light that cemented tailings backfill (CTB) has gained popularity as an underground backfill support system. Once the CTB is placed in underground stopes, its key role is to maintain the stability of adjacent stopes being mined (Zhao, 2021). Several authors have developed stability methods and graphs to analyse backfilled stopes and CTB design. The sliding wedge failure by Mitchell et al. (1982) is one such well-known method. It allows one to determine the required strength of backfill that would stabilise a certain stope. Although widely used, the method by Mitchell et al. (1982) has undergone several modifications by Aubertin (2003), Li et al. (2003), and Wang et al. (2021) among others. This has been done mostly to address the limited ability of the method to guide the design of CTBs.

The design and mechanical strength of a CTB are of paramount importance considering its primary application in underground mines. Indeed, CTB has commonly been used as a secondary or tertiary support system in open stopes and other massive mining methods. Qin et al. (2021) explained that a backfill support system is preferred as it leads to increased ore recovery and reduced dilution across the mining stope. Furthermore, CTB is one viable mechanism that can be used to reduce the surface area needed for tailings disposal (Yang et al., 2020) as well as surface pollution and surface subsidence (Ercikdi et al., 2017). It is because of the above benefits that several experimental studies have been conducted to evaluate the mechanical strength of CTB and optimise its design. In one such study, Chen et al. (2020) examined the change in uniaxial compressive strength (UCS) of CTB with time. Their results showed a notable increase in the development of UCS from 0.2 MPa to 4 MPa after 28 days. Concordant studies have also reported similar observations, see for example Benzaazoua and Belem (2008), Nasir and Fall (2010), and Zhou et al. (2019). It can therefore be argued

that the adequate design of CTB is mainly dictated by its UCS which in turn enables one to perform affordable, reliable and simple UCS tests when studying CTB. This understanding has led to numerous studies on CTB in view to identify the factors that contribute largely toward its increased strength. Zheng et al. (2018) for example found that the UCS of CTB increases with the content in ordinary Portland cement. Shunman et al. (2021), on the other hand, reported an increase in UCS when both curing stress and curing temperature were increased. For this reason, they recommend that curing stress and curing temperature must be incorporated into the design of CTB. However, caution needs to be exercised as Xu et al. (2019b) have reported that high curing temperatures promote the cement hydration reaction with dire consequences on the strength of CTB. That is why scholars such as Shunman et al. (2021) argue that more experimental validation is still needed for a way forward.

The other important factor determining CTB strength is the size of the stope to be supported. The size of stopes may vary in height or width from high to narrow and wide depending on the rock mass stability. For large (high) stope, it is impossible to complete the filling process all at once (Xu et al., 2019a). Doing so would result in high hydrostatic pressure on the barricade thereby increasing the risk of failure.

According to Cao et al. (2018), mines generally adopt a strategy whereby backfilling is performed in two stages: a plug pour and a final pour to alleviate the pressures on the barricade. Thus, a large-scale stope should be backfilled gradually and at regular intervals; this results in the layering of CTB with consequences that are yet to be clarified. The present doctoral study, therefore, seeks to investigate the effect of layering on the mechanical strength of CTB. The findings are expected to contribute towards addressing the paucity of analytical solutions and stability graphs for layered stope supports. Most importantly, layering can be incorporated in CTB design since mining stopes vary in shape and size.

To achieve the above, laboratory tests were conducted to test the mechanical strength of non-layered and layered CTB samples under compressive loading. Samples were cured at a constant temperature and humidity and tested for uniaxial compressive strength (UCS). Results were then used to develop stability graphs and deformation curves for the CTB design tested. Complementary numerical simulations were also carried out for the purpose of better understanding the expected behaviour of the CTB in an underground environment.

## 1.2 Problem statement

Cemented tailings backfill (CTB) has become common practice in the management of tailings generated by underground mining operations. CTB is placed in open stopes mainly to control ground convergence and surface subsidence (Fu et al., 2020). Once placed underground, the CTB is expected to maintain its mechanical stability while providing support to surrounding excavations and a safe working environment for mine workers (Wu et al., 2018; Zhao, 2021). And when mining the adjacent stope, the exposed backfill wall must remain stable; otherwise, it might fall into the recently blasted stope and cause dilution. The problem is that currently available guidelines (see for example Mitchell et al., 1982; Li, 2014a) as well as Mathew's stability graphs (Mathews et al., 1981) cannot be used to predict the stability of layered CTB. They may provide inaccurate predictions since they were developed and intended for uniform and homogenous backfill bodies (Wang et al., 2021).

The problem is compounded by the fact that stopes exist in various sizes and shapes depending on the mining layout and method used. In the case of large underground stopes, it is a logistical challenge to backfill at once; instead, this is done in gradual and successive sequences. As a result, the CTB pillar appears stratified (Fu et al., 2020; Wang et al., 2019; Xu et al., 2019a) essentially altering its mechanical properties and failure mode. Indeed, Wang et al. (2019) support that the mechanical properties of single-layered backfill and multi-layered backfill differ. It is thus important to study the strength of CTB as stope height increases and understand better the stress distribution within layered backfill.

## 1.3 Research objectives

The main objective of this study is to investigate the effect of layering on the stability of large backfill bodies. As stated earlier, mining stopes vary in size from narrow to wide to large with the latter being difficult to backfill continuously and at once. Instead, large stopes are backfilled in successive layers from the bottom up. The number of layers, therefore, increase with stope height which then results in a layered or stratified backfill structure. It is the effects of this layering on the mechanical performance of cemented backfill that the doctoral aims to investigate.

To achieve this goal, specific objectives are set as follows:

- determine the selected properties (chemical composition, particle size distribution) of the tailings obtained;
- determine unconfined compressive strength of Cemented Tailings Backfill (CTB) cube produced in the laboratory;
- develop a constitutive damage model that characterizes the mechanical properties of a layered backfill support system;
- develop deformations curves on the mechanical performance of layered backfill support system; and
- develop an analytical solution capable of appraising the stability of vertically exposed and layered backfilled stope.

#### 1.4 Contribution to the body of knowledge

In a recent review, Zhang et al. (2022) highlight the fact that the systematic study of the mechanical behaviour and failure characteristics of layered CTB is relatively rare yet needed. This doctoral study, therefore, seek to close the gap by refining existing predictive models and solutions for the stability of CTB to allow for the layering effect. The current solutions by Mitchell et al. (1982), Li (2014b) and Li and Aubertin (2014) amongst others neglect the effects of the shearing force existing along the interfaces between the backfill layers. Furthermore, their solutions do not consider the multiple layers existing in the backfill structure, which further exacerbates the shearing force. This result in the overestimation of the stability of underground backfill structures. Therefore, this thesis aims to incorporate the shearing force existing within the backfill layers to further investigate the change in the safety factor of the backfill with increasing backfill layers. When this is achieved, mines using large-scale mining methods will be able to design safe backfilled stopes and reduce dilution and associated operational costs.

#### 1.5 Structure of the thesis

The present chapter of the doctoral thesis introduces the research problem and objectives. It also outlines the envisaged contribution of the research study. Chapter 2 then reviews previous research that has been conducted in the area of backfilling. The review covers the properties of CTB and the various factors

contributing to the strength of CTB. Empirical and analytical methods used to analyse the stability of CTB structures are also discussed. Lastly, the chapter concludes by identifying the knowledge gap which this study aims to address.

Chapter 3 explains the research methods used to collect empirical data in line with the objectives set out for the doctoral thesis. Procedures and protocols used in measuring the physical properties of the backfilling material such as particle size analysis and the Atterberg limits are presented. The experimental method applied to prepare, cure and test CTB samples are also described. The challenges and limitations of the experimental protocols are identified and succinctly discussed.

Chapter 4 covers the analysis of the experimental data collected in the laboratory. Particle size distributions, plasticity index, and mechanical properties of CTB (including UCS, stress-strain curves, and elastic modulus) are also presented.

Chapter 5 discusses the process followed to develop a constitutive damage model capable of predicting the strength of layered backfill support. The damage model is based on the empirical regression model developed from the data obtained from laboratory experiments.

Chapter 6 provides a detailed description of the numerical model developed to analyse the stress distribution within a layered backfilled stope. The chapter further presents the deformation curves developed from the results of the numerical model carried out on a typical stope.

Chapter 7 outlines the procedure followed to develop the mathematical solution used to assess the stability of exposed layered backfilled stope. The use of the solution is further demonstrated by drafting a predictive graph of the safety factor of backfilled stopes.

Chapter 8 concludes the thesis by summarising the main findings as well as the recommendations for future work.

## Chapter 2 Literature review

This chapter discusses the characteristics of CTB and how these are factored into the analysis of the stability of backfill walls. Firstly, a brief introduction to CTB, its mixture design, and its use in underground mining are covered. Secondly, the chapter explores the physical, hydraulic, chemical and mechanical properties of CTB and how they influence its behaviour. Then, factors including binder-tailing ratio, water content, mineral admixtures, consolidation, and stope geometry are discussed in terms of their individual effects on the strength of CTB. Lastly, the application of analytical and numerical methods to analyse the stability of CTB is reviewed from previous studies.

### 2.1 Overview of cemented tailings backfill

Mine tailings are generated during the processing of the extracted minerals in the processing plant (Fall et al., 2008). A major concern for the mining industry is their safe disposal to prevent environmental pollution (Qi et al., 2018). It is for this reason that mine tailings are used as backfill in underground open stopes. Cemented tailings backfill (CTB) is the most widely used for backfilling. CTB is usually made of dewatered tailings (70 – 85% by weight), a hydraulic binder (3 – 7%) and mixing water (Kesimal et al., 2005). It is delivered into underground workings as a slurry using pipeline reticulation infrastructure (Rankine, 2004). CTB provides several benefits including safe disposal of mine tailings, improved ground support, ore recovery, and reduced rehabilitation costs (Jahanbakhshzadeh et al., 2018; Qi et al., 2018; Xu et al., 2020). These benefits amongst others have resulted in the worldwide use of CTB technology (Kesimal et al., 2005; Chen et al., 2019; Cui and Fall, 2016; Lu et al., 2018; Fu et al., 2019; Wang et al., 2020a; Zhang et al., 2022).

According to Benzaanzoua et al. (1999), backfill is usually mixed with hydraulic cement. Acting as a binding agent, the hydraulic cement may involve ordinary Portland cement (OPC), fly ash, blast-furnace slag, or a combination of these. The main purpose of these binders is to augment the mechanical strength of backfill (Kesimal et al., 2005). Some binding agents are not only used for strength gain but also to resist sulphate attack. For example, Ercikdi et al. (2009) conducted an experimental study to determine the effect of binder type on sulphide-rich CTB.



They used ordinary Portland cement (OPC), Portland composite cement (PCC), sulphate-resistant cement (SRC) and a 50:50 mixture of OPC and SRC as binding agents. The binder dosage was kept at a constant of 5% for all types of binders considered. Results showed that all samples had developed strength after 28 days of curing. However, only OPC samples had acquired the required UCS > 0.7 MPa. Interestingly, after 56 days, the OPC and PCC samples started to show a drop in strength while SRC and SRC/OPC mixture samples maintained their strength development. These findings suggest that OPC and PCC are not suitable binders for sulphide-rich tailings unless used in high dosages to meet the strength requirements. It should also be noted that OPC is rich in Calcium (Ca) and is hence vulnerable to acid and sulphate attacks (further detail in Section 2.8.3). Cihangir et al. (2012) tested and compared sulphide-rich CTB samples prepared with different binders; namely, OPC and alkali-activated blast furnace slags at different dosages (5 – 7 wt.%). Loss in strength in OPC CTB samples was observed after 56 curing days. The decrease was reported to be of the order of 42.65%, 12.61% and 5.52% at 5 wt.%, 6 wt.% and 7 wt.% binder dosages respectively. In contrast, alkali-activated slag (AAS) binders demonstrated remarkably high strength at longer curing days (i.e., after 360 days) compared to OPC samples. In addition to this, no strength loss was recorded for AAS binders. Cihangir et al. (2012) attributed this to the ability of AAS binders to resist sulphate attack and to their low content of calcium oxide (CaO). The difference in strength performance of CTB samples made of OPC and alkali-activated slags is illustrated in Figure 2.1.

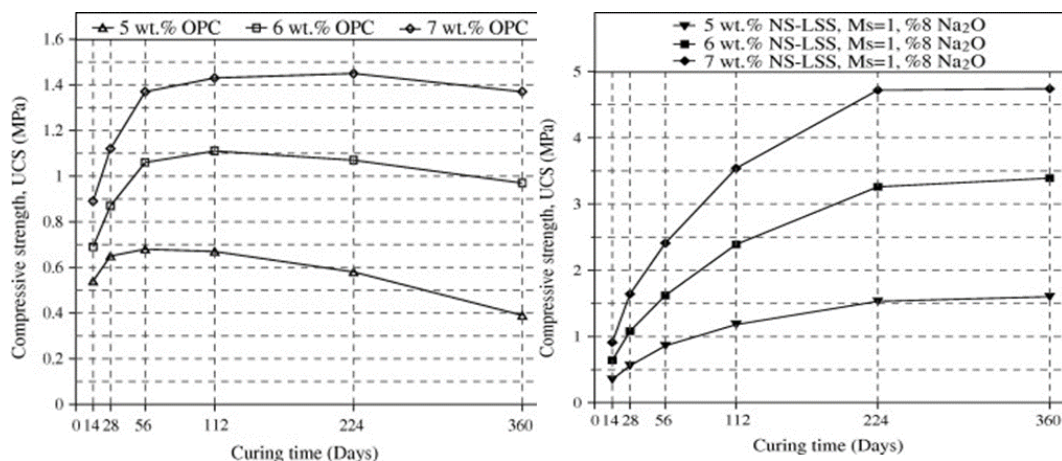


Figure 2.1 (a) Effect of OPC on the strength of CTB overtime with different dosages, and (b) Effect of sodium silicate-activated neutral slag (NS-LSS) on the strength of CTB overtime with different dosages (after Cihangir et al., 2012)

Du et al. (2021) also studied the effect of binder types using red mud, Portland cement and slag cement (mixed with fly ash). From the UCS tests, slag cement exhibited higher strength than Portland cement. It may be argued that sulphate-resistant cement acts as a good binding agent in the preparation of CTB. Its low tricalcium aluminate ( $C_3A$ ) content reduces the formation of expansive ettringite as well as the damage to the CTB matrix. However, the use of sulphate-resistant cement is common practice in the mining industry because of its prohibitive cost (Tariq and Yanful, 2012). Moreover, to address this limitation, several researchers studied CTB designed using a mix of Portland cement and fly ash as a binder. For example, Jiang et al. (2020a) prepared CTB samples using the following OPC/slag ratios: 100% OPC (i.e., 100:0), 90:10, 80:20, 70:30, 50:50, and 20:80. The strength of CTB was noted to drop by 20%, 29%, 37%, 48% and 72% respectively as slag was gradually topped up. Jiang et al. (2020a) argued this reduction in strength to be due to the low pozzolanic reactivity of the slag. In a follow-up work, Jiang et al. (2020b) compared OPC-based and AAS-based CTBs. They reported UCS values for AAS-based CTB samples as high as 1.29 to 2.94-fold those recorded for OPC-based CTB. This is because calcium silicate hydrate gel, as the main hydration product of ASS-based CTB, greatly contributes to strength development.

It can therefore be deduced that the mechanical properties of CTB are primarily based on the mineral composition and source of its constituents. The subsequent sections present a review of the properties of CTB as well as the effects of internal and external factors on its mechanical performance.

## 2.2 Rheological properties of cemented tailings backfill

The transportability and flowability of CTB are highly dependent on its rheological properties with transportability being governed by flowability (Wu et al., 2013). Indeed, poor flowability of CTB not only affect the efficiency of pumping to stopes but can also clog pipes thereby incurring unnecessary costs to the mine. Indeed, if pipes become clogged, the transportation of CTB comes to a halt while the pipeline network must be disconnected to clear the clogs. This delays production and increases operational costs for the mine.

The rheological behaviour of CTB can be evaluated using the traditional method known as slump (Lang et al., 2015). A slump is a measure of the decline in height

when a slurry is freed from a conical mould. The slump can be used to characterize the consistency of a material which in turn can be linked to its transportability. A low-slump mix will flow less easily than a high-slump mix, even if both are produced from the same material. The true rheological properties of a slurry are difficult to acquire in practice. However, the conventional slump test is commonly used to provide a quick and simple measure of the consistency of paste backfill (Wu et al., 2013). Here, the target slump of CTB is generally between 152 and 254 mm with a high slump drop indicating the preferred rheological properties of CTB (Belem et al., 2016; Ouattara et al., 2017 & 2018).

Yield stress and viscosity are a less empirical way of describing the rheological behaviour of CTB. Ouattara et al. (2017) define yield stress as the minimum pressure required to start the flow of the material while plastic viscosity (or viscosity for short) is the frictional resistance between two layers of the fluid.

Fresh CTB slurry generally behaves like a non-Newtonian fluid; it can therefore be described by the Bingham model and the Herschel-Bulkley (H-B) model. The H-B model has better fitting capabilities of the shear rate-shear stress curve that can be produced from a CTB slurry. It is summarised below (Zhang et al., 2021):

$$\tau = \tau_0 + \eta \cdot x^n \quad (2.1)$$

where  $\tau_0$  is the yield stress [Pa]

$\eta$  is the plastic viscosity coefficient [Pa.s]

$x$  is the shear rate [ $s^{-1}$ ]

$n$  is the flow index. When  $n > 1$ , the material has the characteristic of shear thickening. With  $n < 1$ , the material is said to be shear-thinning. And for  $n = 1$ , it degenerates into the Bingham model.

Rheological properties must be known to determine the pressure gradient and flow velocity through a pipeline. Indeed, pressure gradient aid in the optimization of pumping energy consumption (Boger, 2012; Ouattara et al. 2017; Paterson, 2012). Sellegren et al. (2005) recommend a yield stress of less than 200 Pa for easy transportation of CTB. This translates into a CTB mixture of solid content below 76% (Ouattara et al., 2018).

The rheological properties of CTB are influenced by several factors including as its solid content as well as the shape, size, surface chemistry of tailing particles (Huynh et al., 2006).

Yin et al. (2012) investigated the effect of solid components on CTB rheology. Slump tests were performed on CTB samples prepared at 68%, 74%, 78%, and 80% solid content. A slight decrease in the slump was noted at solid contents below 78%. In contrast, a sharp decline in the slump was recorded when solid content exceeded 78%. In a sense, the water content dictated the consistency of the slurry.

In another study, Zhao et al. (2021) investigated the rheological properties of cement paste blended with iron tailings. Here, a decrease in both yield stress and plastic viscosity was observed as the particle size of iron tailings was increased. This is because coarser iron tailings created more voids within the fill, thus, reducing yield resistance. Another observation was that an increase in temperature had a positive effect on both yield stress and viscosity. Interestingly, Cheng et al. (2020) found that an increase in temperature led to decreased yield stress and plastic viscosity. A rise in temperature from 5°C to 50°C resulted in the yield stress changing exponentially from 145.63 GPa to 96.8 GPa. Similarly, plastic viscosity dropped linearly from 0.328 Pa.s to 0.198 Pa.s. Note that Zhao et al. (2021) used tailings from an iron ore while Chen et al. (2020) used nickel mine tailings. As such, the different properties of tailings may have contributed to the discrepancy.

### 2.3 Physical properties of cemented tailings backfill.

The performance of CTB is known to be influenced by its physical properties. These properties include void ratio (or porosity), particle size distribution, specific gravity, and Atterberg's limits to name but a few (Ghirian and Fall, 2017; Lang et al., 2015; Shunman et al., 2021). In turn, the physical properties of a mine backfill vary with the proportions of the mixed constituents (Rankine and Sivakugan, 2007; Cui, 2017). Other factors contributing to variations are preparation techniques and the properties of cement and tailings (le Roux et al., 2005). In the thesis of Cui (2017), it was found that the physical properties of mine backfill are affected by the mixture recipe. It is therefore evident that the design of CTB is unique to every mine.

The void ratio is defined as the volume of voids to the volume of solids. It is closely related to the packing density of CTB. Qiu et al. (2020) performed a wet packing test to investigate the effect of packing density on the fluidity of CTB. The void ratio of CTB decreased when highly packed tailings-cement particles were considered.

Excess water content in the CTB mixture drained because of the short average distance between the particles which resulted in lower fluidity. This finding is also supported by Wang et al. (2021) while Qiu et al. (2020) postulate that packing density may be inversely proportional to binder content.

Tests for Atterberg's limits aim at determining the water content at which the state of soil changes to another. The name is derived from the inventor of the tests, Albert Atterberg (Atterberg, 1911). The initial tests were modified by Terzaghi and Casagrande (1932) who added a Casagrande cup. The updated test is now done to determine the liquid, plastic, and shrinkage limits of soil (Niroshan et al., 2018). The liquid limit (LL) is the moisture content at which a slurry loses viscosity. The plastic limit (PL), on the other hand, is the water content at which the wet soil can be rolled without breaking into crumbs. The shrinkage limit (SL) is the moisture content at which the slurry no longer changes volume upon drying (Kamiakin, 2017).

Atterberg's limits are captured in the unified soil classification system chart in Figure 2.2. This chart is used to classify the plasticity of soil. The A-line in the chart is a boundary between two categories of soil, i.e., clay (C) and silt (M). For example, say the liquid limit of soil is 55% and the plastic limit is 35%, the chart leads to CH, which means the soil is of high plasticity with clay material.

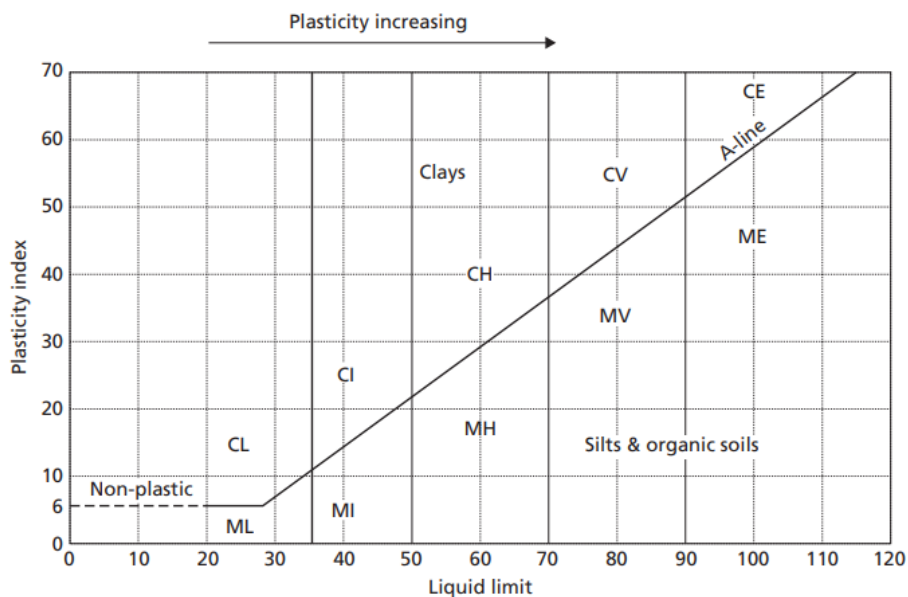


Figure 2.2 Plasticity chart where C: clay; M: silt; L: low plasticity, I: intermediate plasticity, H: high plasticity, V: very high plasticity and E: extremely high plasticity (after Craig, 2004)

From the perspective of CTB performance, the plasticity of tailings affects the strength of the fill. To illustrate this, Niroshan et al. (2018) reported a liquid limit and plasticity index of 22% and 7% respectively for typical base metal tailings falling in the category of low-plastic clay material. And in another study by Zhao et al. (2021), cupro-auriferous tailings were reported to be slightly plastic with a liquid limit of 19.2% and a plasticity index of 6.1%. Lastly, Yilmaz et al. (2011) studied sulphide-rich polymetallic tailings that yielded a liquid limit of 23% and a plastic limit of close to zero. This type of tailings was classified as a non-plastic silt. The above typify how the Atterberg's limits of tailings will differ depending on their source.

Particle size distribution is one of the most critical parameters in the design of any backfill system. It is generated by means of a particle size analysis. This basically refers to the determination of the percentage by mass of particles within the different size ranges (Craig, 2004). The result of a particle size analysis is presented as a curve on a semi-logarithmic scale similar to Figure 2.3.

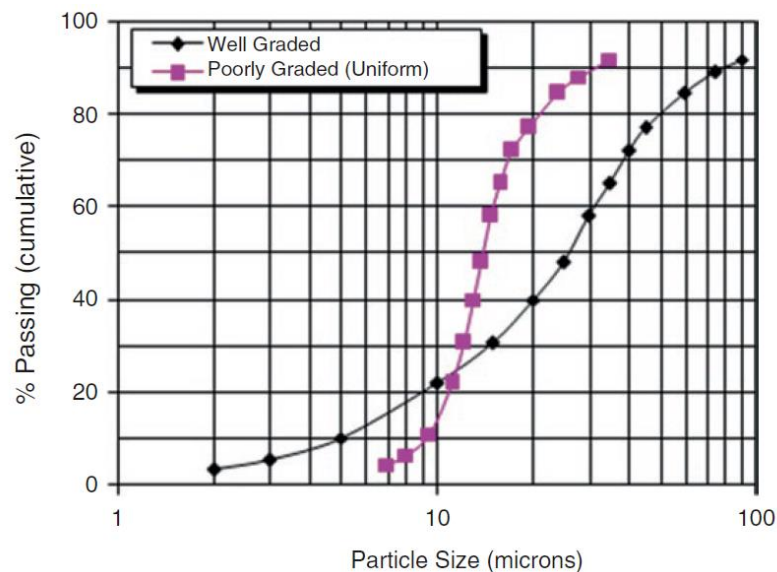


Figure 2.3 Particle size distribution curves for poorly and well-graded backfill material (Ercikdi et al., 2017)

The flatter the distribution curve, the wider the range of particle sizes in the soil; the steeper the curve, the narrower the particle size range. A soil is deemed well-graded if there is no excess of particles in any size range and if no intermediate sizes are lacking. In general, a well-graded soil is represented by a smooth, concave distribution curve. Conversely, a soil is poorly graded if a high proportion of particles have sizes within narrow limits (uniform soil) or particles of both large and small sizes are present but with a relatively low proportion of particles of

intermediate size (Cheng et al., 2020 and Ercikdi et al., 2017). Similarly, well-graded backfill material is constituted of particles of a wide range of sizes. It is poorly graded if its constituent particles are in a narrow range of sizes (refer to Figure 2.3). The general slope and shape of the distribution curve can be described by employing the coefficient of uniformity ( $C_u$ ) and the coefficient of curvature ( $C_c$ ), defined as follows (Craig, 2004):

$$C_u = \frac{D_{60}}{D_{10}} \quad (2.2)$$

$$C_c = \frac{D_{30}^2}{D_{10} \times D_{60}} \quad (2.3)$$

Where  $D_{10}$ ,  $D_{30}$  and  $D_{60}$  denote the respective aperture size of the screen at which 10%, 30%, and 60% of particles pass through. The higher the coefficient of uniformity, the wider the range of particle sizes in the soil. A well-graded soil should have a coefficient of curvature between 1 and 3.

In a series of experimental tests, Ke et al. (2015) demonstrated that finely graded fresh and hardened CTBs consistently result in reduced flowability. Wang et al. (2021) also noted a significant decrease in the flow spread of fresh CTB as the fine content of tailings was increased. Landriault (2006) proposed that a CTB mixture must comprise 15% by weight of particles finer than 20  $\mu\text{m}$  to retain adequate water and form a slurry fill. Otherwise, the mixture would be classified as fine material as pointed out by Kasap et al. (2022) which will lead to a low transportability of the CTB into underground workings.

## 2.4 Hydraulic properties of cemented tailings backfill

According to Ercikdi et al. (2017), the hydraulic properties of CTB collectively refer to the hydraulic conductivity of both saturated and unsaturated backfill as well as the pore water pressure in the cemented backfill.

Hydraulic conductivity may be closely associated with permeability. This is because permeability controls the durability of CTB and the rate of seepage of groundwater through the CTB structure (Fall et al., 2009; Pokharel and Fall, 2013). Permeability also provides useful information about the pore structure, coarseness, and cracking of CTB. Indeed, less desirable pore structures (i.e., coarse pores with high connectivity) and cracks can allow and accelerate fluid transfer between the

CTB and the surrounding rock mass. This in turn may result in increased potential oxidation of the sulphide minerals in the tailings and reduced service life due to sulphate attacks (Fall et al., 2009).

In terms of pore water pressure (PWP) as a hydraulic property, CTB is commonly known to generate excess of PWP once placed underground. A great concern is when the pressure applied by the CTB becomes critically high threatening the stability of the retaining barricade at the base of the stope (Fourie et al., 2007; Jaouhar and Li, 2019). High PWP is generally expected with a faster filling rate of CTB. Nonetheless, the peak value of PWP can be reduced by adding draining holes through the barricade. Another alternative way of alleviating the effect of PWP is by binder hydration through the consumption of water (Tian and Fall, 2021).

## 2.5 Thermal properties of cemented tailings backfill

The thermal properties and processes of CTB materials fall into two main categories: inherent thermal properties such as thermal conductivity and external thermal factors such as curing temperature and the heat released through binder hydration. Both are required to better understand the thermal behaviour of cement-backfilled structures.

Thermal conductivity is defined as *'the heat flux under a unit temperature gradient under a steady state'* (Lee and Shang, 2013). This property is required for the thermal analysis of CTB structures in terms of heat transfer between CTB and the surrounding environment (Ghirian and Fall, 2017). It is also required together with compactness in the selection of adequate backfill material to ensure that its thermal conductivity is not lower than that of the surrounding rock mass.

Fall and Pokharel (2010) reported that the mechanical strength of CTB is sensitive to changes in thermal conditions. Since there are several sources of heat in the underground environment, it is crucial to evaluate the effect of thermal load on the performance of CTB and its response under different thermal conditions (Celestin and Fall, 2009; Li et al., 2022). Indeed, this information would assist in the optimization of the heating or cooling loads of the mines. Contributions by Ghoreishi-Madiseh et al. (2015), Liu et al. (2018) and Zhang et al. (2020) support the fact that backfill can serve as a heat storage material or as a heat transfer medium. As a result, having a good understanding of the thermal characteristics of



backfilling material is critical to the design of cost-effective and high-efficiency energy storage or extraction systems.

## 2.6 Chemical properties of cemented tailings backfill

The chemical properties of CTB are primarily dependent upon the chemistry and mineralogy of its constituents, i.e., tailings, binders, and mixing water (Cui, 2017; Ghirian and Fall, 2017).

In terms of chemistry, chemical properties are interrelated and somehow have an action-reaction effect on each other. For instance, Wu et al. (2015) found that the chemical elements of mixing water may affect the reaction of cement to hydration, thereby influencing the flocculation and strength properties of CTB. This is especially true for water with high content of calcium and magnesium. Indeed, calcium is the primary constituent of hydration products in the form of calcium–silicate–hydrate (or C–S–H). This product is recognised as the main binding phase in the cement hydration process. The said process causes cement hydration products to precipitate into the pores causing pore refinement. The reduced porosity eventually improves the hardening and strength of CTB (Fall et al., 2009; Ghirian and Fall, 2014 & 2017).

In terms of the mineralogical composition of tailings, this is usually determined by X-ray diffraction (XRD) analysis that outputs the type of chart shown in Figure 2.4.

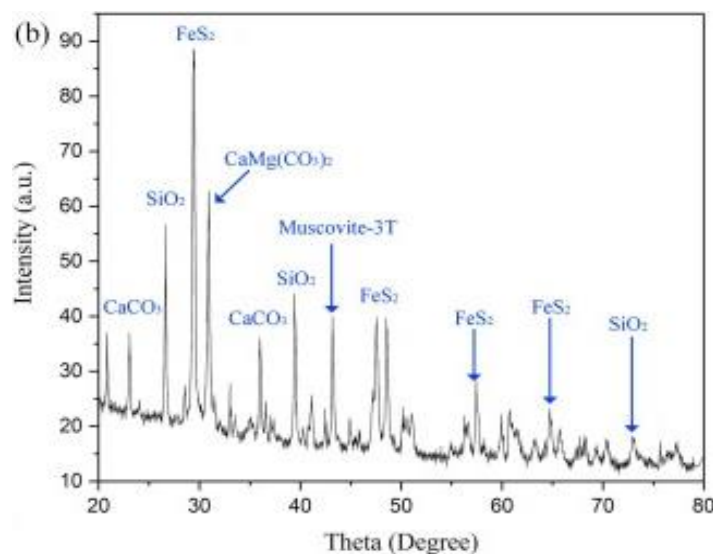


Figure 2.4 A typical XRD chart showing the mineral composition of certain tailings (Qi et al., 2018)

Qi et al. (2018) measured the mineral composition of tailings for use as inputs to a predictive algorithm for the mechanical properties (e.g., UCS) of CTB. The authors found, as can be seen in Figure 2.4, the highest concentration of compounds contained in the tailings is iron disulphide ( $\text{FeS}_2$ ), followed by dolomite ( $\text{CaMg}(\text{CO}_3)_2$ ), and silicon dioxide ( $\text{SiO}_2$ ). This information is useful as one may understand that  $\text{SiO}_2$  affects the filling stability of CTB but improves its permeability (Kasap et al., 2022). Moreover, aluminium trioxide ( $\text{Al}_2\text{O}_3$ ) and calcium oxide ( $\text{CaO}$ ) are important oxides for the coagulation and carrying capacity of CTB (Wang et al., 2017).

## 2.7 Mechanical properties of cemented tailings backfill

The principal mechanical properties of CTB include strength, modulus of elasticity, stress-strain behaviour, and shear strength (Ghirian and Fall, 2019; Liu et al., 2019). It is crucial to understand the mechanical properties of CTB and effectively evaluate its stability of CTB. It is for this reason that several authors (e.g., Liu et al., 2019; Wu et al., 2019; Wang et al., 2020b; Huang et al., 2021) have investigated the mechanical properties of CTB using various testing methods.

The stress-strain behaviour of CTB is generally appreciated graphically. And as illustrated in Figure 2.5, the stress-strain curve can be divided into five stages. According to Wu et al. (2019), the OA stage is characterised by pore compaction whereby stress has a proportional relationship with strain. In this zone, the CTB sample is said to obey Hooke's law (Roylance, 2001).

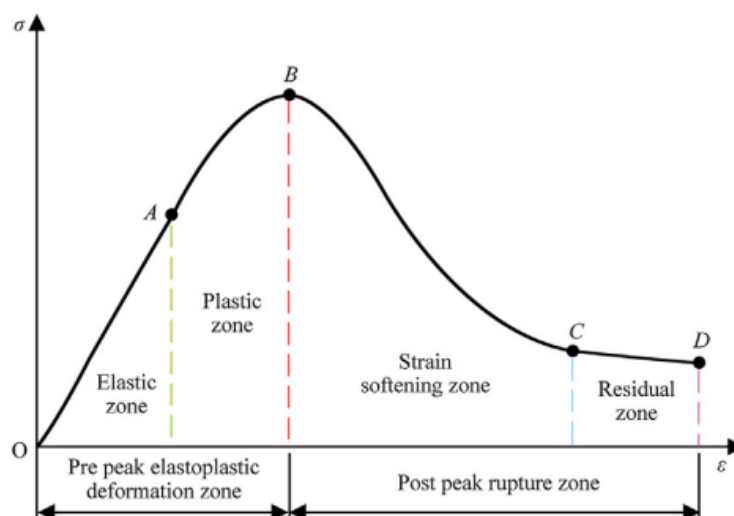


Figure 2.5 Stress-strain curve of CTB samples (Ruijie et al., 2018)

Hooke's law, also known as the law of elasticity, states that the stress of a material is proportional to its strain within the elastic limit of the material in the elastic zone. This means that under compression, stress within the CTB sample will increase with an increase in strain. In addition to this, the CTB material will only return to its original position once the load is removed, hence, the term "elastic" (Roylance, 2001; Sharmain, 2020; Pan et al., 2021). The constant proportionality in this region is also known as the modulus of elasticity or Young's modulus, denoted  $E$  in Equation (2.4) (Roylance, 2001):

$$\sigma = E \varepsilon \quad (2.4)$$

where  $\sigma$  and  $\varepsilon$  represent stress and strain respectively.

In the plastic strain-hardening region AB of Figure 2.5, the stress increases, and the microscopic structure of the CTB sample becomes rearranged (Roylance, 2001). The sample loses its elasticity and exhibits plasticity. When the stress on the sample exceeds its yield stress, a fracture is formed then expands in volume (Ruijie et al., 2018). Note that in the plastic zone, the sample never returns to its original state. Afterwards, zone BCD witnesses localized deformation; strain-softening in stage BC is apparent where the destruction of the CTB sample occurs while stage CD exhibits residual strength of the broken rock particles (Wu et al., 2019).

Deformation or strain is explained by Fall et al. (2007) in an experimental study by characterizing the stress-strain behaviour of cemented paste backfill under compression. From the study, CTB samples were noted to exhibit elastic behaviour at about 30 – 40% of peak stress levels regardless of the type of tailings used. Non-linear behaviour followed as stress increased and later stress level started to decrease slowly as deformations became pronounced. This is because when the cracks generated in the pre-peak and peak regions propagate, the stress-bearing capacity of the samples drops.

Ghirian and Fall (2016) also studied the strength evolution and deformation behaviour of CTB. Their findings showed that all CTB samples exhibited a plastic behaviour after 1 day of curing irrespective of their curing stress and drainage conditions. The observed deformation at failure was 4 – 6% for 1 curing day and 1 – 2 % for 7 curing days. However, the samples exhibited less ductile behaviour as curing time increased, i.e., the sample could return to its original shape after

compression. Several other experiments confirmed these findings by arguing that CTB tend to show low ductility due to ongoing binder hydration as curing time increases (Yi et al., 2015; Jiang and Fall, 2017). In another study, Chen et al. (2018) studied the compressive behaviour of CTB reinforced with polypropylene fibre. The main purpose of adding polypropylene (PP) was to improve the stability of CTB and reduce cement usage. As can be seen below, Figure 2.6 shows two sets of stress-strain curves for the two CTB samples coded as per their mixture design, i.e., T2 (25% cement; 0.1% of fibre) and T6 (20% cement; 0.05%), each sample with and without fibres. The following average deformability secant modulus (or E50) at 50% of the peak stress were found: 107.78 MPa, 54.92 MPa, 182.94 MPa and 84.18 MPa for T2 (No fibre), T6 (No fibre), T2 (PP fibre) and T6 (PP fibre) respectively. It is evident from Figure 2.6 that the PP fibre enhanced CTB ductility; Yi et al. (2015) also reported similar findings.

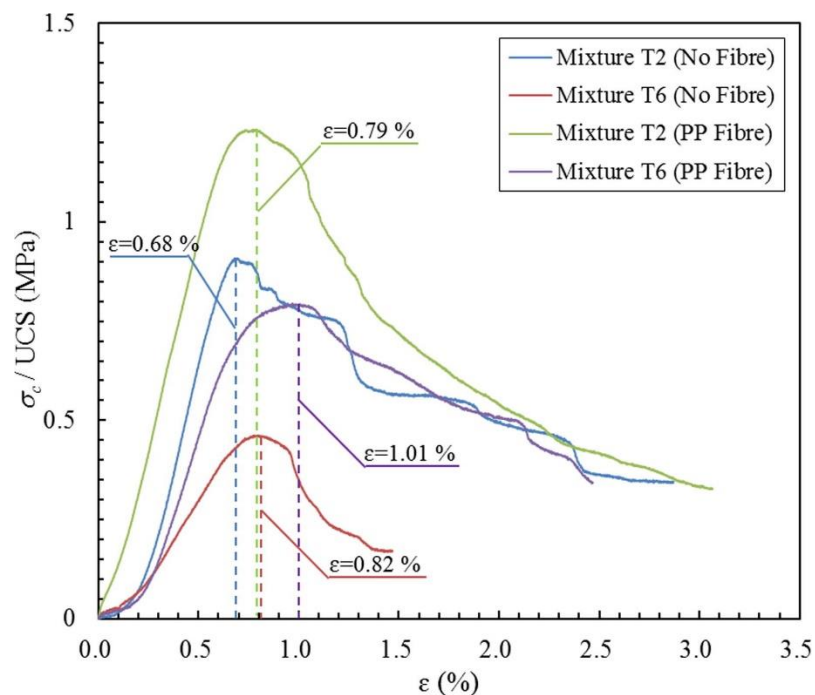


Figure 2.6 Stress-strain curves of CTBs at 28 curing days for mixtures T2 (no fibre), T6 (No fibre), T2 (PP fibre) and T6 (PP fibre) (after Chen et al., 2018)

Zhang et al. (2022) proposed a simplified interpretation of the stress/strain curve in terms of the failure modes experienced by CTB samples. Five failure points are identified; they correspond to the loading start point, the yield point, the peak point, the post-peak point, and the loading end point. As evidenced in Figure 2.7, no cracks are yet apparent in the sample in the elastic zone (pore compaction stage). The first crack becomes visible when the sample enters the yield stage. The

existing cracks gradually propagate while new ones are generated as the loading continues. As additional cracks form and penetrate the matrix, the strength of the sample diminishes. The CTB sample finally experiences mainly tensile failure accompanied by some secondary tensile cracks extending from both ends of the backfill sample to the middle.

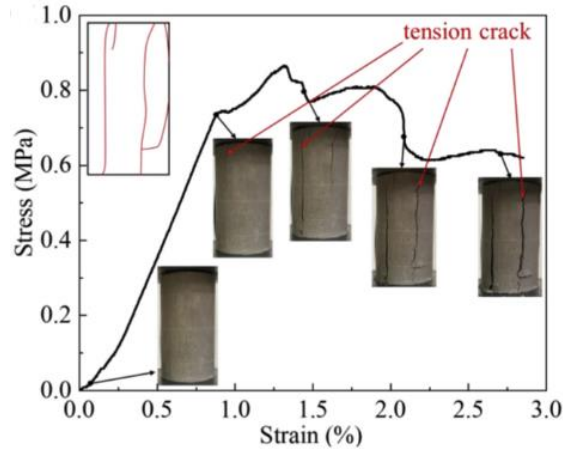


Figure 2.7 Failure modes of CTB under various stages of the elastoplastic and post-rupture zones (after Zhang et al., 2022)

In another study, Pan et al. (2021) explored the behaviour of CTB samples in terms of their shear strengths. They found that shear stress is proportional to shear strain until peak stress is reached. This is believed to be due to the breaking of the cement bonds. However, after the peak, the shear stress started to progress in an inversely proportional relation to shear strain. The mobilization of full frictional resistance may explain this switch. And in the last stage, the shear stress remained constant or decreased slightly as shear strain increased.

Two shear strength properties are used to characterize the failure and shear behaviour of CTB structure: cohesion and internal friction angle. They play a critical role in the stability of side-exposed cemented backfill and control the interface between CTB and the surrounding rock mass. It is also important to note that interfacial failure mainly happens on the soft side of the CTB structure since the rock mass is stiffer and stronger than CTB (Libos and Cui, 2021).

The general assumption is that failure occurs when shear stress matches shear strength in a CTB structure. The commonly used method to describe this is Mohr-Coulomb's theory expressed as follows (Wu et al., 2019):

$$\tau_f = c' + \sigma'_f \tan \phi' \quad (2.5)$$

The strength parameters in Equation (2.5) are cohesion ( $c'$ ) and internal friction angle ( $\phi'$ ) while  $\tau_f$  is the shear strength and  $\sigma'_f$  is the effective normal stress.

Komurlu et al. (2018) also investigated the shear strength of CTB by means of laboratory experiments. From their work, they were able to show that the compressive strength of CTB material can be inferred from its cohesion and internal friction angle as follows:

$$UCS = 2 c' \sqrt{\frac{1+\sin \phi'}{1-\sin \phi'}} \quad (2.6)$$

In closing, the strength of CTB is mainly determined by uniaxial compressive tests because of their reliability and simplicity. The strength here refers to the maximum compressive stress the CTB samples can withstand before failure (Mozaffaridana, 2011). Shear strength tests are resorted to when necessary due to the logistical challenges associated with the implementation of the tests. Equation (2.6) may alternatively be relied upon to infer the shear strength properties from UCS results. The next section discusses some of the internal factors that affect UCS in view of how central it is in testing for the properties of CTB.

## 2.8 Effects of internal factors on the strength of cemented backfill

Internal factors are primarily associated with tailings, binder, and water as the main ingredients of backfill. Other internal factors include the physical and chemical properties of backfill (Benzaazoua et al., 2004; Ercikdi et al., 2017). That is why in this section, the effects of the following internal factors are reviewed: particle size distribution, chemical composition, binder content, admixtures, and binder hydration.

### 2.8.1 Effects of particle size distribution

Particle size distribution is one of the most critical parameters in the design of any backfill system. It affects not only the backfill support capabilities, but also how the backfill is transported and placed hydraulically (Stacey, 2001).

Concordant research recommends that the CTB mixture must comprise 15% by weight of particles finer than 20  $\mu\text{m}$  to retain adequate water and form a slurry fill (e.g., Kesimal et al., 2004; Landriaut, 2006). High fine content also reduces the

permeability of CTB as pointed out by Cheng et al. (2020). This is because fine particles fill the pores between coarse particles and reduce the porosity of the material consequently improving the strength of CTB.

Ke et al. (2015) experimentally studied the effect of particle gradation on fresh and hardened CTB. In doing so, they were able to show that UCS values consistently increase with the content in fine particles in the tailings irrespective of curing time. This was attributed to the fact that fine particles in the tailings filled the voids between larger particles thereby increasing the packing density. The latter is known to improve strength development (Fall et al., 2005; Kwan et al., 2014). In contrast to the above, Wang et al. (2021) prepared tailings of different fine contents ( $< 20 \mu\text{m}$ ) to study the effect of fine tailings on the properties of CTB. They then reported a 30% increase in UCS when fines were increased from 22.08% to 42.2%. They further noticed a 9.1% decline in UCS when the fraction of fines changed from 42.2% to 62.94%. The cause of the decline is unknown; however, it is possible that the packing density may have contributed to this trend.

As a last noteworthy account, Wu et al. (2018) explored the effect of particle size distribution. This team of researchers reported that particle size distribution not only strengthens the structure of CTB but also increases its corrosion resistance. However, the researchers stress that looking at the effect of particle size distribution alone is not enough because their backfill was cured under confining pressure. In this case, backfill samples cured under pressure generally go through the rearrangement of particles caused by the settlement of fine particles. The fine particles settle under the influence of consolidation, which significantly affects the structural and mechanical properties of backfill.

### *2.8.2 Effects of mineral composition*

The mineral composition of tailings is reported to have an impact on the characteristics of CTB (Ercikdi et al., 2017). Although mineral content differs from tailings to tailings, Lemos et al. (2021) stated that gold tailings commonly consist of quartz, silicates (e.g., gypsum), oxides (e.g., iron-based), carbonates (e.g., calcite), sulphides (e.g., pyrite), sulphates (e.g., gypsum) and gold minerals. Akkaya et al. (2021), on the other hand, found CaO, Fe<sub>2</sub>O<sub>3</sub>, Zn, Pb and K in the gold tailings samples they used. Other studies have also indicated that tailings from

gold, zinc and lead mines usually contain sulfidic minerals, mainly pyrite ( $\text{FeS}_2$ ), arsenopyrite ( $\text{FeAsS}$ ) and pyrrhotite ( $\text{Fe}_{1-x}\text{S}$ ). The oxidation of the aforementioned compounds leads to chemical reactions with hydration products and binder phases. This may decrease the strength of the CTB material and cause its undesirable expansion (Cihangir et al., 2012; Liu et al., 2020; Yin et al., 2020). Adding to this, Tariq and Yanful (2013) were able to argue that the high content of  $\text{C}_3\text{A}$  in Portland cement increases the formation of expansive ettringite in the CTB matrix which contributes to the damage of hardened CTB.

It is therefore clear from the above that mineral composition needs to be factored into the design of CTB. Looking at work by Feng et al. (2015) and Jiang et al. (2020a), the authors suggested that the formation of expansive sulphate phases such as gypsum can cause expansion and cracks of CTB. In this light, Li and Fall (2016) found that sulphate affects the strength development of CTB at an early age. Indeed, by testing four samples of CTB with different content of sulphate (0, 5 000, 15 000, and 25 000 ppm), they demonstrated that sulphate-containing CTB yields a slow strength development compared to sulphate-free CTB for all curing times as shown in Figure 2.8. They attributed this to the combined effects of inhibition of cement hydration, formation of expansive products (e.g., ettringite) and sulphate absorption by calcium silicate hydrate (C–S–H).

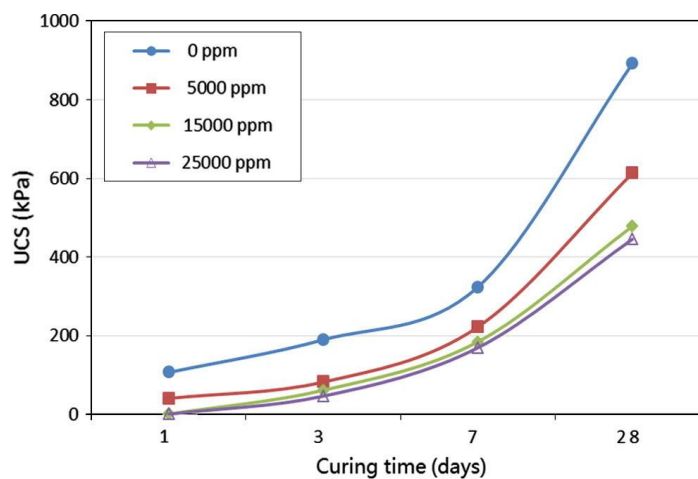


Figure 2.8 Effect of initial sulphate content on the strength of CTB at an early age (Li and Fall, 2016)

Similarly, Wang et al. (2020a) investigated the effect of sulphate attack on the mechanical strength of backfill. In this case, they found that the chemical reaction between sulphate and hydration products at the initial stage had a positive effect on the UCS of backfill due to the refinement of the pores. However, a continuous



reaction results in excess gypsum in the pore space that damages the microstructure and degrades the fill material. The effect of sulphate attack on the strength of CTB is summarised in Figure 2.9. It can be seen that the sulphate treated CTB (red graph) shows a great increase in UCS at the early stage which eventually decreases after 160 curing days. In contrast, the sulphate clean CTB (black graph) shows a gradual increase of UCS with the curing time.

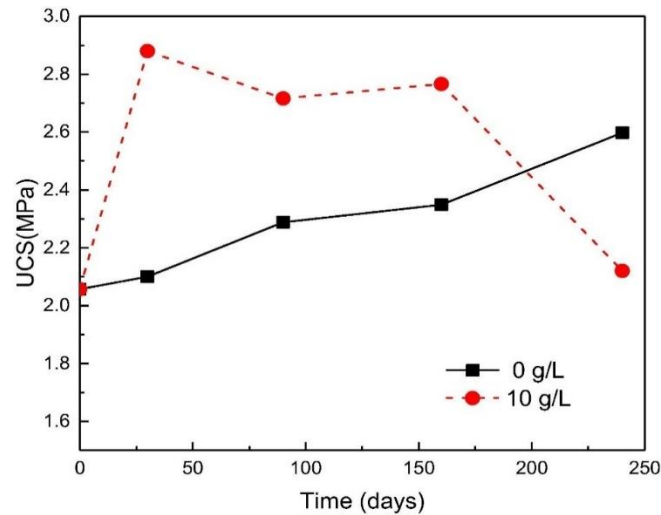


Figure 2.9 Comparison of UCS values for sulphate-treated and sulphate-free CTBs (Wang et al., 2020a)

Dong et al. (2019) also reported similar observations and found that sulphur content before 90 curing days has a strengthening effect on the CTB samples. However, the strength of CTB decreased gradually after 20 days of curing due to severe erosion of sulphur. As a result of this, the authors deduced that in the long run, the lower the sulphur content the better as far as the long-term strength of CTB is concerned. The initial gain in strength of sulphate-treated CTB is clarified by Zheng et al. (2018 & 2019) who explained that the gypsum fills the openings of the matrix. This produces an expansion force that strengthens the fill material. However, when the gypsum is produced in excess, the expansion force exceeds the strength of the backfill causing cracks in the sample and UCS decrease.

The experimental study by Akkaya et al. (2021) also attests that sulphate decreases the mechanical strength of CTB. This is mainly due to the chemical reaction between sulphate and the sulphuric acid produced from hydration. However, the difference with this study as illustrated in Figure 2.10 resides in the relationship between the UCS and the sulphate content of CTB. According to the reported findings, increasing cement content from 3% to 7% reduced total sulphur

concentration due to residual stiffness. It is clear that in high cement contents, the dispersion of sulphate inside the CTB sample and its conversion to ettringite will be slowed down with curing time. However, it should be noted that Akkaya et al. (2021) used Portland Pozzolan (CEM II/A-P) and Pozzolan (CEM IV/A) cement often preferred in works where sulphate and chloride ions are relatively high.

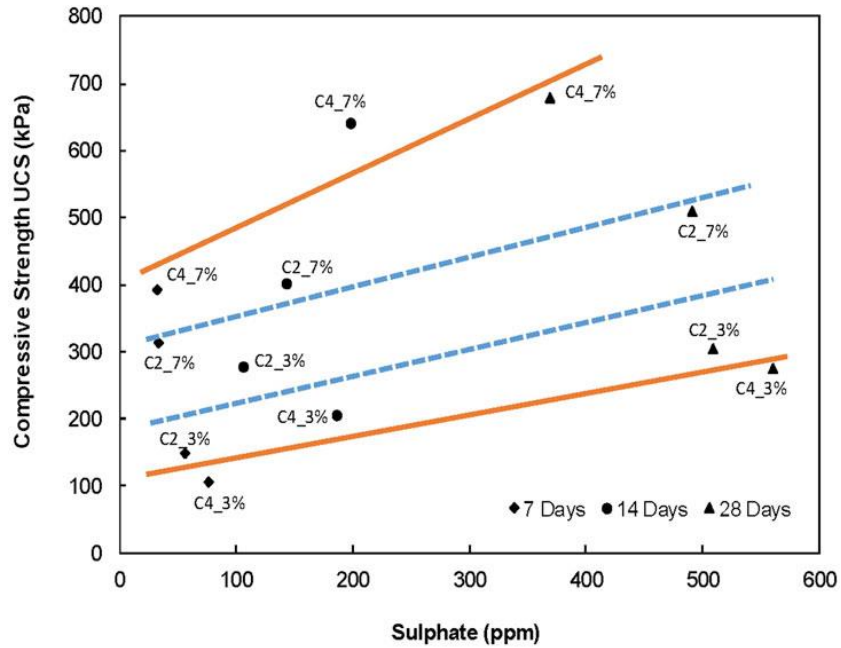


Figure 2.10 Relationship between UCS and sulphate content for CEM II/A-P pozzolan (C2) and CEM IV/A (C4) cements (Akkaya et al., 2021)

In closing, Akkaya et al. (2021) asserted that increasing cement content above 7 wt.% and fast setting time can prevent the formation of secondary gypsum and ettringite. This positive contribution has the potential to assist in preventing sulphate attacks when using high sulphide tailings. However, the financial implications of using these types of cement is yet to be established. This is highly important considering that binder consumption contributes over 60% to operational costs (Ghirian and Fall, 2014; Wang et al., 2021; Zhang et al., 2021).

### 2.8.3 Effects of binder-to-tailing ratio

Binders are added to mine tailings to enhance the strength of CTB. A commonly used binder is cement. Alternative binders that have also been tested to provide effective strength enhancement include fly ash and blast furnace slag. Binders used when preparing CTB mixtures are referred to as hydraulic reagents. Hydraulic reagents are anhydrous phases that react with water to create hydrated phases.

The latter provides backfill cohesiveness and long-term strength (Benzaazoua et al., 2004; Wang et al., 2018).

Some authors have reported that the higher the binder content, the higher the strength development of CTB (e.g., Sasa et al., 2019; Wang et al., 2018). Similarly, Fall et al. (2008) investigated the mixed proportions of CTB and found that increasing the cement content leads to increased UCS of CTB. They explained that the strength gain was due to the fact that increasing cement content led to the formation of more hydration products which subsequently strengthens the cement matrix. These findings are consistent with Yilmaz and Ercikdi (2016) who estimated the UCS of CTB from the ultrasonic pulse velocity test. The two authors found that UCS increased with increasing binder dosage regardless of curing time. The continual increase of UCS even after 28 days was attributed to the on-going hydration process. In other words, the formation of hydration products proceeded even after 28 curing days. Studies supporting this assertion are available; they also show that the increase in binder content accelerates binder hydration and reduces voids in the matrix: see for example Wang et al. (2018) and Yilmaz (2018).

Finally, in an interesting study, Xu et al. (2018) assessed the effect of the cement-to-tailing ratio on the strength of CTB by electrical resistivity measurement. The study reported the highest strength increment rate of CTB (i.e., 20%) at an early age (i.e., 3 to 7 days). In contrast, the lowest strength increment rate (i.e., 5%) was recorded at 7 – 28 days of curing. The decline was attributed to the dilution of the concentration of soluble ions such as  $K^+$ ,  $Ca^{2+}$ ,  $Na^+$  and  $OH^-$ , which led to the reduction of the generation of hydration products.

#### *2.8.4 Effects of moisture content, porosity and saturation*

The mechanical performance of CTB is known to be influenced by its physical properties, i.e., void ratio (or porosity), degree of saturation, and water content (Ghirian and Fall, 2017; Shunman et al., 2021).

Moisture content is a measure of the quantity of water present in the soil. It is defined as the ratio of the mass of water to the mass of dry soil whereas water saturation is the amount of water that has filled the voids in the soil (Naguleswaran, 2018).

Zou and Sahito (2004) used 20.5% of water to mix binder and tailings and found that the mixture (binder + tailings) was still too dry to mix well. They increased the water content to 24.6% and observed a decrease in CTB strength. Researchers such as Mozaffaridana (2011) and Yilmaz (2018) also reported similar findings: UCS decreases with an increase in water content. They argued that, on the one hand, high water-to-cement ratio increases the porosity of the CTB and, on the other, a low ratio leads to a significant increase in CTB strength due to reduced porosity of the matrix.

This now brings us to talk about the effect of porosity. Liu et al. (2018) studied the relationship between pore characteristics and UCS of cemented paste backfill. They found that UCS decreases exponentially as porosity increases as captured in Figure 2.11.

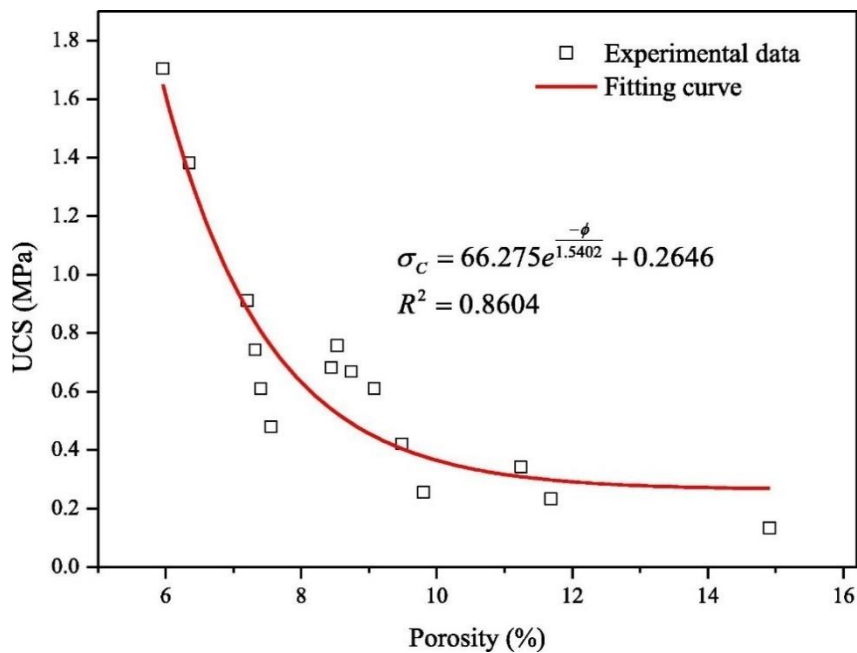


Figure 2.11 Relationship between porosity and UCS for CTB (Liu et al., 2018)

In terms of the effect of water saturation, as defined above, Wang et al. (2017) measured the mechanical properties of fly ash concrete. They found that the UCS of concrete decreased with an increase in water saturation (Figure 2.12). When the concrete samples were fully saturated, the UCS declined to a minimum. The limitation of these findings is that they should be applied to CTB with caution since CTB is a different material from concrete.

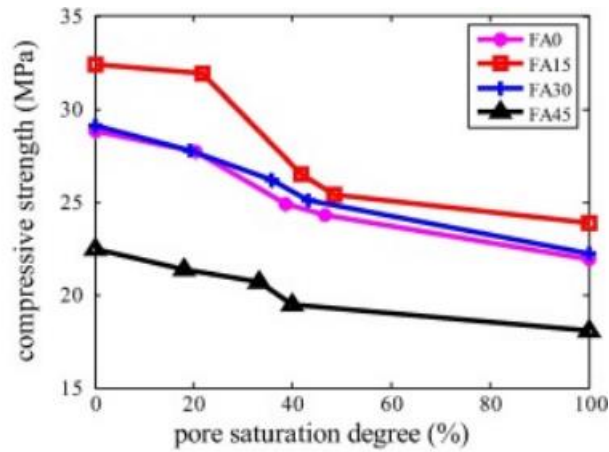


Figure 2.12 Relationship between UCS and water saturation for fly ash concrete (Wang et al., 2017)

To address the limitation in their previous study (Wang et al., 2017), Wang et al. (2021) explored the effect of water saturation on the mechanical characteristics of CTB. Figure 2.13 shows that the UCS first increases and then decreases with water saturation. When saturation was increased from 22.1% to 47.0%, the UCS was found to increase from 2.71 MPa to 3.91 MPa. However, between 65.3% to 100% water saturation, the UCS of CTB dropped sharply. The authors ascribed the initial increase of UCS to the high saturation that accelerated the formation of hydration products. From 65.3% saturation and beyond, the formation of hydration products was already complete. The excess water molecules expanded the internal structure of the CTB. The pore structure began to increase thereby compromising cohesion and UCS.

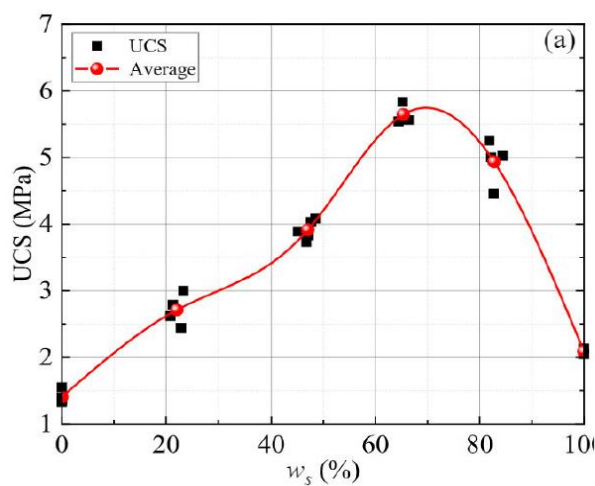


Figure 2.13 Relationship between UCS and water saturation for CTB material (Wang et al., 2021)

Of note here is that the work conducted by Wang et al. (2021) has led to results not in agreement with what was presented by Wang et al. (2017). From Figure 2.13, it is posited that the initial positive correlation between saturation and UCS is due to the accelerated rate of hydration. Meanwhile, other studies argue that pore water is consumed during cement hydration (Nasir and Fall, 2010; Libos and Cui, 2020). The cause of the discrepancy in these findings is contended, the reason being that Libos and Cui (2020) used quartz tailings while Wang et al. (2021) did not disclose the source of their tailings. Although, both tailings have a high content of SiO<sub>2</sub> as per their mineral composition findings. There is, however, a possibility that the findings by Wang et al. (2021) may be misrepresented because the authors did not consider curing time when reporting these findings. If the findings were observed at an early age (1 day) then they would not raise an alarm.

#### *2.8.5 Effects of chemical admixtures*

Admixtures are defined as “*ingredients other than cement or water that may be added to CTB to impart a specific quality*” (Mozaffaridana, 2011). One of the admixtures usually added in tailings is fibres. The use of fibres was introduced by Zou and Sahito (2004) to reinforce tailings and used shotcrete for underground support. Indeed, the flexural strength of the shotcrete was found to increase by 59% when polymer fibres were added. However, CTB has different properties from concrete which raises the question as to whether similar results can be obtained.

Festugato et al. (2013) attempted to answer this by studying the shear response of fibre-reinforced CTB under cyclic shear tests. They then found that the addition of fibre enhances the load-carrying capacity of CTB. The drawback of this study was that it mainly focused on shear strength and did not look at the compressive strength of the backfill. In an attempt to bridge this gap, Yi et al. (2015) conducted an experimental study on the compressive behaviour of polypropylene fibre-reinforced CTB. The UCS of fibre-reinforced CTB samples with 5% cement was found to have increased faster (70 – 90%) than unreinforced samples with 5% cement. The findings showed that the fibre samples were more ductile while the unreinforced ones exhibited brittle behaviour. However, this study only investigated one type of fibre, i.e., polypropylene. It did not also compare various types of fibre reinforcement. As such, it is yet to be established which type of fibres may be adequate for use in cemented backfills.

In another study, Chen et al. (2018) paid attention to the dosage of polypropylene fibre added to CTB samples. The addition of fibre was found to have a positive effect on UCS to a point beyond which UCS dropped after 28 days. Fibre can reinforce the interaction of the tailing's particle-particle structure and improve the strength of CTB. As more fibre is added, this creates weak structural spots within the CTB matrix with unintended consequences on the integrity of the CTB. Chen et al. (2018) therefore concluded that the best fibre content for highest UCS is 0.15%. Similar findings on CTB were obtained by Xu et al. (2019b) who reported an increase in UCS with a steady but marginal addition of fibres. Here, the argument was that fibres intertwined during the preparation of CTB samples with marginally high fibre content. This then led to increased mechanical strength as the network of fibres delayed the propagation of cracks. This understanding was later confirmed by Chen et al. (2020) who noted experimentally that the presence of fibres prevented the formation of tensile and shear cracks. Similar studies may be required on sulphide-rich tailings widely used in underground backfilling.

To this end, one paper was identified in which poly-naphthalene sulfonate and polycarboxylate condensate were used as water-admixtures in the preparation of sulphide-rich cemented tailings backfill. Ercidki et al. (2010) found that the effect of sulphate attack on the strength of CTB was negligible. The improved strength was ascribed to the ability of fibres to delay the propagation of cracks in the CTB samples. Further work is required to consolidate these empirical findings.

Other authors have studied the effect of different fibres such as superplasticizers on the strength of CTB. Simon et al. (2011) for example found that the UCS of CTB continuously increased with an increase in fibre content; thus, diverging from the previous findings. On the other hand, Zhang et al. (2018) studied the effect of poly naphthalene sulfonate, a different kind of fibres known as superplasticizer, on the UCS of CTB. Unlike the previous findings, this study found that the addition of a superplasticizer had a negligible effect on strength of CTB at an early age (1 day). Then, an increase in CTB strength was recorded between 7 and 28 days. Figure 2.14 presents the evolution of CTB strength for different content of poly-naphthalene sulfonate and curing times. The capability of the superplasticizer to improve CTB strength was attributed to its propensity to reduce moisture content while maintaining the fluidity of the backfill mixture.

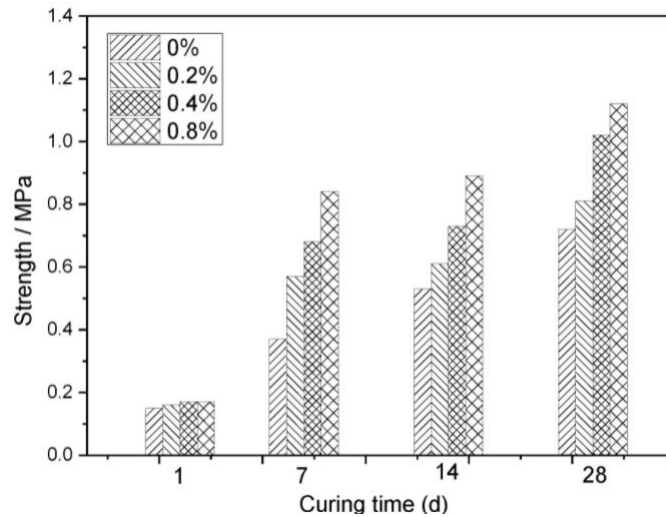


Figure 2.14 Strength evolution of CTB specimens with different poly naphthalene sulfonate dosages (Zhang et al., 2018)

The findings from Xue et al. (2021) that diverge from those of Zhang et al. (2018) are worth noting. Indeed, Xue et al. (2021) studied the mechanical properties of CTB when reinforced with different superplasticizers. The highest strength was noted at a 0.6% fibre content. However, when the fibre content was increased to 0.9%, the corresponding strength decreased from 3.432 MPa to 3.058 MPa, from 3.314 MPa to 2.933 MPa, and from 3.025 MPa to 2.465 MPa for polypropylene-, polyacrylonitrile-, and glass-fibre reinforced backfills cured after 28 days respectively. The tailings-fibre interaction may be at play, but just like Chen et al. (2018) and Xu et al. (2018), Xue et al. (2021) suggest that once the fibre content is in excess in the CTB mixture, a weak structure is formed thereby leading to failure of the CTB material.

### 2.8.6 Effects of binder hydration

The hydration heat in CTB is mainly caused by cementitious materials added to CTB during preparation. The addition of water to ordinary Portland cement starts the cement hydration reaction immediately. The cement hydration process causes cement hydration products to precipitate into the pores, which can lead to pore refinement and reduction of porosity (Fall et al., 2009). Reduced porosity further improves the hardening and strength of CTB (Ghirian and Fall, 2014). It is for this reason that several studies have attempted to scrutinise the effect of binder hydration on the strength of CTB.



Nasir and Fall (2010) studied the coupled effect of hydration and temperature on the strength development of CTB. The study found that the effect on CTB is significant at early ages (7 days) when the rate of binder hydration is high. This leads to high water consumption, thus, hardening of the CTB material.

Fall et al. (2010) also studied the mechanical properties of CTB. The UCS of CTB was found to increase as binder hydration progresses. This is because binder hydration generates heat, consequently, hydration products such as calcium, silicate and hydrate are formed (Fang et al., 2021).

In summary, the hydration products are major binding agents responsible for CTB hardening (Nasir and Fall, 2010; Fang et al., 2021). This is further corroborated by Liu et al. (2021) who studied the effect of binder hydration on CTB and found that CTB gains the required strength to form structural support through binder hydration.

## 2.9 Effect of external factors on the strength of cemented backfill

External factors refer to external surrounding and how it affects the performance of backfill. These factors include temperature, confining pressure/stress, humidity, and stope geometry within the rock mass and in-situ (Zhang et al., 2020). Other external factors of interest are the stope dimension, the backfill-rock interaction, the placement conditions, consolidation, and drainage conditions (Yin et al., 2020). They are succinctly presented in the sub-sections below.

### 2.9.1 *Effects of curing conditions*

Cemented tailings backfill (CTB) poured in underground stopes is subjected to different curing conditions. The CTB material experiences effective stress due to self-weight consolidation and overburden pressure. The in-situ environmental conditions include high humidity and high temperatures (Walske et al., 2015). This state of affairs has led to several studies attempting to understand the effects of all these conditions on the strength of CTB. For example, Hu et al. (2019) studied the strength characteristics of CTB under different humidity curing conditions. It was found that the greater the humidity, the lower the strength. This was attributed to the greater humidity means high moisture content between the CTB particles which results in a decrease in the UCS of CTB. Wu et al. (2020) also investigated the

effect of humidity on the performance of CTB and found that higher humidity improves the peak value of total stress in the CTB. This is because increased humidity increases the water content and temperature of CTB. Consequently, the binder hydration is enhanced by generating more hydration products which improves the strength development of CTB.

There seems to be a lack of research work done to support the findings by Wu et al. (2020). However, Yilmaz et al. (2009) attempted to reproduce underground curing conditions of temperature, pressure/stress and humidity. To do that, they use a modified laboratory apparatus called curing under applied pressure (CUAPS) and studied the strength development of CTB. Although much insight was gained from the exercise, the effect of humidity on the CTB samples was not reported. Further research is therefore required to close this gap.

Every underground mine is unique with regard to its prevailing temperature. This may vary with depth, geological conditions, geographical location, and the heat generated from the rock and machinery (Fall et al., 2010). As ore reserves are depleted at shallow depths, underground mining operations are moving to greater depths. This is naturally associated with heat influx increases because of the geothermal gradients. The average geothermal temperature of a mine ranges approximately from 30°C to 40°C at 1 km depth (Jones, 2018). From measurements done in a South African gold mine, Rawlings and Phillips (2001) reported temperatures of the order of 35°C, 50°C and 70°C at 3 km, 4 km and 5 km respectively. Even Xu et al. (2021) confirmed that the underground stope temperature can reach up to 50°C at a mining depth of 4 km. And in an experimental enquiry, Xu et al. (2019a, 2020, 2021) discovered that the mechanical strength of CTB can be enhanced by increasing the curing temperature. They noted that the UCS of CTB samples increased proportionally with the curing temperature. Like with Selah and Eskander (2020), higher UCS values were reported from samples cured at 50°C regardless of the curing age. The higher curing temperature was argued to enhance binder hydration. Fall et al. (2010) and Walske et al. (2015) also found that the strength development of CTB increased with increasing temperature as shown in Figure 2.15. However, Fall and Samb (2009) cautioned that temperatures should not exceed 400°C; otherwise, hydration products would decompose and lead to the formation of cracks by dehydration.

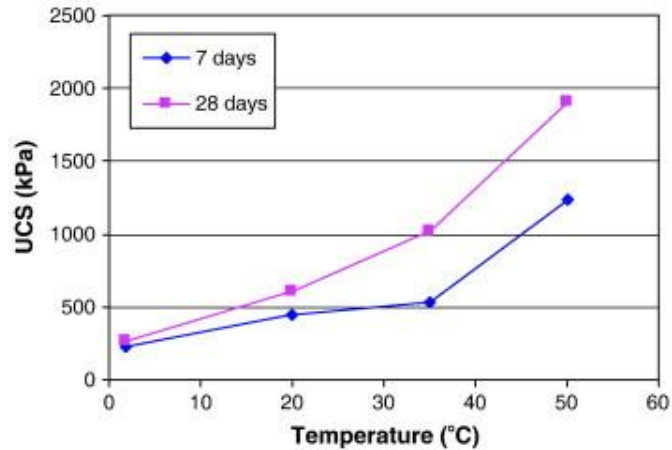


Figure 2.15 Relationship between temperature and UCS of CTB (Fall et al., 2010)

In the context of a mining operation, once CTB is placed underground, it is immediately exposed to ground stress. Vertical stress is known to improve water drainage as it consolidates CTB which also results in high strength development of CTB at an early age (Yilmaz et al., 2009). Similar findings were reported by Ghirian and Fall (2016) who explained that samples cured under stress have higher UCS than those cured under stress-free conditions. This is because higher stress increases the packing density of the particles of tailings, thus, reducing the porosity of CTB. Following from this, Shunman et al. (2021) investigated the coupled effect of curing stress and temperature on CTB. They found that its UCS increased with an increase in curing stress under the same curing temperature. The influence of curing stress on the UCS of CTB was more significant at early ages than later on. This happens when the CTB material had been completely drained through consolidation (Belem et al., 2016).

### 2.9.2 Effects of stope layout/dimensions

In one study, Belem et al. (2016) highlighted the importance of the conditions of an underground open stope. In particular, stope geometry should be taken into account in order to obtain a representative mechanical and physical behaviour of CTB. For this reason, Yilmaz et al. (2015) studied the effect of specimen size on the strength of CTB placed under different placement conditions. The idea was to simulate stope layout by testing various samples with different sizes (diameter x height), i.e., D x H: 10 x 20 cm, 7.5 x 15 cm, and 5 x 10 cm. They found that the samples with the smallest diameter yielded high UCS regardless of the placement conditions. A low density of micro-cracks and pores was created because of the

small size of samples. In a complementary study, Cui and Fall (2018) simulated the effect of stope size on the strength of CTB using a multi-physics model. A range of stope sizes (i.e., width x height) were considered: 5 x 10 m, 8 x 16 m, and 10 x 20 m. The simulation outputs revealed that higher strength (UCS) was experienced with larger stopes due to more heat generated in the CTB mass. This is also in agreement with the findings of Nasir and Fall (2009).

Yilmaz (2018) investigated the effect of stope depth on-field behaviour of CTB by curing the CTB samples under different magnitude of stress to simulate different stope depths. For example, he applied a vertical pressure of 113 kPa to mimic a stope depth of 5 m. Pressures of 227 kPa and 340 kPa translated to stope depths of 10 m and 15 m respectively. Using this approach, Yilmaz (2018) reported high strength gain in 50 m stope due to high vertical stress. He also found that the strength gain of the CTB samples was higher at the bottom of the stope than at the top because of the consolidation effect. Cui and Fall (2018) also reported consistent findings; however, they postulated that the higher strength gain at the stope bottom is because freshly poured CTB is found higher on the stope whether backfilling is continuous or done in sequences.

The size of stopes may vary in height or width from large to narrow and wide depending on the rock mass stability. For a large stope, it is impossible to complete the filling process all at once (Xu et al., 2019a). This would result in high hydrostatic pressure on the barricade, increasing the risk of failure. According to Cao et al. (2018), mines adopt a strategy whereby backfilling is performed in two stages: a plug pour and a final pour to alleviate the pressures on the barricade. And for a large-scale stope, backfilling should be done gradually and at regular intervals. As a result, the CTB pillar appears in a layered structure owing to multiple fillings (Fu et al., 2020; Wang et al., 2019; Xu et al., 2019b). Fu et al. (2020) also add that multiple filling of backfill changes the mechanical properties of CTB and influences its failure mode. In addition to this, Wang et al. (2019) support that the mechanical properties of a single-layered backfill and stratified backfill differ. Wang et al. (2019) also explained in the same paper that the peak strength of CTB decreases with increasing backfilling time. And unlike single-layered backfill, the failure modes of stratified backfill mainly occur in the upper layer near the loading area. The researchers hence deduced that the weakening of the CTB structure is closely related to the layering structure of the fill.

Perhaps the most important point to make pertains to the outstanding study by Xu et al. (2019b). In this work, the scholars provide invaluable insights on the response of stratified CTB in large stopes. They highlight the fact that a high backfilling ratio (the rate at which backfilling is done) more often than not negatively affects the strength of stratified CTB. And lastly, stratified CTB samples tend to display greater brittleness.

### *2.9.3 Closing remarks*

A review of the factors affecting the strength (UCS) of CTB was conducted. Although several factors such as curing conditions, temperature, binder hydration, and particle size distribution have been extensively studied, there is still room for further explorative work. For example, there is no documented study that extensively explore the effects of the aforementioned factors on the behaviour of CTB structure. Layered CTB is backfilled in intervals (24 hours gap), therefore, there is definitely temperature differences between the layers. Additionally, if the CTB is placed in environment with high horizontal stress, the dislocation of the layers may occur. Moreover, the seepage of water through layers interfaces may gradually disintegrate the backfill material. Thus, opening several gaps of research for further investigation.

Indeed, scrutinising the effect of internal and external factors on the behaviour of CTB has led to the betterment of the design of CTB in the mining industry. With the continuous improvement in mining technology and methods, on-going research on CTB for underground support is required. In addition to laboratory experimental study, numerical modelling and simulation can be another effective method to describe and analyse the behaviour of CTB. The next section presents some of the analytical and numerical methods used to study the behaviour of CTB.

### **2.10 Stability analysis of backfilling body**

Alternate primary and secondary stopes are generally delineated in high-production mining technologies such as blast hole stopping. First, the major stopes are removed and backfilled. Then, the backfill is allowed to cure for some time. After that, the secondary stopes are extracted. During secondary stope extraction, the cemented fill acts as an artificial rib pillar that must remain self-standing, and

the side wall of the fill will be exposed as shown in Figure 2.16. Any failure of the backfilled material from the primary stope may result in ore dilution and may lead to ground instability. As a result, the stability of backfill walls is critical (Godugu et al., 2021; Yang and Aubertin, 2017). The stability of paste fill stopes increases with an increase in binder percentage and declines with an increase in stope size, according to the literature review (Godugu et al., 2021).

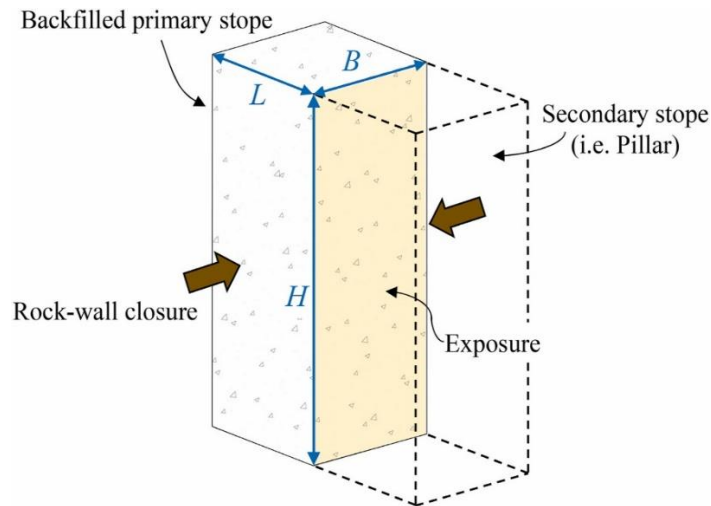


Figure 2.16 Side exposed backfill body during secondary stope extraction (Wang et al., 2021)

### 2.10.1 Vertical exposed stopes

The exposed backfill is often designed and built to withstand the pressure generated due to its self-weight. The CTB pillar is then treated as a freestanding vertical 1-dimensional (1D) prism, with the required unconfined compressive strength (UCS) exceeding the vertical stress  $\sigma_v = \gamma h$ . Here,  $\gamma$  is the fill unit weight and  $h$  is the depth from the top of the fill (Liu et al., 2016; Yang and Aubertin, 2017). With this method, the fill structure must meet the condition  $\sigma_v \geq \gamma h$  (Porathur et al., 2022). Additionally, the vertical stress of the fill structure is zero at the top of the fill to a maximum value of  $\gamma H$  at the bottom of the fill, whereby  $H$  being the overall height of the exposed fill. This method offers a CTB with strength that is proportional to depth in a linear manner.

The second design method is based on the analysis of cemented fill with an open face as a two-dimensional (2D) vertical slope ( $90^\circ$ ) and a linear sliding plane. However, it is applied to backfill material that is cohesive and frictionless, i.e.,  $\phi = 0$  with  $UCS = 2c$  ( $c$  is the fill cohesion). The limit equilibrium analysis of a 2D wedge

in a strength then yields  $UCS \geq \gamma H/2$  (Liu et al., 2016; Yang and Aubertin, 2017). The drawback of this method is that it does not consider the stabilisation effect of the confining walls, thus rendering the method conservative.

The two methods presented above neglect the lateral confinement along the sidewalls and may result in overconsumption of binder. They are thus perceived as overly conservative. This shortcoming has been partly overcome later by the solution proposed by Mitchell et al. (1982) discussed in the next sub-section.

### *2.10.2 Limit Equilibrium Wedge model*

In general, when the exposed area of the backfilled slope is continuously increased, a typical failure mode of shear sliding can be observed. This failure essentially presents itself in the form of a plane failure surface that dips outwards into the excavation (open slope). This then causes parts of the exposed filling body to move to the new slope. When the height of backfilling body is sufficiently large, a filling block with enough weight will be developed to overcome any resistance to sliding along a critical failure plane. The block's net weight acts as the driving force at the point of failure, while the cohesion and particle friction along the failure surface and at the side walls interact to provide the resistance to shear sliding (Yang et al., 2015).

Mitchell et al. (1982) developed a three-dimensional (3D) analytical method considering a limit equilibrium of a sliding wedge confined by three walls. This is illustrated in Figure 2.17 where  $H$ ,  $W$ , and  $L$  are the backfill height, width, and length respectively. The term  $c'$  represents the adherence cohesion along with the interfaces between the backfill and the side walls;  $\alpha = 45^\circ + \phi'/2$  is the angle between the wedge sliding and horizontal planes;  $\phi$  is the effective friction angle of the backfill.

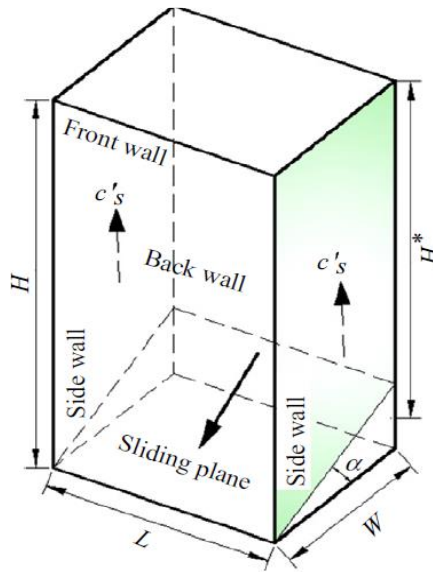


Figure 2.17 Wedge block mechanism proposed by Mitchell et al. (1982)

Subsequent to this, Mitchell et al. (1982) proposed Equation (2.7) in order to calculate the safety of factor of the backfill. In deriving the equation, the equilibrium of the wedge was considered and the backfill material was assumed to obey the Mohr-Coulomb criterion:

$$FS = \frac{\tan\phi}{\tan\alpha} + \frac{2cL}{H^*(\gamma L - 2c'_s)\sin 2\alpha} \quad (2.7)$$

The term  $c$  in Equation (2.7) denotes the effective cohesion of the backfill while  $H^* = H - (W \tan\alpha/2)$  is the block equivalent height of the wedge block. Assuming  $c'_s = c$ ,  $\phi = 0$ , and  $H \gg W$  (thus,  $H^* = H$ ) and  $FS = 1$ , UCS can be solved for (Mitchell et al., 1982):

$$UCS = 2c = \frac{\gamma H}{1+H/L} \quad (2.8)$$

Equation (2.7), known as limit equilibrium wedge model or also simply as Mitchell's model, have several limitations. The most important are listed below (Li, 2014a):

- The method cannot be applied to low and wide stopes but to high aspect ratio stopes (i.e.,  $H/B \geq \tan\alpha$ ).
- It assumes that the cohesion along the interfaces between the backfill and the sidewalls is equal to the cohesion of the backfill. This shortcoming was addressed later by Fall and Nasir (2010) who assumed that the cohesion of the interfaces is much smaller than the cohesion of the backfill.



- The method neglects shear strength by assuming that the material is frictionless, even though frictionless material only applies to undrained and consolidated material (Thompson et al., 2012). The shear strength of the interfaces between the backfill and the sidewalls as well as the back walls were also neglected.

Li and Aubertin (2012) modified Mitchell's model and proposed a solution that can be applied for both high and low height-to-width aspect ratio stopes. The modified model uses the same principle as in Mitchell's model by not considering the friction along with the backfill-rock interfaces. The modified model also considers the addition of a surcharge  $p_0$  on the backfill surface. And based on experimental tests, Li and Aubertin (2012) are able to show that the backfill-sidewall interface cohesion is proportional to that of the backfill:

$$c_b = r_b c \quad (2.9)$$

Where  $r_b = c_b/c$  is the adherence ratio of the backfill-sidewall interfaces; its value ranges from 0 to 1.

Li and Aubertin (2012) proposed for the adherence (cohesion) along the side walls to be estimated as a fraction of the backfill cohesion. And just like in Mitchell's model, the friction angle between the backfill and side walls and the shear strength (cohesion and friction angle) along the back wall are considered negligible (Li and Aubertin, 2012; Liu et al., 2016). This is also deemed a conservative approach to the problem. That is why, Li (2014a) proposed a generalised solution to address the identified limitations of Mitchell's modified model. The solution takes into account the shear strength along the two sides walls ( $\tau_s$ ) and the back wall ( $\tau_a$ ) by assuming that the walls are made up of different materials that may have different geotechnical properties from those of the backfill. The solution neglects the normal stress of the back wall so that the shear strengths of the back wall and side walls can be obtained respectively as follows:

$$\tau_a = c_a \quad (2.10)$$

$$\tau_s = c' + \sigma_h \tan \delta \quad (2.11)$$

Where  $c_a$  is the adherence cohesion along the back wall interface

$\delta$  denotes the friction angle along the interfaces between the backfill and the side wall.

Equations (2.10) and (2.11) can be applied to both low and high-aspect ratio stopes. Li and Aubertin (2014) also proposed an alternative solution that examined the upper rectangular block and a lower triangular wedge. The block is assumed to be moving vertically downwards while the wedge moves parallel to the sliding plane of the plane failure. The limitation of this model is the neglect of the internal shear stress along the interfaces between the rectangular block and the wedge. Another limitation is overlooking the effect of an additional exposed wall during the estimation of stress distribution on the backfill structure. This is corroborated by Rankine (2004) who stated that the major shortfall of the limit equilibrium methods is it is only valid for single-side exposure on a backfill structure, although stopes are usually exposed on a minimum of two 5/9 sides.

All the methods and refinements discussed so far were developed for a single-layered backfill mass. In practice, open stopes are filled with an initial pour called plug pour with high binder content; then, the last pour (also called final pour) is done with less binder content compared to the plug pour (Grabinsky et al., 2021). Li (2014b) proposed an analytical method to estimate the required strength of exposed backfill with a stronger plug pour. The method separately examines a stope when the sliding plane occurs within the plug pour and when the sliding plane intersects the top surface of the plug pour (Figure 2.18). The solution considers a stope with a high height-to-width ratio:  $H \geq H_p + B \tan \alpha$  where  $H_p$  is the plug thickness, and  $B$  represents the backfill width.

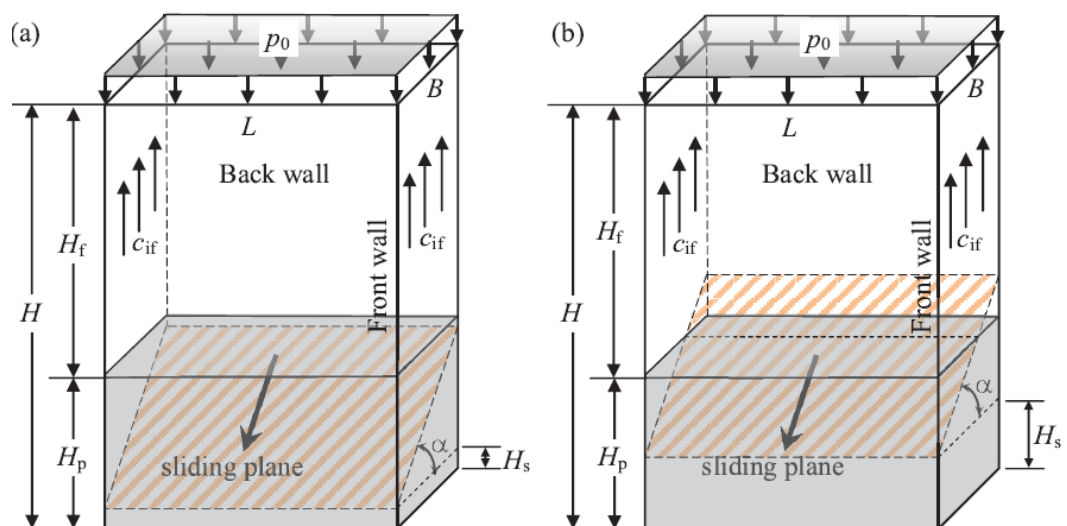


Figure 2.18 Backfill with a high height-to-width ratio containing plug pour at its base, when the sliding plane (a) remains within the plug, and (b) intersects the top surface of the plug

Li (2014b) therefore formulated his model by distinguishing two scenarios. In the first instance when there is a contrast in strength between the plug pour and the final pour, two possibilities can be considered: the sliding plane may either remain within the plug pour or intersect the top surface of the plug. Therefore, for a sliding plane within the plug pour, when the wedge block above the sliding plane is considered and the assumption that the material obeys the Mohr-Coulomb criterion, the safety factor of the exposed backfill is given by:

$$FS = \frac{\tan \phi}{\tan \alpha} + \frac{C_p L B}{w_n \sin 2\alpha} = \frac{\tan \phi}{\tan \alpha} + \frac{2 r_p C}{p_n \sin 2\alpha} \quad (2.12)$$

$$\text{Where } P_n = P_0 + \left( \gamma - \frac{2 r_{if} C}{L} \right) H_f + \left( \gamma - \frac{2 r_{ip} r_p C}{L} \right) H' \quad (2.13)$$

$$\text{And } H' = H_p - H_s - \frac{B \tan \alpha}{2} \quad (2.14)$$

The required backfill cohesion is estimated as follows:

$$2 c = \frac{p_0 + \gamma H_f + \gamma_p H'}{\frac{r_p}{FS - \tan \phi} \sin 2\alpha + r_{if} \frac{H_f}{L} + r_{ip} r_p \frac{H'}{L}} \quad (2.15)$$

Where  $P_0$  is the pressure due to surcharge on the top surface of the backfill

$H$  and  $L$  are the height and length of the backfill respectively

$H_f$  is the thickness of the final pour

$\gamma$  is the unit weight of the fill

$c$  and  $\phi$  represent the cohesion and friction angle.

The interpretation of the symbols in Equation (2.15) remains the same regardless of the subscripts ( $p$  or  $f$ ) attached to it. These subscripts  $p$  and  $f$  refer to plug and final pour respectively. When the plug is of the same properties as the final pour, this means that the unit weight  $\gamma_p$  of the plug pour is similar to that of the final pour  $\gamma_f$  and that the interface adherence ratio of the plug  $r_p = 1$ . Moreover, the interface adherence ratio of the plug with the side walls  $r_{ip}$  is equal to that of the final pour with the sidewall  $r_{if}$ . And if the elevation of the line of intersection between wedge-sliding and front-wall planes is zero; then, Equation (2.12) reduces to:

$$FS = \frac{\tan \phi}{\tan \alpha} + \frac{2 c}{\left[ p_0 + \left( \gamma - \frac{2 r_{if} C}{L} \right) + \left( H - \frac{B \tan \alpha}{2} \right) \right] \sin 2\alpha} \quad (2.16)$$

And Equation (2.15) reduces to:

$$2c = \frac{P_0 + \gamma \left( H - \frac{B \tan \alpha}{2} \right)}{\left[ \left( FS - \frac{\tan \phi}{\tan \alpha} \right) \sin 2\alpha \right]^{-1} + \frac{r_{if}}{L} \left( H - \frac{B \tan \alpha}{2} \right)} \quad (2.17)$$

Equations (2.16) and (2.17) correspond to the modified Mitchell's solution for the case of backfilled slope having a high height-to-width ratio. By considering  $P_0 = 0$ ,  $\phi = 0$ ,  $r_{if} = 1$ ,  $H \gg B$ , and  $FS = 1$ , Equation (2.16) further reduces to Mitchell's original model (i.e., Equation 2.7).

The second scenario presented by Li (2014b) refers to the formulation whereby the sliding plane is intersecting the top surface of the plug pour. In this case, the factor of safety can be expressed as follows:

$$FoS = \frac{\tan \phi}{\tan \alpha} + \frac{\tan \alpha + (r_p - 1) \left( \frac{H_p - H_s}{B} \right)}{(\sin \alpha)^2 p_0 + \left( \gamma - \frac{2 r_{if}}{L} c \right) H^* + \left( \gamma_p - \frac{2 r_{ip} r_p}{L} c \right) \frac{(H_p - H_s)^2}{2 B \tan \alpha}} \quad (2.18)$$

$$\text{Where } H^* \text{ is given by } H^* = -H_f - \frac{(2 B \tan \alpha - H_p + H_s)^2}{2 B \tan \alpha} \quad (2.19)$$

The required cohesion can be estimated as follows:

$$c = \frac{p_0 + \gamma H^* + \gamma_p \frac{(H_p - H_s)^2}{2 B \tan \alpha}}{\frac{\tan \alpha + (r_p - 1) \frac{H_p - H_s}{B}}{\left( FS - \frac{\tan \phi}{\tan \alpha} \right) \sin^2 \alpha} + \frac{2}{L} \left[ H^* + r_{ip} r_p \frac{(H_p - H_s)^2}{2 B \tan \alpha} \right]} \quad (2.20)$$

In a similar fashion, if the plug pour has the same properties as the final pour (i.e.,  $\gamma_p = \gamma$ ,  $r_p = 1$ , and  $r_{ip} = r_{if}$ ) and again if the elevation from the bottom of the plug pour to the line of intersection between the wedge and the sliding plane  $H_s = 0$ ; then, Equations (2.18) and (2.20) reduce to Equations (2.16) and (2.17) respectively.

It should be stressed that the solutions proposed by Li (2014b) adopted the same approach and assumptions as Mitchell's model. To put it simply, the shear strength along the two side walls (i.e., the friction angle of the backfill-sidewall interface) is deemed negligible. The same is assumed for the contact between the back wall and the backfill. In other words, the cohesion and the friction angle of the backfill-back wall interface are also negligible.

Zhou et al. (2019) also proposed an analytical solution that incorporates the arching effect for both uniform and non-uniform backfill strength. For the purpose of this thesis, suffice it to say that the solution is based on Morgenstern's method

and some modified differential slice methods used to evaluate the stability of soil slopes. The vertical fill body is divided into differential vertical slices; then, the vertical stress at the bottom of each slice is measured. For a given cohesion and angle of internal shear, the solution provides a prediction of the safety factor.

In closing, the methods discussed here rely on a simplified stope geometry, i.e., the underground stope is taken as a vertical rectangular block whereas in practice, it is usually irregular and inclined (Wang et al., 2021). These methods also do not consider the effect of blasting vibrations on the adjacent backfill pillar. Finally, back wall closure is ignored so that the contact between the back wall and backfill mass is negligible. The next sub-section looks at the problem empirically and expounds on the stability graphs applied in open-stope design.

### *2.10.3 Stability charts for open stope design*

In the mining industry, there is a prevalent pressure to maximise reserves and increase revenue by reducing operational costs. Cost-cutting methods include the reduction of stope dilution and the optimisation of ore recovery. To this end, backfill is usually exposed either vertically or horizontally when placed in the underground open stopes. As such, the backfill body must be strong enough not to fall into the recently opened stope when blasting and mucking occurs. Otherwise, the backfill body will fail and causes dilution into the stope (Veenstra, 2015). It is important to design the backfill body with the size of vertical exposure and expected dilution in mind. The present and subsequent sub-sections discuss the various empirical stability charts developed for the purpose. They are mostly based on the Mathews stability charts (refer amongst other to Potvin, 1988; Nickson, 1992; Potvin and Milne, 1992; Hadjigeorgiou, 1995). As the name states, this first stability graph was introduced by Mathews et al. (1981) based on 50 mining cases. It is the most frequently used method for managing dilution and stope stability (Jang, 2014). The method can provide optimal stope dimensions with low mining costs at a depth lower than 1000 m (Papaioanou and Suorineni, 2016). By using the Mathews stability chart, the stability of the stope can be classified as stable, potentially unstable, or potentially caving as shown in Figure 2.19 with the three stability zones separated by transition zones.

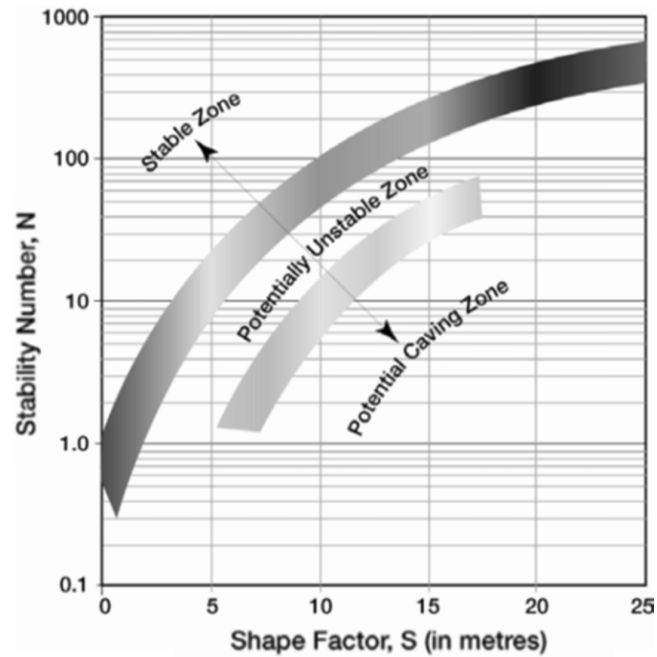


Figure 2.19 Mathews stability chart showing the three stability zones (Mathews et al., 1981)

The chart relies on two calculated variables to characterise stability: the Mathews stability number and the shape factor. The Mathews stability number ( $N'$ ) denotes the ability of the rock mass to remain stable under certain stress conditions. On the other hand, the shape factor ( $S$ ), also known as the hydraulic radius, represents the surface geometry of the slope (Mawdesley et al., 2001; Kang et al., 2019). The principal concept behind the stability graph is that the size of an excavation surface can be related to the rock mass competency to indicate stability or instability.

As depicted in Figure 2.19, the stability number on the y-axis is plotted against the shape factor on the x-axis. If the estimated data point falls in the stable zone, it means that the surface of the slope has a high probability of being stable. In the unstable zone, there is a high probability that the surface will fail but the stability can be improved by ground support. If the slope surface lands in the caving zone, there is a high chance that 30% of the surface will slough. The “caving” term in the caving zone does not necessarily mean that the slope will cave in.

In terms of application, the stability number is calculated as follows:

$$N' = \left(\frac{RQD}{J_\eta}\right) \times \left(\frac{J_r}{J_a}\right) \times A \times B_1 \times C \quad (2.20)$$

Where  $RQD$  represents the rock quality designation;  $J_\eta$  denotes the joint set number;  $J_r$  is the joint roughness number;  $J_a$  is the joint alteration number;  $A$ ,  $B_1$

and  $C$  represent the stress factor, the joint orientation factor, and the gravity factor respectively. The empirical charts to determine  $A$ ,  $B_1$ , and  $C$  are presented in Figures 2.20 – 2.22. The product of  $\left(\frac{RQD}{J_n}\right) \times \left(\frac{J_r}{J_a}\right)$  is defined as the modified tunnelling quality ( $Q'$ ) by Mathews et al. (1981). The authors assumed that the joint water reduction parameter and the stress reduction factor are both equal to one.

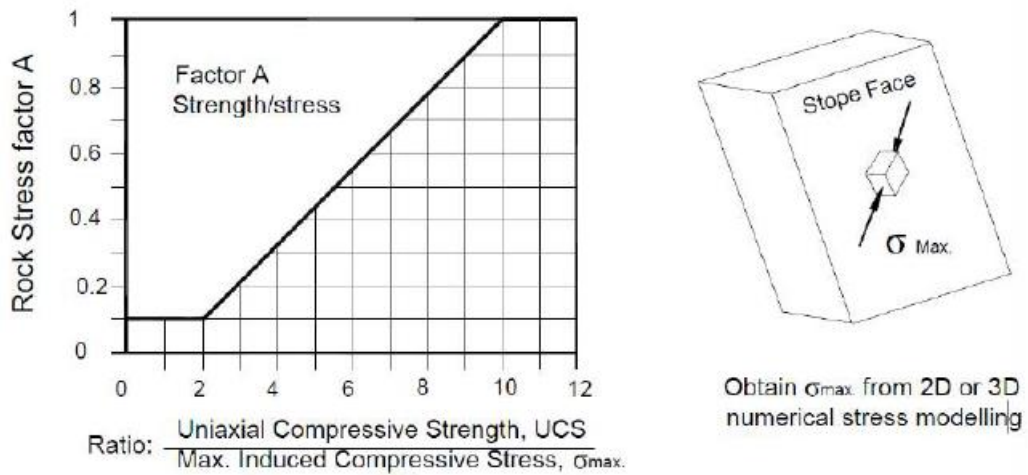


Figure 2.20 Graphical determination of stress factor  $A$  (after Potvin, 1988)

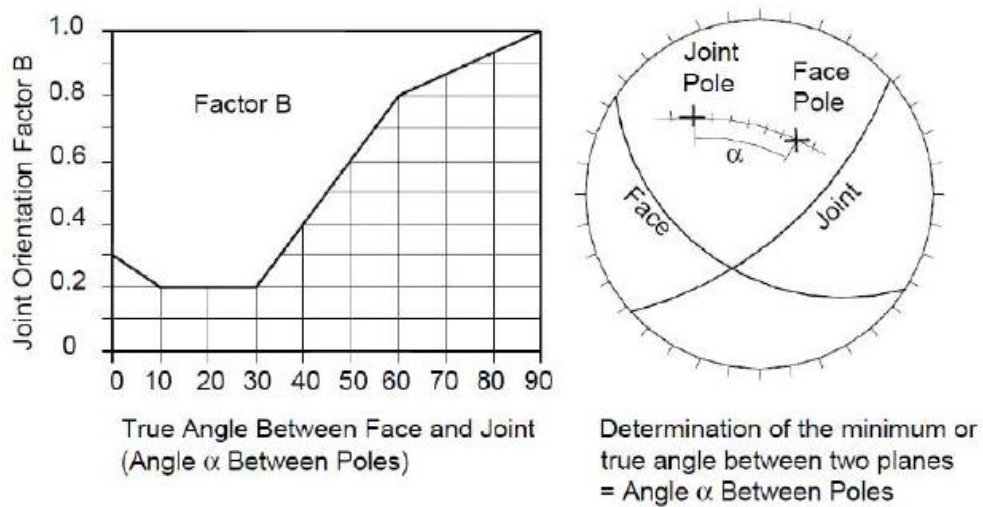


Figure 2.21 Graphical determination of joint orientation factor  $B$

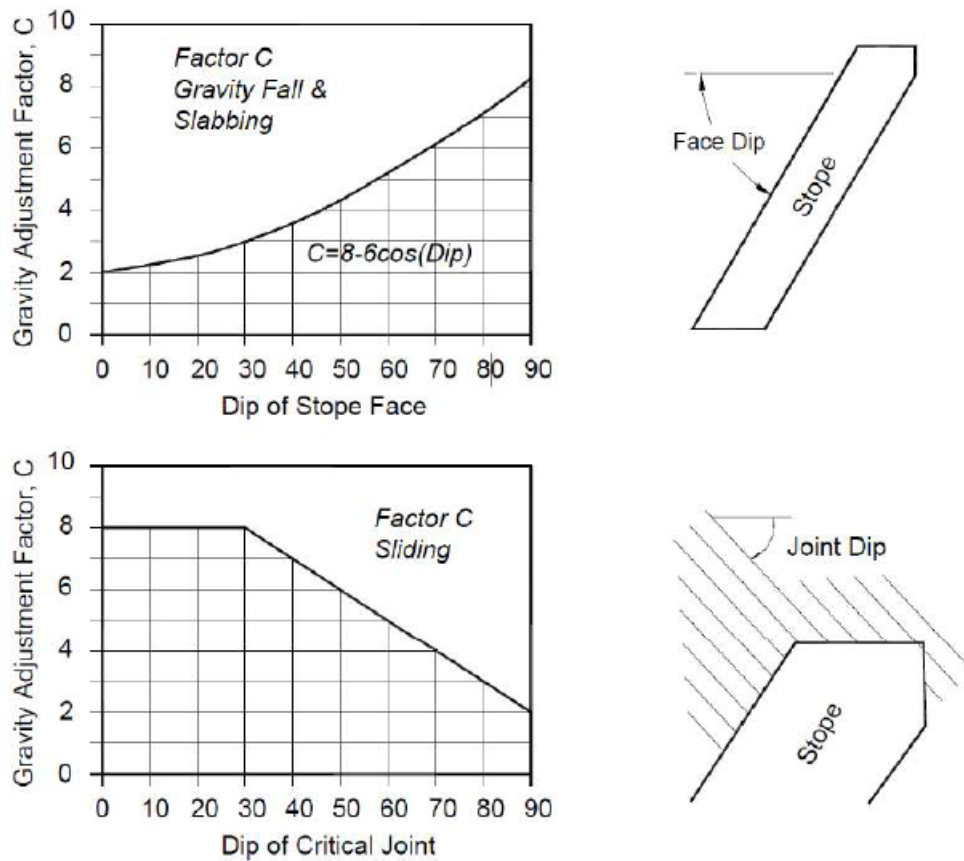


Figure 2.22 Graphical determination of gravity adjustment factor  $C$  (after Potvin, 1988)

Finally, the shape factor/hydraulic radius ( $S$ ) is defined as the area of the stope surface divided by the length of its perimeter. The area and perimeter of the stope are respectively determined through the application of the general mathematical formula for area or perimeter of a square or rectangle, depending on the shape of the stope.

#### 2.10.4 Modified Mathews stability charts

Since the inception of the Mathews stability graph, several authors (Potvin, 1988, Nickson, 1992; Stewart and Forsyth, 1995; Hadjigeorgiou et al., 1995) have made a significant contribution to the modification of the method to improve its reliability. For example, with more than 170 case studies, Potvin (1988) modified the Mathews stability graph by reducing the number of stability zones. Figure 2.23 shows the stability graph by Potvin (1988) with only two stability zones: stable and caved zones separated by a transition. Potvin also modified the way of calculating the rock stress, joint orientation, and gravity adjustment factors. Nonetheless,



Mathews and Potvin's stability graphs were found to be limited because they could only be applied to Canadian mines (Mawdesley et al., 2001). Additionally, the original stability graph was designed for large 'non-entry' stopes (Papaioanou and Suorineni, 2016).

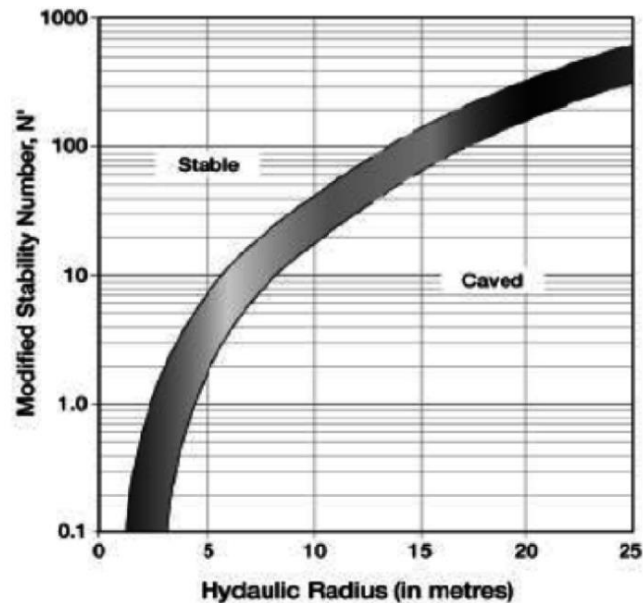


Figure 2.23 Modified stability graph by Potvin using the modified stability number (after Potvin, 1998)

The modified stability graph by Potvin (1988) was further refined by Nickson (1992) statistically using discriminant analysis. Nickson (1992) posited that Potvin's transition zone can be only used for the design of unsupported stopes (Mawdesley et al., 2001). He incorporated zones (stable/unstable) for cable bolt design as shown in Figure 2.24 and applied the Mahalanobi's distance to separate the two zones. Further modifications were made when Stewart and Forsyth (1995) criticised Potvin's stability graph by arguing that the method is non-rigorous. To improve the validity of the Mathews stability graph, Stewart and Forsyth (1995) added a fourth zone named a possible significant failure zone separated by three transitions as depicted in Figure 2.25. The authors employed Laubscher's caving stability graph in their modernized version to approximate the position of the potential caving line.

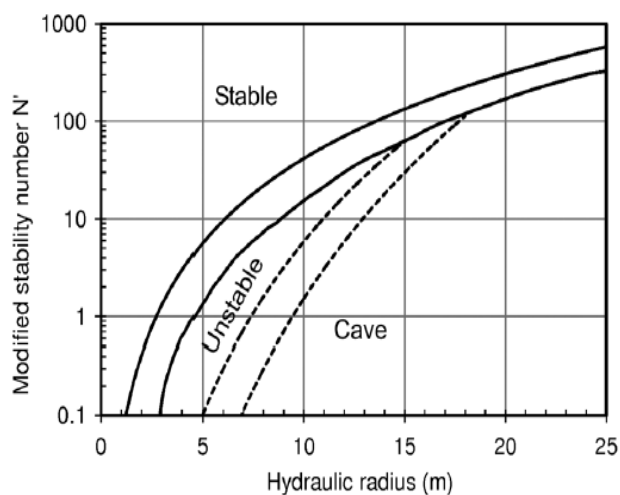


Figure 2.24 Stability graph incorporating cable bolt (Nickson,1992)

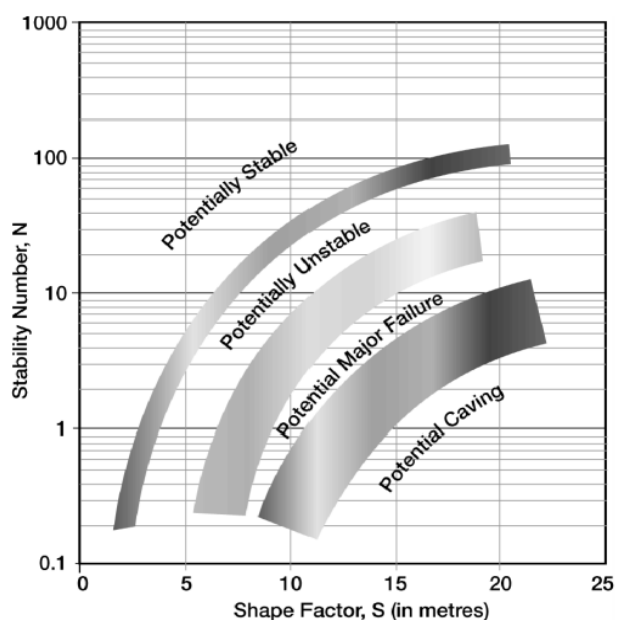


Figure 2.25 Modified stability chart by Stewart and Forsyth (1995)

According to Suorineni (2012), Hadjigeorgiou et al. (1995) developed another stability graph just after Stewart and Forsyth (1995). To develop this new graph, the authors applied discriminant analysis to design a partial statistical definition of stable/unstable zones and obtained similar results. Figure 2.26 depicts the stability graph by Hadjigeorgiou et al. (1995) that includes a stability zone in which cable bolting may effectively be utilized to provide back support.

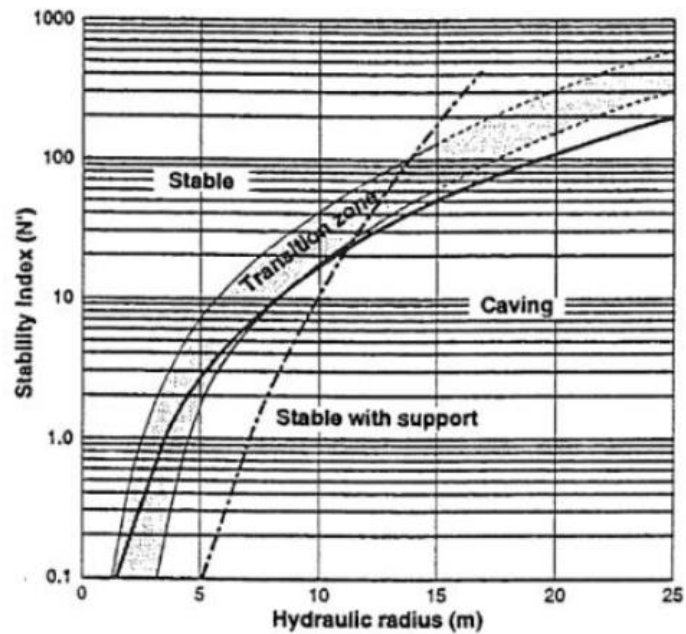


Figure 2.26 Modified stability graph by Hadjigeorgiou (1995)

The 50 case studies by Mathews were extended to 485 by Mawdesley et al. (2001). The authors considered a variety of slope geometries and rock mass conditions, thereby increasing the reliability of the Mathews stability chart. These cases were validated by Trueman and Mawdesley (2003) and roughly 100 cases from the database had uncertainties and therefore, were removed in the final version of their modified stability graph. Their results are illustrated in Figure 2.27 which considers four stability zones; namely, stable, failure, major failure, and caving. This extended Mathews stability graph allows for individual cases to be distinguished as well as presents the increased range of shape factors captured within the stability database.

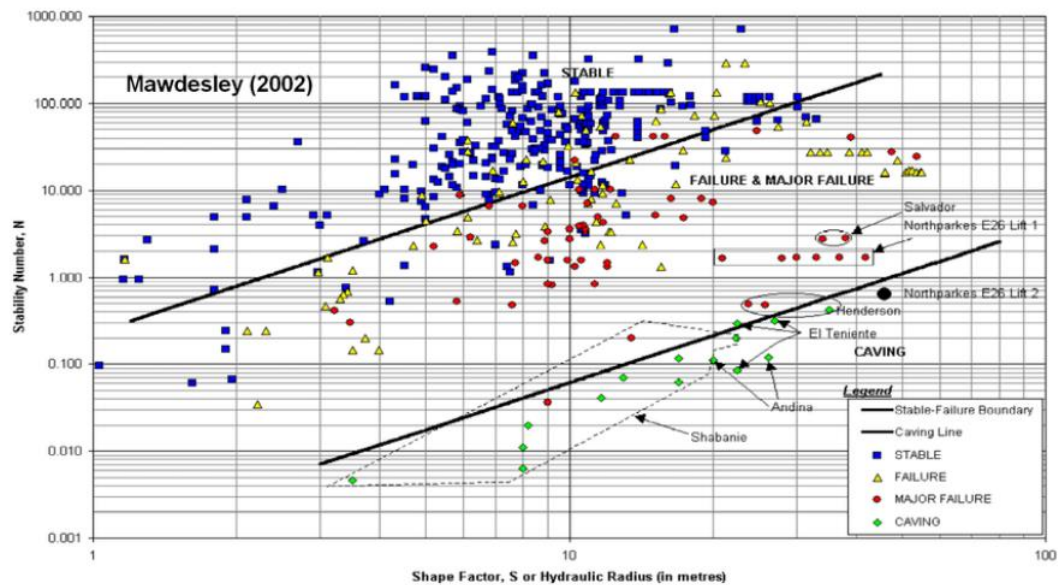


Figure 2.27 Extended Mathews stability graph by Trueman and Mawdesley (2003) Regardless of the reputation of the stability graph methods, certain limitations have been noted. They are summarised below (Jang, 2014; Suorineni, 2010; Papaioanou and Suorineni, 2016; Potvin and Hadjigeorgiou, 2001):

- Complex stope geometries are often oversimplified
- The effect of blasting on the surrounding rock mass
- Backfill surface stability is not accounted for; it is assumed that all stope surfaces are in-situ rock
- Stand-up time is not considered, i.e., the exposure period of the stope wall is neglected
- Effects of faults are not considered
- The design of stability zones and assessment of stope stability is subjective
- They cannot be applied to rock-burst conditions.

### 2.10.5 Dilution-based stability graph

Various factors can affect a mine's productivity, but ore loss and dilution are recognised as the most significant. Henning and Mitri (2007) define unplanned dilution as *any waste material derived from rock or backfill outside the stope boundaries due to blast-induced overbreak, sloughing of unstable wall or backfill*. Hence, there are quantitative methods used to assess stope performance based on the level of dilution incurred. For example, Clark and Pakalnis (1997) developed

a dilution design graph which is the most preferred method due to its simplicity and reliability. The graph is based on the concept of equivalent linear overbreak slough (ELOS) and is used to quantify the level of unplanned dilution generated as a result of instabilities within the stope (Suorineni, 2010).

ELOS can be defined as follows (Henning and Mitri, 2007)

$$\text{ELOS (m)} = \frac{\text{Volume of measured overbreak}}{\text{Area of stope surface}} \quad (2.21)$$

The limitation of the ELOS stability graph is that the database used for the purpose is primarily from narrow vein mines. However, the method can be used for narrow and wide orebodies provided that ELOS is converted to percent dilution. An example by Papaioanou and Suorineni (2016) outlines that for a hangingwall ELOS of 0.5 m in a 1 m wide orebody the dilution is 50% while a dilution of 5% is also possible for a 10 m wide orebody with the same ELOS. Equation (2.22) provides a means of converting ELOS values into percent dilution:

$$\text{Dilution (\%)} = \frac{\text{ELOS}}{\text{Orebody width}} \times 100 \quad (2.22)$$

A dilution graph presented in Figure 2.28 illustrates the estimation of dilution where a plot of stability number and hydraulic radius of a stope meet. The dilution zones are interpreted as follows:

- (1) ELOS < 0.5 m means no blast damage;
- (2) 0.5 m < ELOS < 1.0 m means minor sloughing;
- (3) 1.0 m < ELOS < 2.0 m is for moderate sloughing and (4) ELOS > 2.0 m denotes severe sloughing or possible wall collapse.

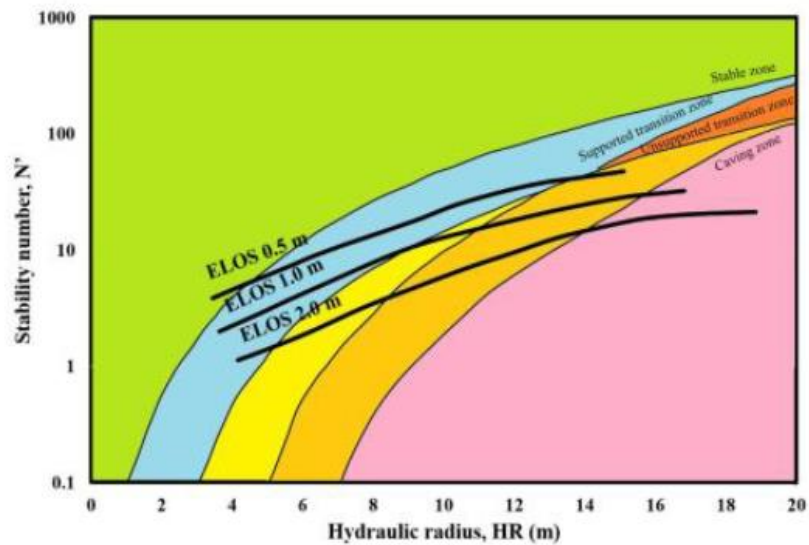


Figure 2.28 ELOS lines superimposed on the Potvin-Nickson graph (after Clark and Palaknis, 1997)

### 2.10.6 Numerical methods

This section reviews past studies in the numerical analysis of the strength of CTB. From the perspective of mine tailings, Seneviratne et al. (1996) are amongst the first to develop a one-dimensional finite element method (FEM) code called MinTaCo capable of simulating the consolidation and evaporation behaviour of slurried mine tailings. Since then, the method has been widely used to improve CTB design by incorporating various processes that contribute to the strength development of CTB. For example, Helenski et al. (2007) have developed a model based on MinTaCo to describe the consolidation of CTB. Their model was named CeMinTaco with the “Ce” denoting the addition of cement into the tailings. It is because of the addition of cement that the numerical tool considered the effect of cement hydration in the consolidation of CTB.

Nasir and Fall (2010) developed a model to predict the UCS development of undrained CTB structures using the FLAC 3-D tool. The authors studied the effect of stope size by selecting a range of 2.5 m by 5 m, 5 m by 10 m, and 10 m by 20 m. Other variables considered are CTB temperature of 20°C and backfilling rate of 2.5 m per day. The model successfully predicted the strength development of CTB for three different mix characteristics.

Due to the lack of a model to simulate the thermo-hydro-chemical process of CTB, Wu et al. (2014) developed a FEM model to predict and describe the coupled thermal and hydraulic processes that take place within CTB. The limitation of this model is that it does not consider the mechanical factors (i.e., confining pressure, self-weight pressure) acting on the CTB. Therefore, to close this gap, Cui and Fall (2015) developed a thermo-hydro-mechanical-chemical model to study the coupled processes and the resulting influence on the properties and behaviour of CTB. The results from the model were successfully validated against the laboratory experiments.

Another worth-mentioning numerical study was done by Liu et al. (2017) using the Particle Flow Code (PFC) 2-D to simulate the stress-strain behaviour of CTB. This discrete element model incorporates the particle description of tailings and cement particles. The model uses the true particle size distribution of tailings to simulate the tailings particles and the bond between cement and tailings particles. Other input variables include void ratio, the normal and shear stiffness of the tailings and the ratio between the bulk modulus and shear modulus as the main component of tailing. The limitation of the model is that it assumes that the stiffness of the cementing materials is the same as the tailings. The reproducibility of the stress-strain curve is also not guaranteed due to the circular grain used in the PFC 2-D.

Yu et al. (2018) analysed the effects of mechanical properties (for example, friction angle, Poisson's ratio, elastic modulus) on the stress distribution of backfilled stopes. The authors used stope dimension of  $H = 45$  m,  $B = 6$  m and the space from the top of the backfill to the hanging wall is 0.5 m. FLAC was used to create the numerical model and the backfill was modelled in 5 layers with a thickness of 9 m. The overall depth is set to be 250 m while the rock mass is assumed to be homogeneous, isotropic and linearly elastic. The results of the model are depicted in Figure 2.29 where a non-uniform stress distribution across the stope is displayed using several colours. The intensity of the stress is colour-coded with 0 MPa highlighted in blue and the stress increases in ascending order until 240 MPa in red. The results show that the higher the aspect ratio of the backfilled stope, the greater the vertical stress.

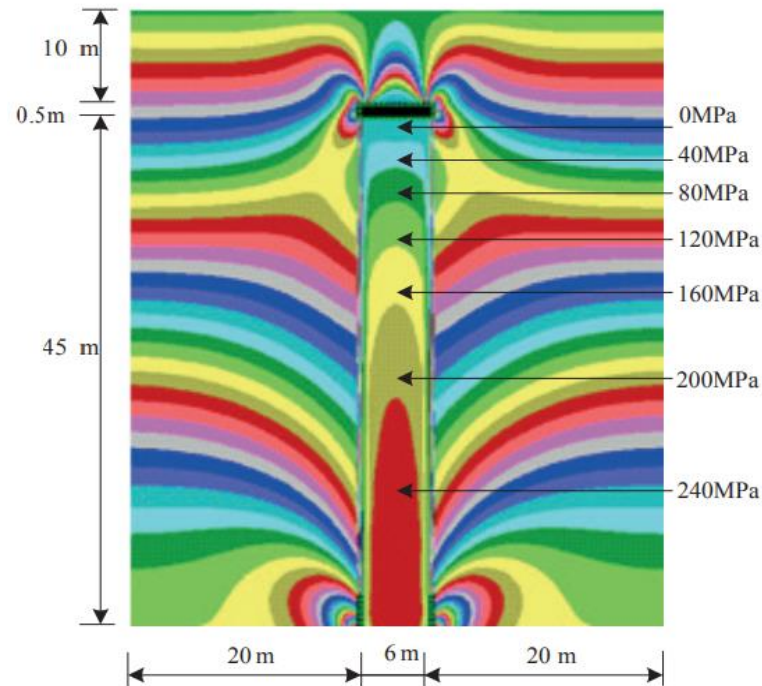


Figure 2.29 Vertical stress distribution contours within backfill and surrounding rocks (after Yu et al., 2018)

### 2.11 Successful and failures of backfill stopes – Case studies.

The strength design of backfill is encouraged to ensure the safety of mine personnel through effective ground support. Insufficient strength of the CTB structure can lead to stope failures when the hanging wall confining pressure exceeds the UCS of the backfill. For instance, the collapse of the backfilled stope in an undisclosed gold mine in Jilin, China (Chang et al., 2021). The required strength of the CTB after 28 days is 0.8 MPa. The gold mine uses tailings purchased from another mine since their tailings are highly concentrated with cyanide. Moreover, the filling timeline is increasing with the mining, so the slurry concentration needs to be reduced to achieve gravity transportation. Consequently, a high dosage of cement must be added to achieve the expected CTB strength, thus, leading to high operational costs. Alas, the quality of the CTB in use that the mine can only reach 0.76 MPa at 28 days when the cement content is 10%, which has led to many collapses in the mine. Notably, Chang and his colleagues did an experimental study to improve the strength of the CTB by adding fly ash into the mixture, thereby, reducing cement cost.



A study by Han et al. (2019) reported that frequent failures of backfilled stopes occurred at Jinying Gold Mine due to a low-strength CTB body. The Jinying Gold Mine is located in cold regions of Baishan City, Jilin Province. The annual temperatures around the mine area range between  $-3^{\circ}\text{C}$  to  $7^{\circ}\text{C}$ . The mine uses a high sublevel subsequent filling mining method and the stability of the backfill is essential when mining the adjacent secondary stope. To improve the strength of the CTB in this mine, Han et al. (2019) studied the effect of temperature on the strength development by reflecting on cement hydration, backfill microstructure, evaporation and drying rate of the slurry. The authors were able to improve the strength of CTB by 129% through thermal insulation and heated water application and underground ventilation.

A case related to surface subsidence was reported in Longshou Mine (Ding et al., 2018). Longshou Mine is a large Nickel underground mine located in Gansu Province, China. The extraction method employed by the mine is cut-and-fill mining due to high in-situ stresses. Sudden violent caving of the hanging wall occurred at the mine resulting in air blasts and ground vibration. The scale of the collapse extended up to  $11\ 000\ \text{m}^2$ , which is a major threat to life and mine equipment. The cause of the caving was fault slip; as a result, the fill around the fault lost strength (Ding et al., 2018). The backfill body could self-support itself for only some time until it failed. This is because the backfill is softer than the surrounding rock mass. The difference in mechanical properties between the fill and the rock mass can cause stress transfer and redistribution between both materials (Sivakugan et al., 2014).

## 2.12 Closing comments

The use of CTB as a means of ground support has gained popularity and it seems that its use will continue to grow exponentially. It is evident from the literature reviewed that backfill must be self-supporting and be able to remain standing during the excavation of the adjacent stope. The stability of the exposed backfill can only be assured once the secondary stope has been backfilled, thus, it offers confinement to the primary stope. While there are proposed solutions for high height-to-width stope ratios, there is little to no evidence of any published literature documenting the successful or unsuccessful implementation of these solutions to layered CTB. The same can be said regarding the numerical investigations of

stress distributions for layered backfill. Indeed, while most studies focus on simulating the coupled effects of the hydro-thermal-mechanical-chemical process on the mechanical properties of CTB, some only cover the effects of only two or three processes. Thus, the study of the mechanical properties of layered CTB is utterly rare, which is the main objective of this study.

### 2.13 Summary and future work

This review has shed some light on the future of research on CTB. The articles assessed in this review provided some insights into the knowledge gap for future consideration. For example, it cannot be deduced how saturation affects the strength of CTB. Based on the reviewed articles, it can be deduced, from the perspective of the long-term effect that saturation reduces the strength of CTB. Although it has been reported to increase the strength of CTB at the first stages due to cement hydration, other findings show that cement hydration consumes pore water, thus hardening the CTB. It is thus, recommended that the effect of saturation on the short-term (i.e., at an early age) strength of CTB be studied to clarify this confusion.

Furthermore, the literature reveals that ordinary Portland cement (OPC) is not resistant to sulphate attack. It is for this reason that other alternatives such as fly ash, alkali-based slag and other pozzolanic cement are used in high sulphide tailings. Although it has been reported that fly ash or furnace slag can reduce cement consumption, the unanswered question from the literature is whether it can provide competitive strength as OPC. This conclusion is derived from the various findings that the UCS was observed to either increase or decrease when fly ash or furnace slag was used. This conflicting finding is attributed to the different mineral compositions of the binders according to where they were sourced.

The effect of stope height on the strength of backfill is still not well understood. The performance of multiple-layered backfill is different from a single-layered one, therefore, the same method of designing a backfill cannot be applied to both. The numerical solutions to analyse the stability of backfill stopes also have their limitations. That is, they do neglect the effect of geological discontinuities such as faults and the effect of layering in large stopes. On the other hand, the published findings on the difference in mechanical properties between single-layered and

multiple-layered have recently been brought to attention. This explains the paucity of documented work in this area. Thus, more room for exploration has been opened from the perspective of research and innovation. This study is anticipated to close some of the gaps and contribute to the development of charts that considers the layering of CTB. The following chapter presents the procedures adopted in the collection of empirical data in view to achieve the objectives set out for this doctoral research study.

## Chapter 3 Data collection procedure and research methodology used

This chapter discusses the experimental design, procedure, and equipment used to collect empirical data. Moreover, the steps followed to develop the simulation model are described. Lastly, the challenges encountered as well as associated remedies are detailed.

### 3.1 Introduction

The experimental work carried out as part of this doctoral study entailed measurements of the particle size distribution (gradation curve), Atterberg's limits, X-ray fluorescence profile of the tailings. Cemented tailings backfill samples were also meticulously prepared by casting and curing before UCS testing was done. To complement the experimental data, Finite Element Method (FEM) was used to develop the numerical simulation model aimed at predicting the backfill support behaviour with different layers. FEM analysis was used because it is considered to be the most appropriate numerical method for continuum material (Sengani and Mulenga, 2020). The model was built to study the variation of the strength of backfill as the layers increase.

In the first phase of the research work, gold-bearing tailings material was collected in bulk from a selected site. The collected bulk material was analysed for particle size distribution to determine the grading of the tailings. This was followed by determining Atterberg's limits to classify the plasticity of the tailings. The second phase involved preparing the CTB using tailings, cement and tap water. The CTB slurry was subjected to a slump test to ascertain the consistency of the material prepared. Thereafter, the slurry was moulded and cured for a maximum of 28 days. Throughout the entire curing period, the CTB cubes were subjected to UCS tests after 7 days, 14 days, 21 days and 28 days as per the experimental design generally used in mining and civil engineering research. The last phase of the work was centred on the development of the FEM simulation model. The subsequent sections cover in detail the three phases of the research work succinctly introduced above.

### 3.2 In-situ collection of the bulk tailings sample

The tailings were collected from a mine dump located on the southern side of Johannesburg, South Africa, alongside the coordinates  $26^{\circ}13'16.6''\text{S}$   $28^{\circ}01'42.4''\text{E}$  shown on the map in Figure 3.1 9 (circled in red). Old dry tailings from a gold mine were used in this doctoral study. South Africa has several gold tailings dumps that are openly accessible. The tailings used in this study were selected randomly to save costs. Other types of tailings required a need of transport to other provinces which would be more expensive when opposed to traveling in Johannesburg.

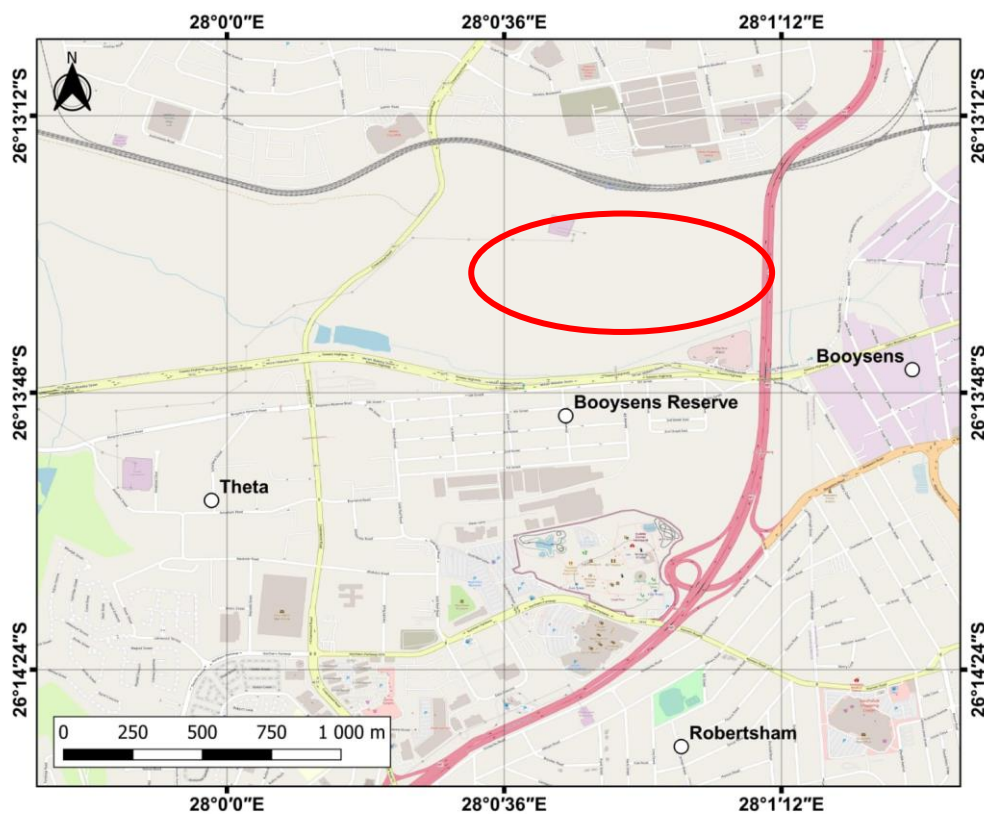


Figure 3.1 Location of tailing dumps where the samples were collected; coordinates:  $26^{\circ}13'16.6''\text{S}$   $28^{\circ}01'42.4''\text{E}$  (Google Maps)

The samples were collected according to the American Society for Testing and Materials (ASTM) D75 standards. The upper layer was scraped off by about 20 cm deep and discarded since this layer may be contaminated by foreign materials through water deposition. A shovel was used to dig the tailings from the top, middle and bottom of the pile. These samples were collected randomly from different points in the stockpile to at least have a representative sample of the tailings

stockpile. About 9 points were randomly selected on the pile to collect the tailings. A 25 kg container was used to pour the samples into plastic bags and later transported to the laboratory storeroom (see Figure 3.2). The tailings were not consistent throughout the pile, i.e., the hardness and colour of the material were different at the top layer as compared to the bottom of the pile. The tailings were brittle at the top but was lumpy and difficult to dig through at the bottom. The colour of the tailings was yellowish at the top due to the chemical reaction when exposed to oxygen and water. However, the tailings at the bottom were brownish like the natural colour of soil. In total, nine (9) bags weighing an average of 50 kg each were collected from the pile.

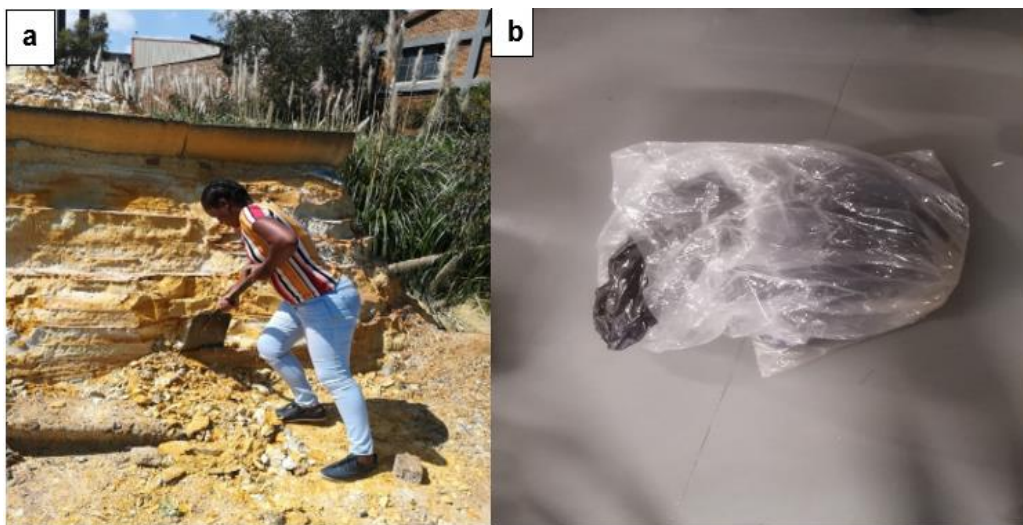


Figure 3.2 (a) Collecting tailings samples; and (b) Samples stored in refuse bags

### 3.3 Laboratory experiments

Upon collecting the bulk samples from the identified site, these were prepared for characterisation. This section details the experimental tests carried out at the laboratory facility. The laboratory tests include sieving, Atterberg's limits, XRF analysis, and slump test. The experiments, on the other hand, entail the preparation and UCS tests of CTB specimens also covered in this section.

#### 3.3.1 Particle size distribution

Particle size distribution was carried out to separate particles into different size ranges and to determine the mass of particles in each range. The test was done

as per the ASTM D6913 standards. As highlighted in Sections 2.3 and 2.8.1, the size of particles of tailings affects the behaviour of CTB (Cheng et al., 2020; Qi and Fourie, 2019; Wu et al., 2018); hence, the importance of conducting this type of test.

The following tools and equipment were used for particle size analysis: a stack of sieves of different sizes in descending order (i.e., 50 mm, 28 mm, 20 mm, 14 mm, 5 mm, 2 mm, 0.425 mm and <0.425 mm); a pan at the bottom of the sieves; a plate; a weighing scale; and a drying oven.

The samples were placed in an oven and dried overnight at 110°C for 24 h as shown in Figure 3.3. Before starting with the sieving, the sieves and the pan were cleaned and stacked. The sieves were arranged from top to bottom starting with a 50 mm sieve and ending with a less than 0.425 mm sieve. The dried sample was weighed on the scale, poured into the 50 mm sieve and gently shaken by hand before pouring another portion. The dried sample was sieved through a stack of sieves on a shaker for 20 min. The tailings retained on each sieve were collected onto various plates and weighed. The masses from individual sieves were used to calculate the fraction of material passing through each sieve as a percentage of the total sample. The results were used to develop a gradation curve or particle size distribution for the tailings material similar to Figure 2.3.

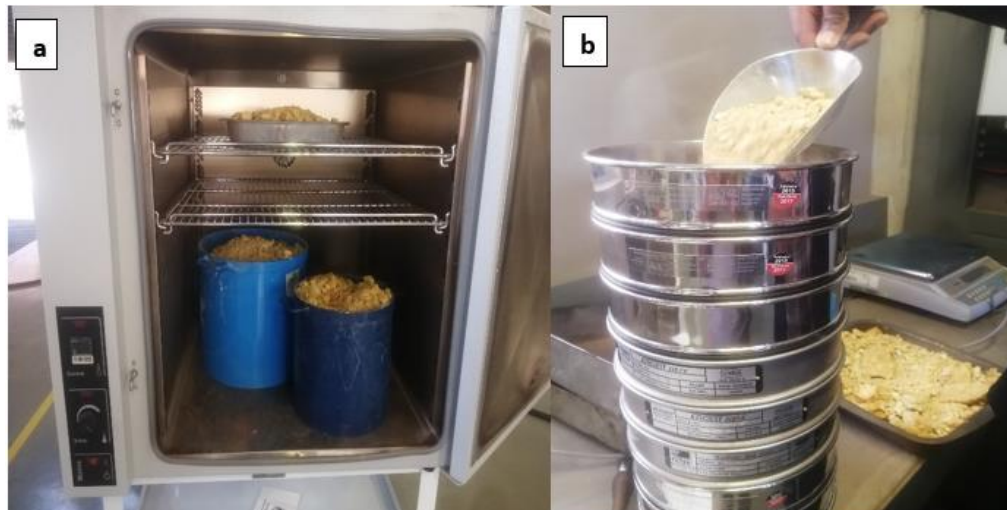


Figure 3.3 (a) Tailings placed in an oven for overnight drying; and (b) Putting tailings in a stack of sieves.

Finally, the coefficient of uniformity ( $C_u$ ) and curvature ( $C_c$ ) using Equations (2.2) and (2.3) were extracted from the gradation curve.

The next section discusses the process followed to conduct the Atterberg tests on the tailings material.

### 3.3.2 Atterberg's limits

Atterberg's tests were done to determine the liquid limit (*LL*) and plastic limit (*PL*) of the tailings according to the ASTM D4318 standards. The objective of these tests is to classify the characteristics of soil material in terms of its liquidity, plasticity, and solidity (refer to Figure 2.2).

The liquid limit is the water content at which the tailings change from a liquid to a plastic state (Balegh et al., 2020; Chen and Lin, 2009; Hong et al., 2012). The Casagrande cup method was used to determine the liquid limit of the tailings. The types of equipment required for this test are shown in Figure 3.4. Nonetheless, for the full test, a Casagrande liquid limit device, a grooving tool, a water bottle, mixing dishes, a spatula, and a drying oven are required.



Figure 3.4 (Left) Equipment used for the limit liquid test: (a) water bottle, (b) mixing bowl, (c) spatula, (d) weighing scale (e) Casagrande's cup. (Right) Tailings sample is split at the centre to observe the closing gap when tapping.

The cup was lifted and then dropped from a 10 mm height using the crank-operated cam. The oven-dried tailings particles that passed through the 0.425 mm were weighed to exactly 100 g. The tailings were poured into a mixing dish, few drops of water were gradually poured while mixing the tailings using a spatula. When the tailings seemed a bit moist, the mixture was transferred into the cup and divided into two portions using a grooving tool. The device was then cranked at 2 revolutions per second until the two halves of the soil pat come into clear contact



of about 13 mm long at the bottom of the groove. The gap closed after 28 taps and a sample of the paste was collected, weighed using a small container, and dried in an oven at 110°C overnight. Three empty containers were weighed and recorded to measure the weight of the sample without the weight of the can. Two similar procedures were repeated at varying moisture contents.

After the first procedure is completed, a few drops of water were added to the paste to increase moisture content. In the second procedure, the gap in the paste was closed at 23 taps and at 18 taps in the third procedure. A sample was also collected from all varying moisture content for weighing. The samples were dried in an oven overnight at 110°C. The moisture content  $MC$  (%) at each tap was calculated as follows:

$$MC = \frac{\text{Mass of moisture}}{\text{Mass of dry soil}} \times 100\% \quad (3.1)$$

The number of taps ( $N$ ) was plotted against the water content. A straight line was constructed for which the liquid limit ( $LL$ ) was determined as the water content corresponding to 25 taps. In plotting the liquid limit data, some data recorded from the tests did not form a straight line probably due to the small volumes of tailings in the cans, or inadequate height of fall. It is for this reason that Equation (3.2) was used to compensate for these inaccuracies (South African National Standard: SANS, 2011)

$$LL = MC \left( \frac{N}{25} \right)^{0.121} \quad (3.2)$$

Where  $N$  denotes the number of taps

This brings us to discuss the steps taken to carry out the plastic limit procedure. The plastic limit ( $PL$ ) is the water content at which the paste changes from a plastic state to a semisolid state. Three ellipsoidal-shaped portions of the paste were rolled repeatedly on a glass surface by hand. This was done until the thread of the paste started to crumble (see Figure 3.5), the diameter of the thread was not greater than 3 mm when it started to crumble. The crumbs were combined and kneaded again into ellipsoidal masses and were rolled again. The paste was rolled until it crumbled and could no longer be rolled into a 3 mm diameter thread. The same paste was then put in two containers (the empty weight of the containers was recorded) and dried in an oven overnight at 110°C. All the dried samples were weighed and recorded; the results were used to determine the plasticity index.



Figure 3.5 Rolling of ellipsoidal paste for determining plastic index.

The plastic index ( $PI$ ) was calculated as follows (SANS, 2011):

$$PI = LL - PL \quad (3.3)$$

Where  $LL$  is the liquid limit and  $PL$  represents the plastic limit. The moisture content was deemed to represent the plastic limit of the paste. The interpretation of the value from Equation (3.3) can be done in line with the description in Section 2.3 and Figure 2.2.

### 3.3.3 X-Ray fluorescence spectrometer

The mineral composition of the tailings was determined using the handheld X-Ray fluorescence device at the mining engineering laboratory of the University of South Africa. The elemental analysis was carried out by placing the front window of the device in contact with the sample. In order to detect the elements, the analysis was done by pressing the trigger finger button which releases x-rays into the sample. The X-rays characteristics are released from the sample and the detector quantifies the elements in the sample. The results of this analysis are presented in Chapter 4.

### 3.3.4 Slump tests

A slump test was conducted according to ASTM C143 standards to determine the consistency and viscosity of the CTB. Slurry liquidity is an important feature of

backfilling transportation. The higher the slump, the better the slurry liquidity is (Zhou et al., 2017).

As shown in Figure 3.6a, the apparatus used for the slump test is a frustum mould known as the slump cone (length: 30 cm, diameter: 20 cm, top opening: 20 cm), together with a base plate, a steel tamping rod and a measuring tape.

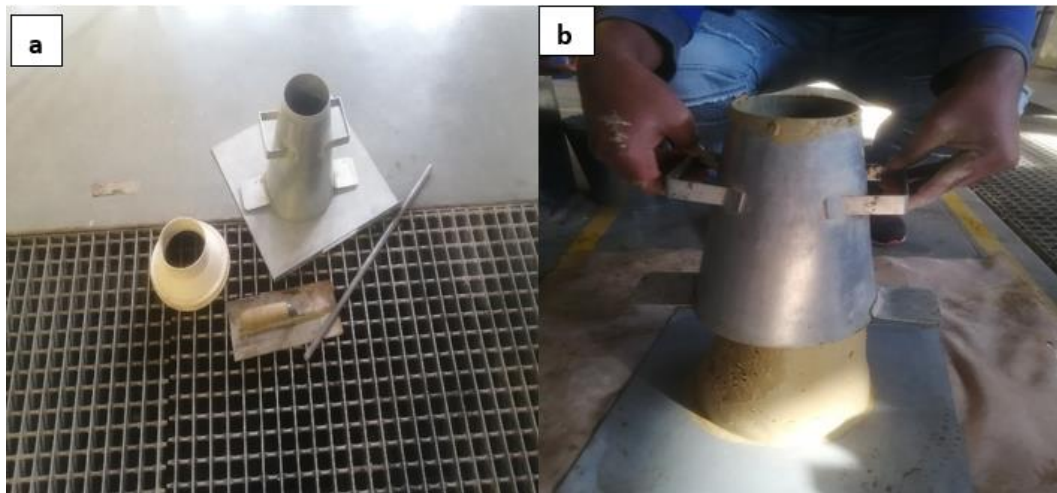


Figure 3.6 (a) Equipment required for a slump test procedure; (b) Performing a slump test.

The internal surface of the slump cone was cleaned and placed on the base plate. The cone was filled with CTB in three layers. The first layer (1/3) was tamped 25 times using a steel tamping rod uniformly over the entire cross-section of the sample. A second layer (2/3) was poured and circularly tamped 25 times, as done in the previous layer. Once the slump was full, tamping was also done 25 times, even penetrating slightly the second layer. The excess CTB material was scraped off and the opening was levelled. The cone was lifted gently (see Figure 3.6b) in a vertical direction and the unsupported material was left to slump. The slump cone was inverted, and the tamping rod was placed across the slump cone base with one end suspended over the pile of the backfill. A measuring tape was used to measure the distance from the edge of the top surface of the backfill to the bottom of the tamping rod. The decrease in height of the material is known as the slump. The same procedure was applied for all different mixing proportions, the water content remained constant.

### 3.3.5 *Mixing and curing procedure*

An Ordinary Portland Cement (CEM V 42.5 N) was used as the hydraulic binding agent. The acronym CEM represents the term cement while V refers to the constituents of the cement. A cement type CEM V contains a high percentage of blast furnace slag and fly ash, up to a maximum content of 38%. This particular cement is highly used to resist sulphate attack. The 42.5 N refers to the grade (strength) of the cement and the rate of strength gain; the cement is of strength 42.5 MPa with normal (N) strength gain. The addition of 20% of fly ash to cement results in reduced water consumption (Szczesniak et al., 2020) and the use of slag aids in the reduction of carbon dioxide emissions (Saleh and Eskander, 2020).

The CTB specimens were prepared according to the ASTM C 192 standards. The backfill samples were made with a cement/tailing (c/t) ratio of 2.5 which makes up a solid concentration of 73% and a water content of 27%. The ingredients were mixed using a concrete mixer as shown in Figure 3.7a, for at least 10 min (as recommended by Qi et al. (2018) to obtain a homogenous slurry. The cement content in the above mixture is 20%; therefore, the cement content was increased by 10% in other proportions to observe the change in the strength of CTB.

The control mixture (non-layered) was placed in 150 mm cubic moulds (see Figure 3.7b) in 3 layers of equal volume. After the first layer was placed, a rod was used to strike the mixture 25 times uniformly over the cross-section of the mould. Another layer was poured and rodded 25 times, the mould was tapped 15 times to close the holes of the rod. The same procedure was followed with the last layer and the mould was vibrated until the top surface of the CTB mixture became smooth. The backfill specimens were then cured for 24 h at 25°C. After 24 h of curing, the specimens were removed from the moulds and coded as per the curing period, i.e., for 7 days, 14 days, 21 days, and 28 days respectively (adapted from Nasir and Fall, 2010). The specimens were then immersed in water in a water storage tank to be cured as per the specified curing days. The above-mentioned procedure was used for single-layered specimens.

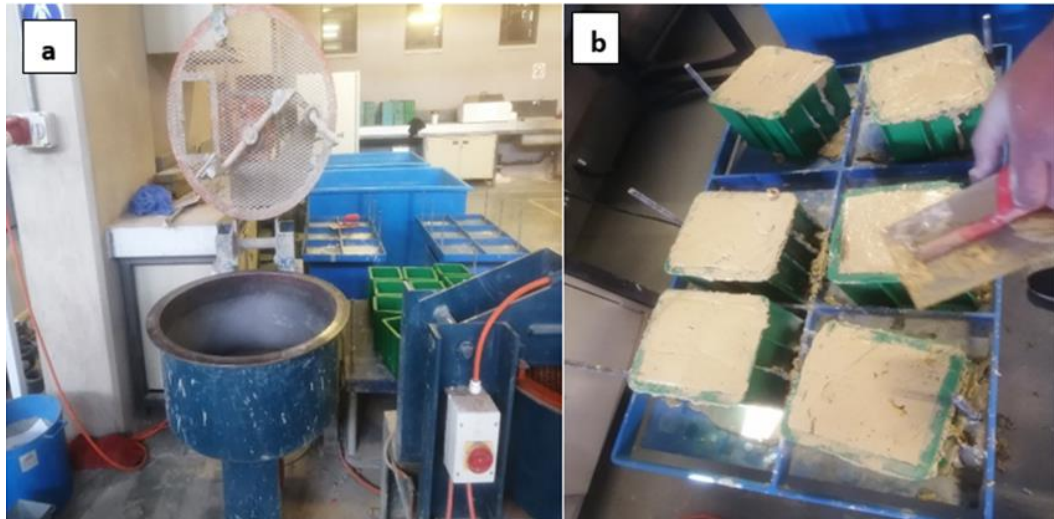


Figure 3.7 (a) A concrete mixer used to mix CTB slurry; (b) Casting CTB slurry into a cubic mould.

To establish the layering of the specimens, the first layer was poured into the mould, vibrated, and allowed to cure for 24 h before placing the last year. When all the moulds were full, the specimens were cured for 24 h, demoulded and coded as per the experiment design. For example, 20% cement content, two layers (2L) and 7 days of curing was coded as 20%;2L;7d. The filling height of the two-layered and three-layered CTB specimens was 75 mm and 50 mm at each time, respectively. Similarly, the samples were also coded accordingly, i.e., 20%;3L;7d. Three specimens of each curing day were made for validation purposes (Wang et al., 2021). Table 3.1 shows the reproducibility of the experiment and the total number of specimens made.

Table 3.1 Number of CTB specimens made per mixture design.

20% cement content	Curing periods			
	7 days	14 days	21 days	28 days
Single layer	3 samples	3 samples	3 samples	3 samples
Two layers	3 samples	3 samples	3 samples	3 samples
Three layers	3 samples	3 samples	3 samples	3 samples
The total number of specimens is 36 for a 20% mixture design. Therefore, an overall total of <b>108</b> specimens were prepared in this study.				

### 3.3.6 Mechanical compression tests

The UCS of the CTB samples was tested using a universal testing machine following ASTM C39 standards. The upper and lower surfaces of the CTB were levelled and subjected to a UCS test. The specimen was placed and aligned with the centre of thrust of the spherically seated bearing block. The load indicator was set at zero before commencing the tests. A loading rate of 0.5 mm per minute was applied to the specimens until failure occurred. The deformation was measured by a calliper and recorded to measure the strain. The compressive strength of the specimen was calculated by dividing the maximum load achieved during the test by the cross-sectional area of the specimen. Three replicates of each UCS test were done and their mean value was calculated, the results are presented later in Chapter 4. The process followed starting from mixing to testing is illustrated in Figure 3.8 below. Summarily, once the tailings were mixed with water and cement to form a CTB slurry, this was moulded in cubes and cured before the universal mechanical press was used to test the load-bearing capacity of the CTB.

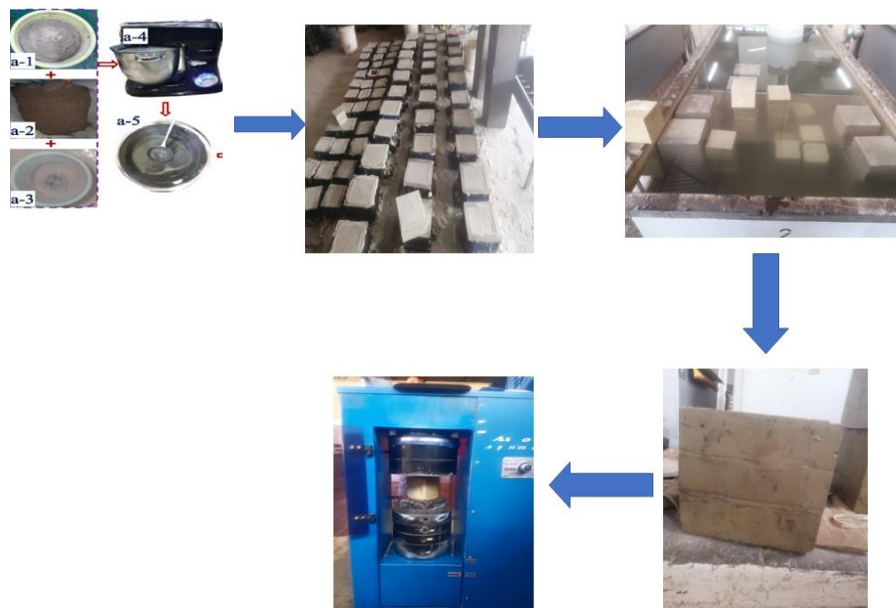


Figure 3.8 Step by step procedure from mixing the backfill to testing compressive strength.

The results obtained from the UCS tests were used to calculate the stress ( $\sigma$ ), strain ( $\epsilon$ ) and elastic modulus ( $E$ ) of CTB material using Equations 3.4 to 3.7:

$$\epsilon = \frac{\Delta l}{L_0} \quad (3.4)$$

where  $\varepsilon$  is the strain,  $\Delta l$  is the change in the measured length of the specimen, and  $L_0$  denotes the original length of the specimen.

$$\sigma = \frac{P}{A_0} \quad (3.5)$$

where  $\sigma$  is the compressive stress,  $P$  is the load, and  $A_0$  is the cross-sectional area of the specimen. Therefore, the uniaxial compressive strength (*UCS*) was calculated for the maximum load applied:

$$UCS = \frac{P_{max}}{A_0} \quad (3.6)$$

Lastly, the elastic modulus ( $E$ ) was calculated:

$$E = \frac{\sigma}{\varepsilon} \quad (3.7)$$

### 3.4 Development of simulation model

OPTUM G3 is a finite element method commercial software with a possibility of a one-month trial, thereafter, a monthly subscription is required to continue the use of the software. Nonetheless, the software also offers a free academic version for some institutions. The computer system requirements of the software to operate optimally are as summarised in Table 3.2.

Table 3.2 System requirements of OPTUM G3

<b>Parameter</b>	<b>Description</b>
<b>Operating System</b>	<ul style="list-style-type: none"> <li>• Microsoft® Windows® 7 SP1 with Update KB4019990 (64-bit)</li> <li>• Microsoft Windows 8.1 (64-bit)</li> <li>• Microsoft Windows 10 (64-bit)</li> </ul>
<b>CPU Type</b>	64-bit Intel Multicore processor or AMD Athlon 64 processor
<b>Memory</b>	Required: 4GB Recommended: 8 GB
<b>Display</b>	Basic: 1024 x 768 pixels, 32-bit colour palette
<b>Resolution</b>	Recommended: 1920 x 1080 pixels, 32-bit colour palette
<b>Disk Space</b>	6 GB
<b>.NET Framework</b>	.NET Framework Version 4.5.2

In terms of the development of the FEM-based simulation model, the sub-sections below provide a succinct breakdown of the procedure followed. And later, Chapter 6 expands on the numerical model itself and the significance of the simulation outputs.

### 3.4.1 Meshing

The numerical analysis exercise simulated an underground rock block with an open stope located 1000 m deep. The open stope is first analysed to measure the principal stress acting on it and later backfilled through various steps to study the fluctuations of the stress with every backfilling step. The simulation work is essential to validate the laboratory work conducted. When the simulation results reveal any variation of the stress distribution within the stope under different layers of backfill, the objectives of this PhD thesis would be successfully met.

A block of 75 by 100 m was developed to simulate the rock mass located underground. The block was then discretized into 1 000 elements. The simulation processing time was very short and so was the principal stress also very low. Thereafter, the mesh size was refined to 10 000 elements (see Figure 3.9) with the consideration that a mesh size that is too coarse may generate inaccurate results (Newman, 2018). Conversely, a too-dense mesh may increase the calculation period and cause a difficult stress convergence (Qi et al., 2022). Once the mesh has been refined, the results of the simulations changed by 150%.

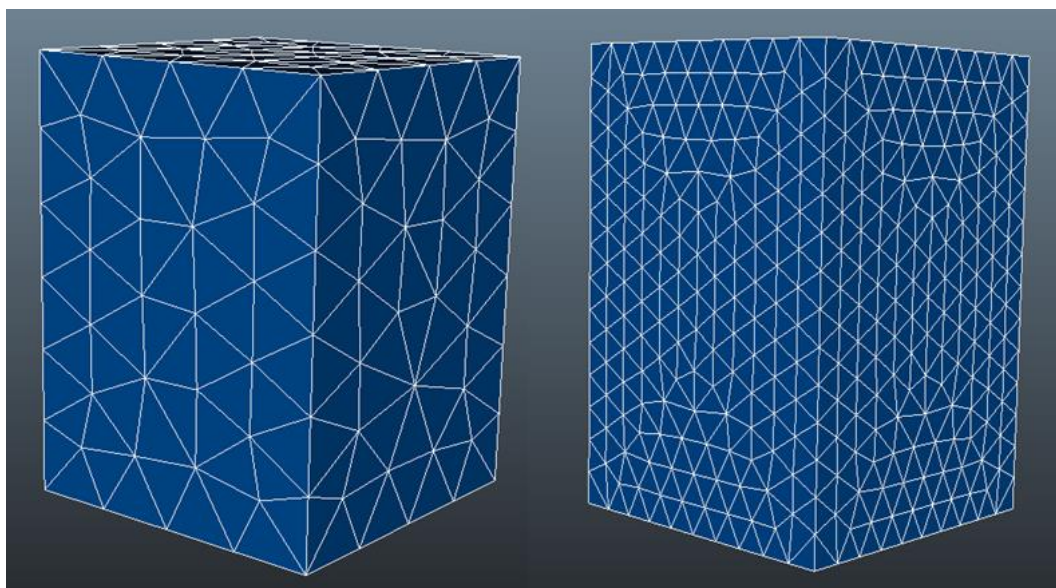


Figure 3.9 Mesh refinement



### 3.4.2 Properties of the rock mass and backfill material

A block size of 30 × 25 × 20 m was excavated in the rock mass to simulate a 20 m open stope. The schematic view of the model is shown in Figure 3.10. The properties of the rock mass and backfill are adapted from literature and are shown in the Tables 3.3 and 3.4. The rock mass is assumed to be homogeneous, and isotropic and obeys the Mohr-Coulomb (MC) properties. The results from Atterberg's tests indicated that the tailings are clayey. Therefore, the backfill material was also assumed to be stiff clay and obeys elastic-plastic behaviour (Cui and Fall, 2016).

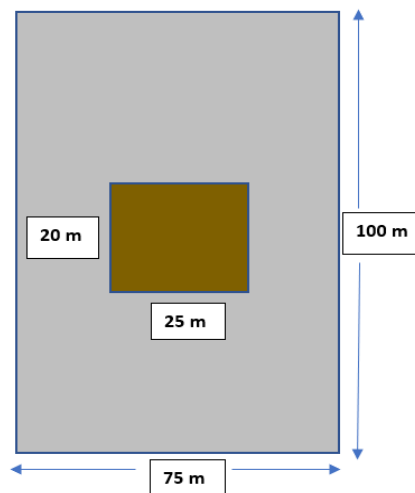


Figure 3.10 Schematic view of the backfilled stope

The input material properties used for the model is adapted from Guo et al. (2022), Qi et al. (2022), and Zhao et al. (2021) as shown in Tables 3.3 and 3.4. Note that most input parameters were extracted from the data collected in this chapter and the results presented in Chapter 4. However, additional mechanical parameters such as cohesion, Poisson ratio and angle of friction were sourced from previous studies available in the literature.

Table 3.3 Properties of the rock mass used in the numerical modelling (Guo et al., 2022; Qi et al., 2022; Zhao et al., 2021)

<b>Bulk density</b>	<b>2 700 kg/m<sup>3</sup></b>
<b>Cohesion (c)</b>	5.5 MPa
<b>Shear modulus (G)</b>	12 200 MPa
<b>Bulk modulus (K)</b>	26 400 MPa

<b>Young's modulus (<math>E</math>)</b>	0.66 MPa
<b>Unit weight (<math>\gamma</math>)</b>	28 kN/m <sup>3</sup>
<b>Friction angle (<math>\phi</math>)</b>	57°
<b>Poisson ratio (<math>\nu</math>)</b>	0.3

Table 3.4 Properties of the backfill material used in the numerical modelling (Guo et al., 2022; Qi et al., 2022; Zhao et al., 2021)

<b>Bulk density</b>	<b>2 700 kg/m<sup>3</sup></b>
<b>Cohesion (<math>c</math>)</b>	20 MPa
<b>Shear modulus (<math>G</math>)</b>	62.5 MPa
<b>Bulk modulus (<math>K</math>)</b>	83 300 MPa
<b>Young's modulus (<math>E</math>)</b>	150 MPa
<b>Unit weight (<math>\gamma</math>)</b>	20 kN/m <sup>3</sup>
<b>Friction angle (<math>\phi</math>)</b>	30°
<b>Poisson ratio (<math>\nu</math>)</b>	0.3

### 3.4.3 Initial stresses around the stope

For the initial stresses, the overburden weight of 1000 m and the ground pressure coefficient ( $K_0$ ) of 0.5. The initial stress calculated using Equation (3.8) was found to be 26.5 MPa.

$$\sigma_v = \rho h g \quad (3.8)$$

Wherein  $\rho$  denotes the density of material (kg/m<sup>3</sup>),  $h$  is the mining depth (m) and  $g$  is the gravity acceleration at 9.81 m/s<sup>2</sup>.

### 3.4.4 Backfilling process

The 20 m stope was backfilled using different strategies, i.e., an immediate single pour, two layers of backfill and consecutively to four layers of backfill. It is assumed that the stope is backfilled from the top, thus, a tight fill is achieved. Therefore, no gap is left at the top of the stope. The simulation of each filling strategy is run from the excavation stage until backfilling is complete. After the excavation, the backfilling process is simulated as the material is placed in layers until the stope has been backfilled. Figure 3.11 illustrates the modelling procedure followed, from

creating a block (rock mass), followed by the excavation and the backfilling process.

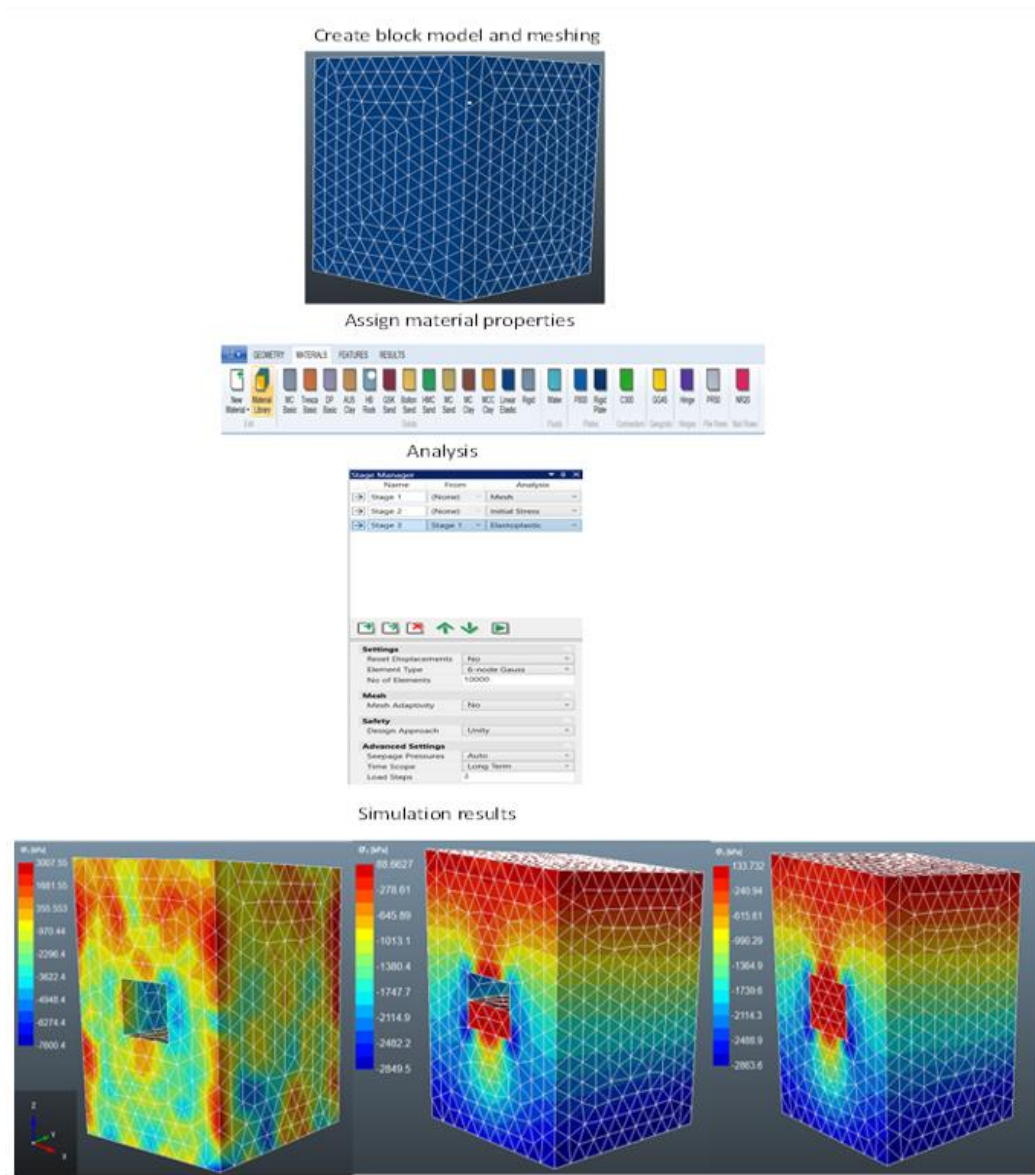


Figure 3.9 Illustration of the backfill modelling process.

The shape and dimensions of the slope were kept constant throughout the simulation process to limit the impact of external factors on the strength of the backfill as these are not part of the scope.

### 3.5 Challenges encountered with the experimental tests.

The first mixture of CTB prepared was very stiff as shown in Figure 3.12. When the slump test was performed, the measured slump was very low at 75 mm, which is

less than the minimum 150 mm recommended by Wu et al. (2015). Initially, a cement/tailing ratio of 1:4 was used adapted from Wang et al. (2021). However, due to the material differences, the mixture did not work on the tailings used in this study. As a result, the mixture was sticky and stiff. This challenge was overcome by doing a trial run of the mixture design until we selected one with a slump value of 180 mm. In support of the trial-and-error method, Yilmaz et al. (2015) add that there is no standard backfill recipe and specimen size for the determination of the UCS of CPB materials. Additionally, shaking the stack of sieves by hand may present some errors as compared to using a mechanical shaker. Indeed, shaking the sieves by hand is a tedious process, this may result in some material that was meant to pass through a certain sieve being retained.



Figure 3.12 The failed slump test due to a stiff mixture

Last note, this chapter outlined and discussed the empirical method followed to collect the raw data for the study. The next chapter presents the findings obtained from the laboratory tests while Chapters 5 and 6 cover the empirical and analytical analysis of the stability of backfill respectively.

## Chapter 4 Effects of cement-to-tailings ratio and layering on the compressive strength of cemented tailings backfill.

### 4.1 Introduction

In Chapter 2, it was discussed how the properties of tailings (particle size, mineral composition, plasticity) affect the performance of CTB. A high percentage of fines in tailings is known to improve the strength of CTB. Indeed, the fine particles fill the pores between the coarse particles, reducing the porosity of the CTB structure. As a result, the strength of CTB increases (Cheng et al., 2020; Ke et al., 2015; Wu et al., 2018). Although the fines improve the mechanical performance of CTB, it affects the flowability of CTB. This is crucial for transporting CTB in underground stopes without clogging the pipes. Fines have been reported to absorb excess of water; thus, more water may be needed to maintain the consistency and viscosity of CTB (Fall et al., 2005; Qiu et al., 2020; Wang et al., 2021). This was observed at the lab when performing a slump test. The sample had a high content of fines, as a result, the fines absorbed more water and the mixture sticky. Consequently, the viscosity of the slurry was very low.

The chemical composition of tailings is also known to affect the performance of CTB. For example, high sulphide tailings diminish the strength of CTB by forming and expanding cracks into the CTB structure. On the other hand, some compounds found in tailings, e.g., Silicon dioxide and Calcium oxide are reported to improve the filling stability and carrying capacity of CTB, respectively (Kasap et al., 2022; Wang et al., 2017). Moreover, UCS is widely used to determine the strength of CTB due to its reliability, simplicity, and affordability. It is the above information that governs the methods used to collect data for this study.

This chapter presents and discusses the results obtained in UNISA and Civilab laboratories from various tests conducted. It commences by discussing the results obtained from the sieving analysis. The tailings sample is classified and graded based on its size distribution. Afterwards, Atterberg's limits are calculated for categorisation as solid, plastic, non-plastic clayey or silty. The chemical composition of the tailings follows. Lastly, all the above are linked to the corresponding mechanical properties of the CTB (i.e., UCS and elastic modulus).

## 4.2 Particle size distribution of the tailings material collected

This section presents the data collected when conducting sieving analysis. Key characteristics of the material are also extracted from the gradation curve.

Starting off with the sieving results, Table 4.1 shows the mass of particles retained in each specified sieve size. The information in the table was used to draw the graph in Figure 4.1. This graph shows that the fractions of particles passing through different sieves range from 10% to 100% while particles in the tailings material are of size less than 50 mm.

Table 4.1 Mass fractions of tailings particles retained in different sieves.

Sieve size [mm]	Mass of material retained [g]	Mass retained [%]	Cumulative mass passing [%]
50	0	0	100
28	312.3	11.5	89
20	304.3	11.2	78
14	214.9	7.9	70
5	715.4	26.4	44
2	446.2	16.5	28
0.425	460.2	17.0	11
Pan	253.0	9.3	
Total	2707.9		

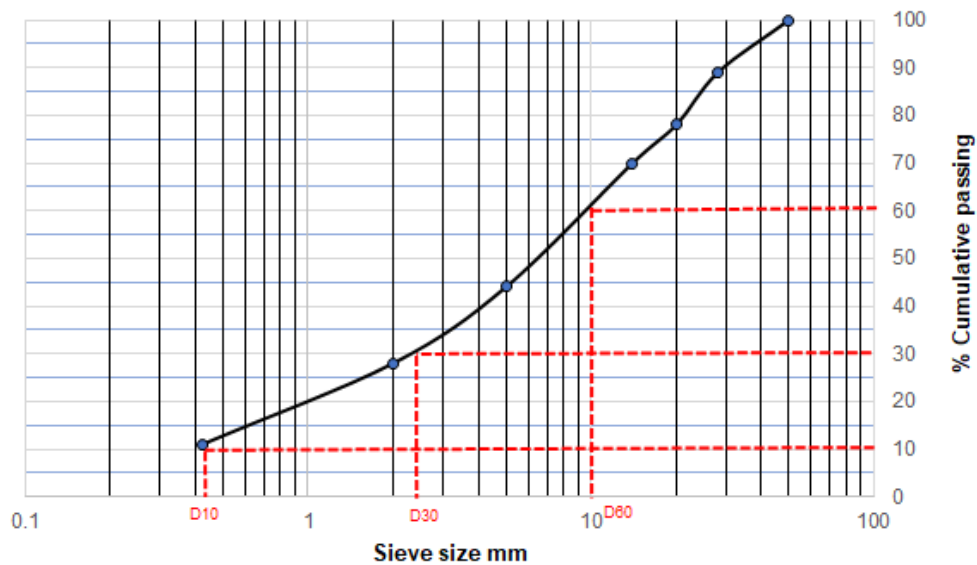


Figure 4.1 Gradation curve of the collected tailing sample.

From Figure 4.1, it can be seen that  $D_{60}$ ,  $D_{30}$ , and  $D_{10}$  are 10 mm, 2.2 mm, and 0.3 mm respectively. So, by substituting these values read off Figure 4.1 into Equations (2.2) and (2.3), the following were obtained  $C_u = 33.3$  and  $C_c = 1.61$ . These values indicated that the tailings material collected is well-graded. The  $C_u$  of the tailings was found to be greatly higher than 5, signifying a great imbalance between coarse and fine tailings (Peng et al., 2021). However, the balance was created during the mixing of the tailings with water and cement. The concrete mixture equipment is robust, and the tailings were ground to fine material during mixing. Thus, the backfill slurry had no coarse tailings but fines. Furthermore, the  $C_c$  of the tailings was found to be between 1 and 3. Therefore, indicating well-graded tailings (Dalce et al., 2019; Zhou et al., 2019).

### 4.3 Atterberg's attributes of the tailings material

At varied degrees of moisture content, the behaviour of soils is different due to unique engineering properties. It is therefore important to determine the properties of the tailings. This section presents the results for the liquid limit  $LL$ , plastic limit  $PL$ , and plasticity index  $PI$  of the tailings.

The results recorded from the Atterberg limit procedure are shown in Table 4.2. The results from Table 4.2 were further used to produce Figure 4.2 to determine the moisture content of the tailings at 25 taps. The moisture content corresponding to 25 taps is the liquid limit of the tailings.

Table 4.2 Data recorded from Atterberg's tests.

	Test 1	Test 2	Test 3
<b>Container label</b>	A	B	C
<b>Mass of container and wet soil [g]</b>	31.9	32.5	31.5
<b>Mass of container and dry soil [g]</b>	30.8	31.8	30.9
<b>Mass of container only [g]</b>	28.2	28.5	28.4
<b>Mass of moisture [g]</b>	1.1	0.7	0.6
<b>Mass of dry soil [g]</b>	2.6	3.3	2.5
<b>Moisture content [%]</b>	42.31	21.21	24
<b>Number of taps</b>	28	23	18

When using Figure 4.2, it has been found that the liquid limit of the tailings is 26%. As it can be seen, the graph did not form a straight line as it should. This is attributed to the small quantities of tailings in the cans since a small portion of the mixture was randomly taken from the mixture. Therefore, to account for any inaccuracies, Equation (3.2) was used to calculate the liquid limit and was found to be liquid limit 27%.

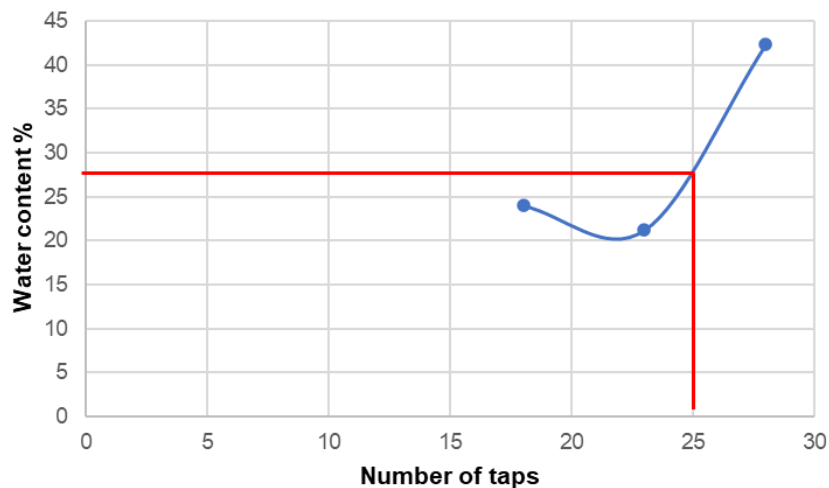


Figure 4.2 Liquid limit (moisture content) corresponding to 25 taps.

Table 4.3 presents the findings from the plastic limit tests, i.e., a test to determine the moisture content at which the tailings change from plastic state to semisolid state. The plastic limit is required to determine the plasticity index, which is an important value when classifying tailings. The moisture content of both samples



i.e., test 1 and 2, was determined using Equation 3.1. The average moisture content (plastic limit) from both tests is 15.11%.

Table 4.3 Data recorded from the liquid limit tests.

	Test 1	Test 2
<b>Container label</b>	D	E
<b>Mass of container and wet soil [g]</b>	42.8	43.5
<b>Mass of container and dry soil [g]</b>	42.7	43.2
<b>Mass of container only [g]</b>	41.3	41.9
<b>Mass of moisture [g]</b>	0.1	0.3
<b>Mass of dry soil [g]</b>	1.4	1.3
<b>Moisture content [%]</b>	7.14%	23.08%

The liquid limit and plastic limit values were substituted into Equation (3.3) to calculate the plasticity index. The plasticity index was found to be 11.89%. According to Figure 4.3, the tailings can be classified as a low-plasticity clay material. Indeed, the tailings were sticky and clayey as observed in the laboratory (see Figure 3.12).

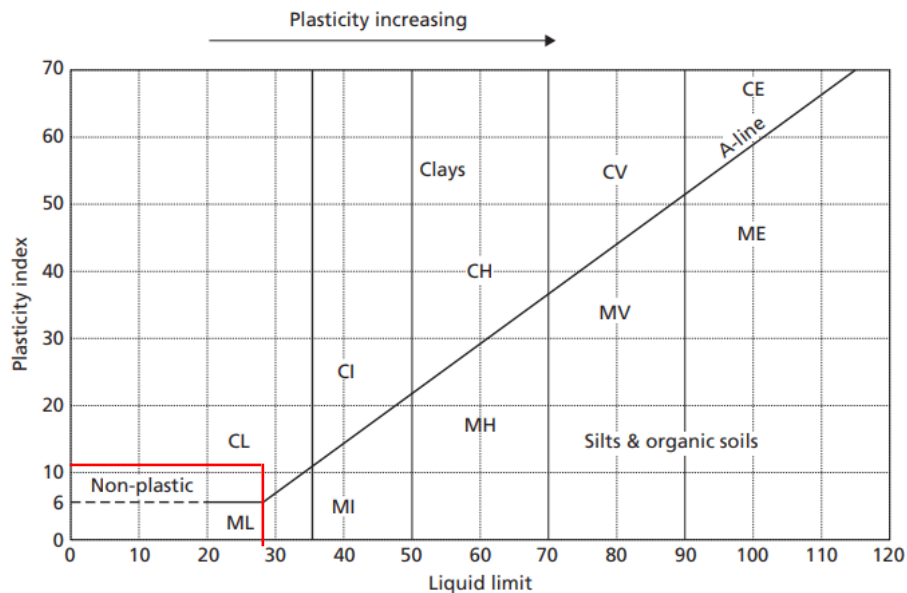


Figure 4.3 Plasticity index chart to classify tailings type.

These Atterberg's tests results are further used in the plasticity index chart to determine the category of soil which the tailings fall under. Therefore, it has been determined from the chart that the tailings are of low plastic clay material. This is

information is also significant when defining the properties of the tailings during simulations. Islam (2021) conducted the same tests to study the mechanical behaviour of three different types of tailings, namely, coal tailings, gold tailings and red mud. He also found that the gold tailings were of the lowest plasticity compared to the other tailings. Islam (2021) further adds that most of the mine tailings contain significant percentages of clay minerals. The next section presents the XRF analysis, and compression tests. The results extracted from the UCS tests include the elastic modulus of CTB for different layers.

#### 4.4 Mineral composition of the tailings material

The mineral content of the tailings material used in this doctoral study is presented in Table 4.4. This was obtained by XRF analysis following the protocol presented in Section 3.3.3.

Table 4.4 Mineral composition of the tailings material by XRF analysis

<b>Component</b>	<b>Mass fraction [%]</b>
<b>MnO</b>	0.024%
<b>Fe<sub>2</sub>O<sub>3</sub></b>	3.8%
<b>FeS<sub>2</sub></b>	64.4%
<b>Ni</b>	2.4%
<b>Zr</b>	2.6%
<b>Ru</b>	3.4%
<b>Rh</b>	12.8%
<b>In</b>	9.5%
<b>Zn</b>	0.02%
<b>Cu</b>	0.02%

The tailings used in this work are very high in sulphide minerals. Sulphide minerals are known to affect the strength of CTB through a process known as the sulphate attack. Wang et al. (2020a) investigated the effect of sulphate attack on the compressive strength of backfill. In this case, they found that the chemical reaction between sulphate and hydration products at the initial stage had a positive effect on the UCS of backfill due to the refinement of the pores. However, a continuous reaction results in excess gypsum in the pore space that damages the

microstructure and degrades the fill material. The effect of sulphate attack on the strength of CTB in this study was overcome by using CEM V Portland cement rich in furnace slag and fly ash. The cement was particularly manufactured to resist sulphate attack and other harsh conditions.

#### 4.5 Results of the slump tests

Three mixture designs were adopted in this study, i.e., cement/tailing (c/t) ratio of 2.5, 2.3 and 2.1 respectively. And for each mixture, the water/cement ratio was adopted as such: 1.3, 1.32, and 1.21. A slump test was conducted to measure the consistency and flowability of CTB slurry. The results of the slump tests are shown in Table 4.5.

Table 4.5 Slump test results

<b>Mixture proportion</b>	<b>Slump</b>
<b>2.5 c/t ratio</b>	185 mm
<b>2.3 c/t ratio</b>	180 mm
<b>2.1 c/t ratio</b>	160 mm

As indicated in Chapter 2, a slump of CTB of between 152 and 254 mm is acceptable (Belem et al., 2016; Ouattara et al., 2018). A slump not only measures the flowability of CTB but, also affects its strength. That is, a high slump value diminishes the final strength of CTB whilst increasing the pumping ability of the fill. On the other hand, a low slump value results in high strength of CTB but with difficult transportation of the fill (Niroshan et al., 2018). In this study, the slump value of the slurry decreased with an increase in cement. However, the slump for every mixture is still within the recommended slump, i.e., 185 mm, 180 mm and 160 mm. Thus, the transportability of the mixture was not compromised.

#### 4.6 Mechanical properties of the CTB samples

This section presents the results of the laboratory compression tests performed on CTB cubes (see Section 3.3.6 for reference). The findings are presented in different themes, i.e., looking at the effects of curing time, binder content and layering on the mechanical performance of CTB samples.

#### 4.6.1 Effect of curing time on the compressive strength and elastic modulus of CTB samples

Table 4.6 shows the average UCS results of the combination of the mix ratio at various curing periods, from 7-28 days. For each layer, 3 samples were cured for validity purposes and the average UCS was calculated. The UCS of the samples develops with the curing period regardless of the binder dosage or type. The results of the study have shown that the UCS of the 2.5 c/t mix ratio was rapidly increasing from 5.2 MPa at 7 days to 9.2 MPa at 28 days, which is a 76.9% increase. Whereas an increase of 69.8% is observed for the 2.3 c/t ratios from 7 days to 28 days. These findings corroborate the findings of Fall et al. (2008) and Yilmaz et al. (2014). The authors studied the mechanical behaviour of CTB under different conditions. However, the same trend of the effect of the curing period on the UCS of CTB samples was observed. The strength development is high at an early age (7 – 14 days) as compared to long-term strength development (21 – 28 days). The strength gain is due to increased cement hydration products such as C-S-H gels, which are known to reduce porosity and improve the cohesion of CTB (Jiang et al., 2020c). The significant increase in strength in the early days is corroborated by Xu et al. (2022) who attributed it to the high rate of cement hydration taking place at an early age. The increase rate for two-layered samples from 7 to 14 days and 14 to 28 days is 24.64%, and 11.2%. In this case, a high increase rate of UCS at an early age is observed, then, a slight increase at a later stage. The standard deviation (STDV) also indicates that the UCS does not deviate too far from the average.

Table 4.6 Uniaxial compressive strength [in MPa] of CTB samples for different combinations of cement-to-tailings ratios, curing periods, and layering structures.

		Curing periods			
		c/t mix ratio	7 days	14 days	21 days
1 layer	<b>2.1</b>	6.313	10.000	12.000	15.700
	<b>STDV</b>	0.250	0.681	0.342	0.210
	<b>2.3</b>	6.313	8.760	10.113	10.699
	<b>STDV</b>	0.258	0.889	0.340	0.190
	<b>2.5</b>	5.240	7.600	8.535	9.193
	<b>STDV</b>	0.248	0.332	0.435	0.232

<b>2 layers</b>	<b>2.1</b>	6.100	9.800	11.600	12.800
	<b>STDV</b>	0.310	0.420	0.360	0.120
	<b>2.3</b>	5.110	7.100	7.800	7.778
	<b>STDV</b>	0.214	0.132	0.418	0.212
	<b>2.5</b>	4.680	6.210	7.553	7.635
	<b>STDV</b>	0.374	0.547	0.300	0.188
<b>3 layers</b>	<b>2.1</b>	6.900	9.800	12.400	13.700
	<b>STDV</b>	0.351	0.400	0.280	0.130
	<b>2.3</b>	4.713	7.160	7.400	9.0
	<b>STDV</b>	0.444	0.341	0.284	0.132
	<b>2.5</b>	4.470	6.460	7.266	8.616
	<b>STDV</b>	0.207	0.543	0.496	0.127

In Table 4.7, the elastic modulus for the 2.1 c/t ratio is not recorded. This is because the equipment used to measure the strain was dysfunctional. Therefore, the strain measurements were not done for the 7 and 14 days, thus, it was decided to continue as such. The elastic modulus was calculated from the data using Equation (3.7). In a similar increasing pattern of the compressive strength of CTB samples, the elastic modulus of the samples also increases with time.

Table 4.7 Elastic modulus [in MPa] of CTB samples for different combinations of cement-to-tailings ratios, curing periods, and layering structures.

		<b>Curing periods</b>				
		<b>c/t mix ratio</b>	<b>7 days</b>	<b>14 days</b>	<b>21 days</b>	<b>28 days</b>
<b>1 layer</b>	<b>2.1</b>					
	<b>2.3</b>		315.670	867.000	1011.333	5319.411
	<b>2.5</b>		392.750	451.400	853.500	4596.667
<b>2 layers</b>	<b>2.1</b>					
	<b>2.3</b>		139.110	350.352	257.400	388.500
	<b>2.5</b>		175.626	205.511	251.778	381.750
<b>3 layers</b>	<b>2.1</b>					
	<b>2.3</b>		212.100	357.366	363.333	1343.333
	<b>2.5</b>		200.749	320.963	277.500	861.630

As shown in Table 4.7, the elastic modulus of the samples increases with time. Thus, the CTB samples become stiffer with time. The changes in elastic modulus from 7 days to 14 days until 28 days are 2.31%, 48.86% and 81.43%, respectively. With slower growth rates from 14 days to 28 days, the elastic modulus of the two-layered and three-layered samples is 34.05% and 57.83%, respectively. Elastic modulus is known to be one of the crucial indicators to measure the elastic deformation of CTB. A high elastic modulus indicates that a high-stress value is required for the deformation of that specific sample to occur. That is, the higher the elastic modulus, the stiffer the sample (Xue et al., 2020; Zhang et al., 2022). Indeed, the findings attest that the samples become stiffer with time due to denser pore structures (Liu and Fall, 2022). Similarly, Libos and Cui (2020) confirm that CTB stiffness gradually develops with curing time.

#### *4.6.2 Effect of binder content on the performance of CTB samples*

The effect of cement content is shown in Figure 4.4 throughout the curing period. The findings show that the UCS of the 2.5 c/t mix ratio is 9.1 MPa, 7.6 MPa, and 8.6 MPa for the non-layered, two-layered, and three-layered samples, respectively. Likewise, the UCS values for the 2.3 c/t samples is 10.7 MPa, 7.8 MPa, and 9.0 MPa taken also in the same order of layering. Similarly, the non-layered, two-layered and three-layered 2.1 c/t samples possessed greater UCS as follows: 15.7 MPa, 12.8 MPa, and 13.7 MPa. The elastic modulus of the 2.5 c/t mix ratio for the non-layered sample, two-layered sample and three-layered sample is 4596.7 MPa, 381.8 MPa, and 861.6 MPa respectively. Similarly, when looking at the 2.3 c/t mix ratio, the elastic modulus of the non-layered, two-layered and three-layered samples is 5319.4 MPa, 388.5 MPa, and 1343.3 MPa, respectively. The effect of cement here is visible, and the strength of samples increases when more cement is added. Libos and Cui (2020) witnessed the same findings in their experimental study of the fracture toughness of CTB. An increase in cement leads to a generation of more hydration products which forms a more cohesive CTB matrix (Zhang and Li, 2021). Consequently, the water within the pores is consumed and the samples solidify. The heat from hydration speeds up hydration, and precipitation of calcium hydroxide (CH) and calcium silicate hydrate (C–S–H), which is what gives CTB its strength (Zhou et al., 2019). Raut et al. (2022) concur that excess cement generates more hydration gel that further anchors the CTB

effectively. Likewise, the elastic modulus also increases with an increase in cement content. The same findings were reported Wang et al. (2020b). Thus, it can be deduced that the higher the cement, the stiffer the CTB samples.

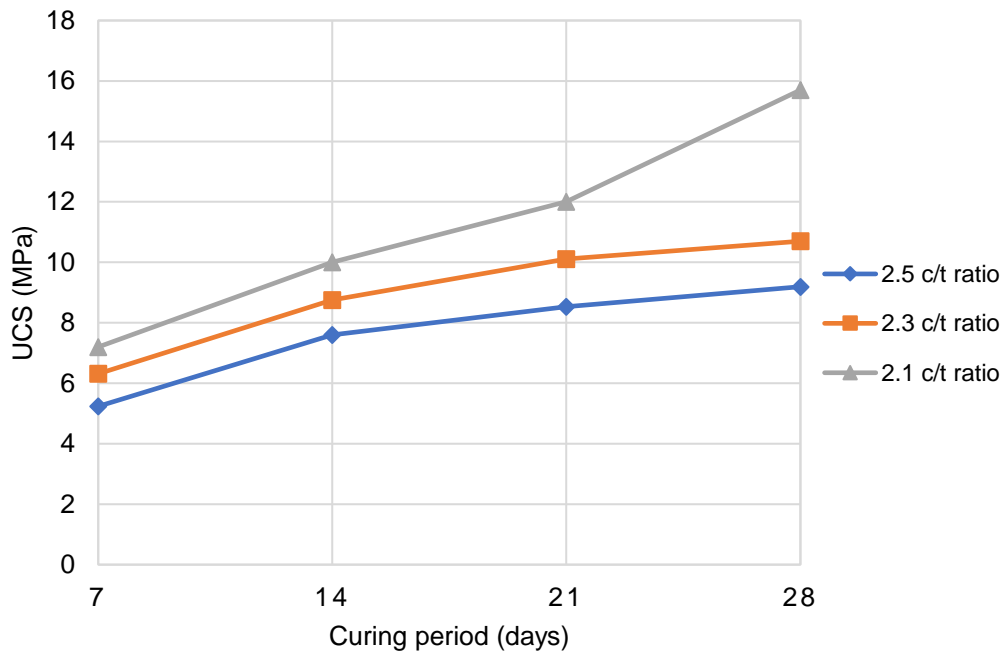


Figure 4.4 Effects of binder content on the strength of CTB samples for various binder contents

#### 4.6.3 Effect of layering on the performance of CTB samples

The effect of layering is demonstrated in Figure 4.5. The findings show that the strength of CTB decreases with the number of layering. However, the declining trend is significant at an early age. On the other hand, the strength of two-layered samples continuously declines regardless of the curing time. Meanwhile, the strength of three-layered samples gradually increases with curing time. After 28 days, the non-layered samples still demonstrate the highest strength compared to that of two-layered and three-layered samples. For the 2.5 c/t mix ratio, the UCS differences between non-layered samples and two-layered samples at all curing periods (7, 14, 21, and 28 days) are 10.58%, 18.42%, 19.20%, and 15.45%. Whereas the percentage differences between non-layered and three-layered samples are 14.69%, 15%, 14.87%, and 6.20%. Cao et al. (2016), Zhang et al. (2017) and Wang et al. (2020c) conducted an experimental study to investigate the mechanical properties of layered CTB. The authors corroborate that the strength of CTB decreases with an increase in CTB layers. However, none of the authors

reported an increase in the UCS of three-layered CTB at any stage. This may be because the authors excluded the effect of curing time by curing all the samples for 90 days before compressing them. Even so, a notable study by Chen et al. (2022b) reports that the UCS of CTB did not always decrease with an increase in the number of layers. In fact, when the number of layers exceeded 3, the change in the UCS of layered CTB is very negligible and the strength of CTB started increasing from layer number 4. Thus, corroborating the findings of this study.

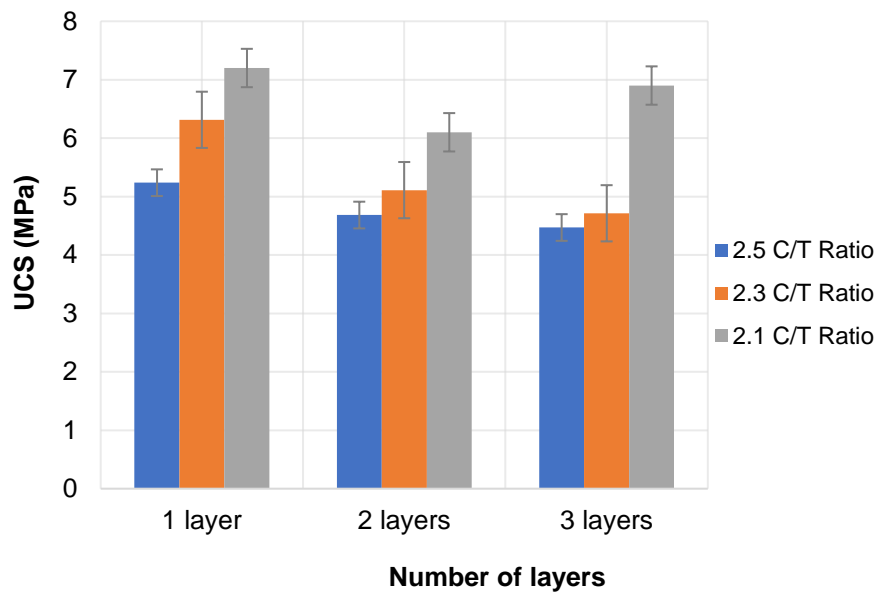


Figure 4.5 Effect of layering on the UCS values of CTB specimens for 2.5 c/t, 2.3 c/t and 2.1 c/t mix ratios

Instead, Zhang et al. (2022) postulate that when the layer number increases, the interface dislocation effect gradually increases. In this study, this effect was significantly observed when crushing the two-layered samples. The two layers were displaced from their position which led to the sudden deformation of the lower layer, and thus, the sample's deformation. The lower layer absorbs all the load which resulted in its great failure. As a result, the UCS results of the two-layered samples were negatively affected as compared to the rest of the samples. In contrast, the failure of the lower layer of the three-layered backfill does not spread to the top layer. Therefore, the rise of the UCS may be due to the residual strength of the top layer. Chen et al. (2022b) posited that with an increase in the number of layers, the residual strength of the peak also increases. Thus, provided layered CTB samples with lasting bearing capacity after failure. As a result, the safety of underground working is optimised through the enduring support system.



#### 4.7 Significance of the findings

In this Chapter, the strength development of layered backfill is studied with curing time and changing the number of layers. According to the results of the laboratory experiments, the strength gain of non-layered CTB samples is much higher than that of layered samples. Furthermore, the strength of layered samples increases with curing time regardless of the layering. Although the strength of the layered samples decreases with increasing layers, the strength does not always decrease but eventually picks up. A similar trend is observed concerning the elastic modulus of the layered samples with increasing layers.

The non-layered backfill has the highest elastic modulus as compared to the layered backfill. Whereas the layered backfill enters the elastic stage with lower stress exerted on the fill. Thus, with the increase in the number of layers, the elastic deformation stage became short. As a result, the elastic modulus of the layered backfill is lower than the non-layered backfill. The strength of non-layered (complete filling) samples gained more strength than two-layered and three-layered samples. The strength of the samples decreased with increasing layers. Although a slight increase in strength is observed in three-layered samples. This trend of strength loss is due to the backfilling gap adopted as practised in the mining industry since the bottom layer is poured first, the 24-h curing period allows the bottom layer to gain some strength. Following that, for layered samples; the second layer, and so on are expected to have less strength than the bottom layer. Likewise, the variation in strength between the layers (first, second and third) is expected. In this study, curing periods of 7, 14, 21, and 28 days were implemented, therefore, the differences were noticeable. Other authors that have tested layered CTB samples cured their samples for more than 60 days to minimise the effects of time differences (Fu et al., 2020; Wang et al., 2020c; Zhang et al., 2022). These authors reported an exponential decrease in the UCS of CTB samples with increasing layers. A worth-mentioning study by Chen et al. (2022a) on the mechanical properties of layered backfill samples has shown that the strength of CTB samples does not always decrease with increasing layers. Indeed, as much as the UCS of the samples decrease with increasing layers, when the number of layers exceeded 3 the UCS started to increase. Additionally, when the layers exceed 9, the change in UCS becomes negligible. Therefore, it can be concluded

that as much as the non-layered CTB structure possesses more strength than the layered CTB, the strength of CTB samples is not always dwindling.

#### 4.8 Conclusion

This chapter presented the findings obtained from the laboratory experiments when collecting empirical data. The findings from the Atterberg limit experimental tests were first presented, followed by the particle size distribution results. The next results to be presented was the XRF analysis, followed by the findings from the slump tests. Lastly, the findings of the compressive tests were presented, together with the elastic modulus results emanating from the compressive tests. Chapter 5 also outlines the procedure followed to develop the damage model that characterises the mechanical properties of backfill. The parameters used to develop the damage model were drawn from the findings of this chapter.

## Chapter 5 Development of deformations model on the mechanical performance of layered backfill support system.

### 5.1 Introduction

Firstly, this chapter mathematically modelled the mechanical behaviour of CTB samples as discussed in Chapter 4. The findings discussed in the previous chapter were used to develop predictive charts through curve fitting and deformation model based on the damage theory by Lemaitre (1984) at micro-scale level. The curve fitting functions used to develop the deformation model have boundary conditions in a range of value of curing periods, number of layers and binder content. That is between 7 and 28 curing days, maximum of three layers of backfill and a  $c/t$  ratio between 2.1 and 2.5. Outside this domain, the model and chart may not work.

### 5.2 Correlating the mechanical properties, curing time, binder content and layering of CTB cubes

This section discusses the results from the compressive strength tests obtained for each test after curing for 7 days, 14 days, 21 days and 28 days. The results are discussed in terms of the effects of curing time, binder content, and layering structure on the mechanical behaviour of CTB cubes. Effect of curing time on the performance of CTB cubes.

#### *5.2.1 Effect of curing time on the performance of CTB cubes*

To mathematically describe the relationship between UCS and curing time, different types of fitting functions such as linear, logarithmic, exponential, and power were implemented. The power function was deemed to be more adequate due to the highest correlation factor ( $R^2$ ) and took the following form:

$$UCS = a t^b \quad \text{for } 7 \text{ days} \leq t \leq 28 \text{ days} \quad (5.1)$$

Where  $UCS$  is the uniaxial compressive strength of the CTB;  $t$  is the curing period; and  $a$  and  $b$  are the fitting coefficients.

It is also worth noting that the use of Equation (5.1) may also be restricted within the range of the values of the experimental parameters considered in the preparation of the CTB samples. That is, there are several factors that affect the reliability of the equation. For example, a different equation can be derived for CTB cured for longer than 90 days. As exemplified in Figure 5.1, the curve-fitting of Equation (5.1) to one sample of data in Table 4.6 yields an average coefficient of determination ( $R^2$ ) of 0.9872. This means that at least 98.72% of the data can be explained using Equation (5.1).

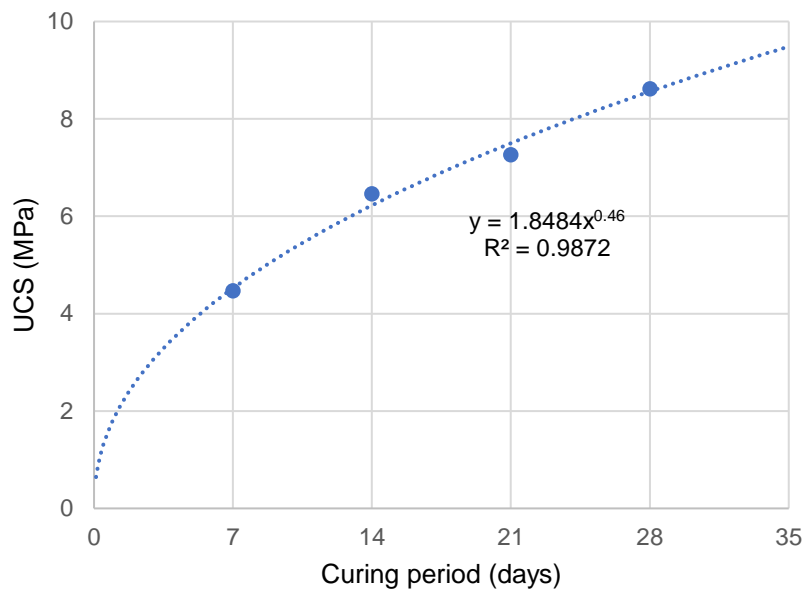


Figure 5.1 Effect of curing on the uniaxial compressive strength at 2.5c/t mix ratio for three-layered CTB samples

As can be seen in Table 5.1, R-square values are on average around 96% whilst the parameter  $a$  tends to rise and drop with an increase in binder content. Meanwhile, the parameter  $b$  does the opposite.

Table 5.1 The fitting and determinant coefficients associated with curing time and UCS of CTB of different combinations of c/t ratios and different layering patterns.

	<b>c/t mix ratio</b>	<b><math>a</math></b>	<b><math>b</math></b>	<b><math>R^2</math></b>
<b>1 layer</b>	<b>2.1</b>	1.83	0.634	0.9843
	<b>2.3</b>	3.03	0.389	0.9749
	<b>2.5</b>	2.44	0.409	0.9659
<b>2 layers</b>	<b>2.1</b>	2.21	0.541	0.9728
	<b>2.3</b>	2.87	0.317	0.8861
	<b>2.5</b>	2.29	0.375	0.9528

<b>3 layers</b>	<b>2.1</b>	2.59	0.506	0.9935
	<b>2.3</b>	2.07	0.438	0.9391
	<b>2.5</b>	1.85	0.460	0.9872

Likewise, to quantify the effect of curing time on elastic modulus, the exponential function was used for the purpose as it was found to be adequate:

$$E = fe^{kt} \quad \text{for } 7 \text{ days} \leq t \leq 28 \text{ days} \quad (5.2)$$

Where  $f$  and  $k$  are the fitting parameters related to the elastic modulus ( $E$ ) and curing time ( $t$ ). Curve-fitting was done for one sample of data.

In Figure 5.2. The corresponding  $R^2$  indicates that the exponential function has the highest accuracy as exhibited by Equation (5.2). As depicted by Figure 5.2, the curve-fitting of Equation (5.2) to one sample of data in Table 5.2 yields an average  $R^2$  of 0.9143. Likewise, this means that at least 91.43% of the data can be explained using Equation (5.2).

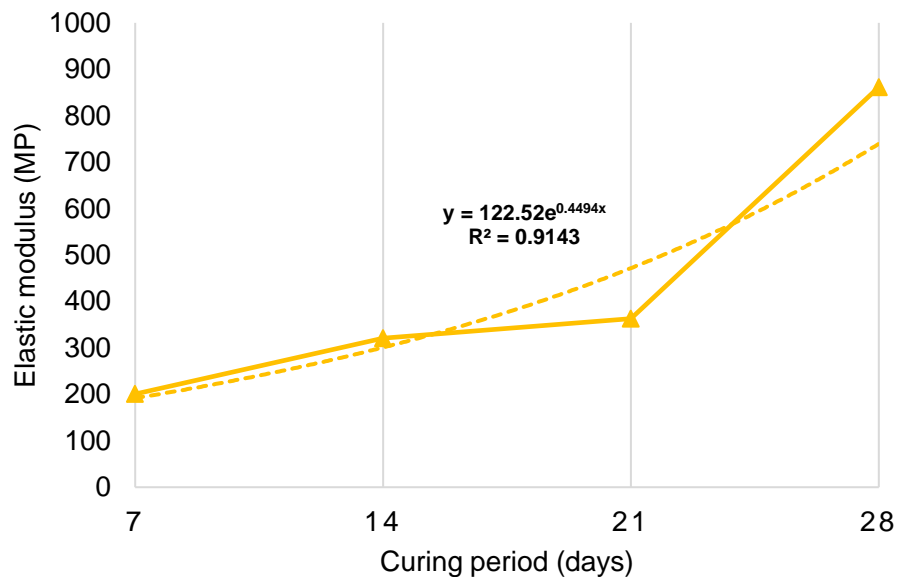


Figure 5.2 Effect of curing time on elastic modulus at 2.5c/t mix ratio for three-layered CTB samples

Table 5.2 The fitting and determinant coefficients associated with curing time and elastic modulus of CTB of different combinations of c/t ratios and different layering patterns.

	<b>c/t mix ratio</b>	<b><i>f</i></b>	<b><i>k</i></b>	<b>R<sup>2</sup></b>
<b>1 layer</b>	<b>2.3</b>	127.08	0.8644	0.935
	<b>2.5</b>	143.12	0.758	0.9099
<b>2 layers</b>	<b>2.3</b>	132.1	0.277	0.5402
	<b>2.5</b>	128.86	0.253	0.9477
<b>3 layers</b>	<b>2.3</b>	109.4	0.529	0.0.8104
	<b>2.5</b>	122.52	0.449	0.9143

### 5.2.2 Effect of layering on the performance of CTB cubes

To study the correlation between the number of CTB layers and UCS quantitatively, the linear, power, exponential, logarithm, and polynomial function of one variable is fitted in the graph (Figure 5.3). Due to lack of data points because of the nature of the graph, the decrease of R<sup>2</sup> with increasing curing time was highly visible. A power function was found best fitting to describe the data at R<sup>2</sup> of 0.9937 at 7 days, due to the moving trend of the graph. Thus, 99.37% of the data at 7 days can be characterised using Equation (5.3). The compressive strength of the samples decreased with increased number of layers; however, the strength gradually increases with more layers. Therefore, the trend does not follow a linear fashion.

$$\sigma_n = zn^{-m} \quad \text{for } 1 \leq n \leq 3 \quad (5.3)$$

Where  $\sigma_n$  is the UCS of CTB with respect to layering;  $n$  is the number of layers; and  $z$  and  $m$  are the fittings coefficients.

It is important to note that Equation (5.3) is limited to 3 layers as indicated and beyond that may produce inaccurate results. Therefore, additional data is required for more accurate modelling of the effect of layering on the strength of backfill.

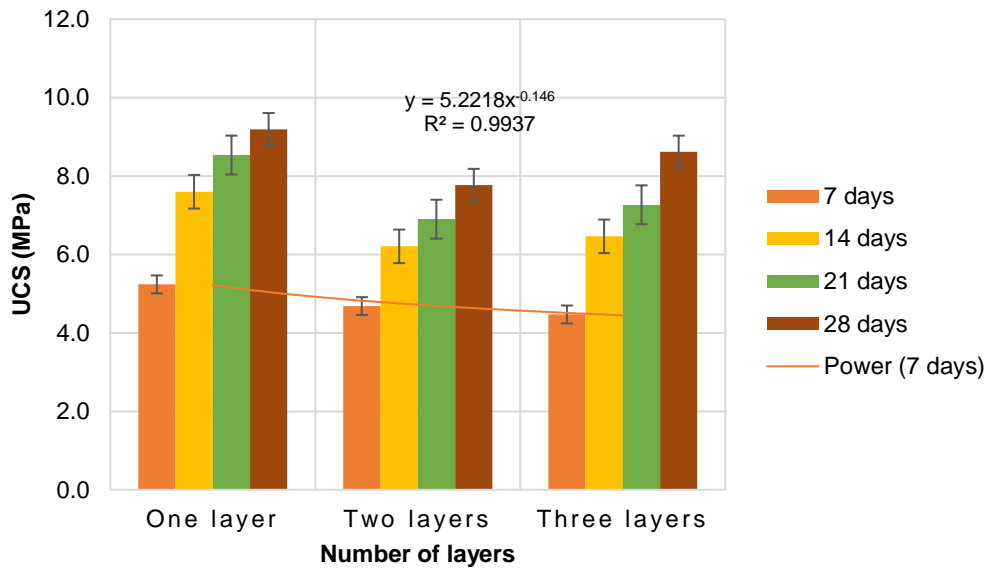


Figure 5.3 Correlation between UCS values and the layering of cemented tailings backfill samples.

As shown in Table 5.3, the  $z$  parameter increases with curing time, meanwhile, the  $R^2$  decreases significantly with curing time. This may be attributed to the high strength gain of the samples at early age while the strength gain becomes nearly flat at a later stage (28 days). Therefore, it can be deduced that it becomes difficult to predict the strength of CTB at longer curing time. This is because backfill support gains strength with time, and once the strength has matured, it becomes stable. Dong et al. (2019) attest that under normal conditions, there is no more strength loss of CTB after 120 curing days. Also, under harsh conditions such as high sulphide rich tailings, there is no more strength gain or loss after 360 days.

Table 5.3 The fitting coefficients associated with layering and UCS of CTB samples from 7-28 days of curing.

Curing period	$z$	$m$	$R^2$
7	5.2218	-0.146	0.9937
14	7.4184	-0.163	0.7501
21	8.3098	-0.164	0.7128
28	8.9161	-0.079	0.2968

Figure 5.6 shows the change of elastic modulus with an increase in the number of layers. It is evident that the elastic modulus decreases with the increase in layer number. These findings concur with the findings of Chen et al. (2022b) and Zhang

et al. (2022). They attest that the elastic modulus of CTB decreases with an increase in the layering of CTB. Although the UCS of three-layered samples seemed to be rising on days 7, 14 and 21, there is only a slight increase in elastic modulus from two-layered samples. This implies that the stiffness of layered CTB material is only fully achieved after long-term curing. These findings are supported by the fitting coefficients and coefficients of determination in Table 5.4. Curve fitting was conducted for all curing days and there are evident fluctuations of the  $R^2$ . As depicted in Figure 5.4, the highest elastic modulus was achieved after 28 days. That is when the sample was fully cured. Similarly, to quantify the effect of layering on elastic modulus, the power function was used for the purpose as it was found to be adequate. This is given by:

$$E_n = dn^{-w} \quad \text{for } 1 \leq n \leq 3 \quad (5.4)$$

Wherein  $d$  and  $w$  are the fitting coefficients associated with elastic modulus and layering while  $E_n$  is the elastic modulus of layered backfill.

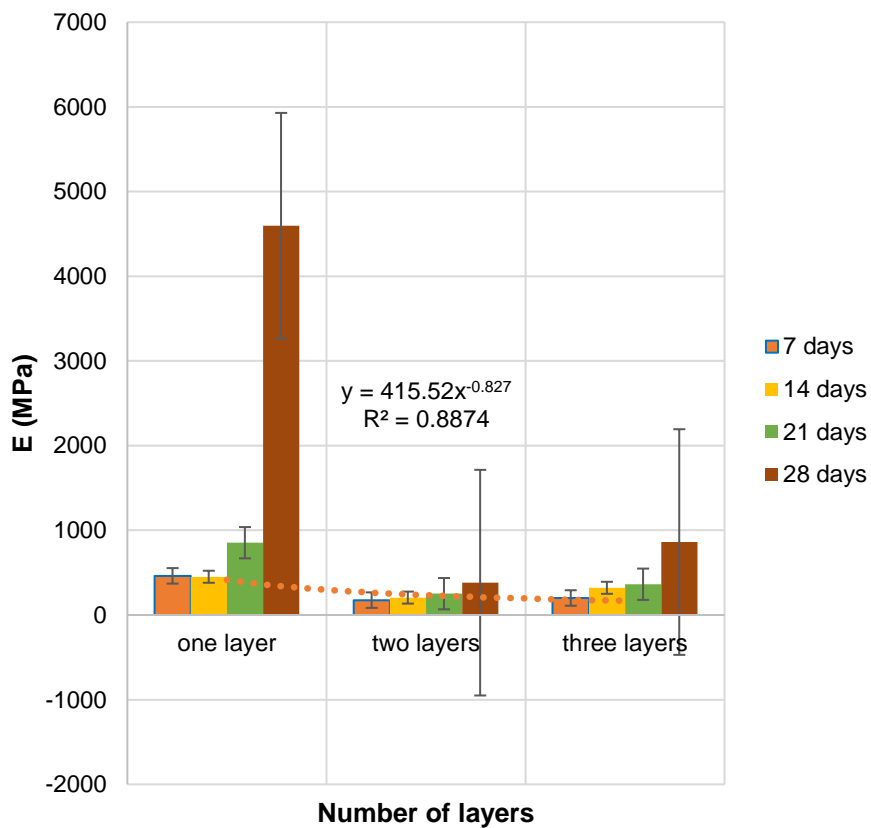


Figure 5.4 Effect of layering on the elastic modulus of CTB specimens for 2.5 c/t



Table 5.4 The fitting coefficients associated with layering and elastic modulus of CTB samples from 7-28 days of curing.

<b>Curing period</b>	<b><math>q</math></b>	<b><math>w</math></b>	<b><math>R^2</math></b>
<b>7</b>	415.52	-0.827	0.8874
<b>14</b>	393.4	-0.399	0.4792
<b>21</b>	724.37	-0.883	0.8252
<b>28</b>	3257.2	-1.746	0.9283

### 5.3 Development of a damage constitutive model for layered CTB

A damage mechanism was proposed by Professor Lemaitre (1984) to describe the stress-strain constitutive relation of damaged material. Lemaitre (1984) proposed that a damaged body at the macro-scale should be considered large enough to contain several defects. But small enough to be considered a material point of the mechanics of continua. That is, the constitutive damage equation can be derived from the constitutive equation of non-destructive material. Provided that the nominal stress in the constitutive model of non-destructive material is replaced by the effective stress after damage. For example, the damaged variable ( $D$ ) is expressed as (Cheng et al., 2021):

$$D = \frac{A - A_1}{A} \quad (5.5)$$

Where  $A$  and  $A_1$  denote the effective bearing area of the CTB sample in the non-destructive state and after the loading damage. The normal stress of the non-destructive material (undamaged stage) is generally exhibited by:

$$\sigma = \frac{F}{A} \quad (5.6)$$

Therefore, when the normal stress is replaced to define the damaged material, the effective stress is now expressed as:

$$\sigma^* = \frac{F}{A_1} \quad (5.7)$$

From Equations (5.5 – 5.7), the following can be derived:

$$\sigma^* = \frac{\sigma}{(1 - D)} \quad (5.8)$$

Therefore, from Equation (5.8), the normal stress can be expressed as:

$$\sigma = \sigma^* (1 - D) \quad (5.9)$$

Then, from  $E = \sigma/\varepsilon$ , the damage constitutive equation is derived as follows:

$$\sigma = E \varepsilon (1 - D) \quad (5.10)$$

where  $D$  is the loaded damage variable and  $E$  is the elastic modulus for the undamaged material. Now, according to the Weibull statistical distribution function, the damage evolution equation of the backfill sample can be written as (Liu et al., 2016b; Wang et al., 2020b):

$$D = 1 - \exp \left[ - \left( \frac{\varepsilon}{x} \right)^m \right] \quad (5.11)$$

Where  $x$  and  $m$  are fitting constants. When Equation (5.11) is substituted into Equation (5.10), the result is expressed as:

$$\sigma = E \varepsilon \exp \left[ - \left( \frac{\varepsilon}{x} \right)^m \right] \quad (5.12)$$

After multiple backfilling, the CTB structure has a layered appearance. Therefore, defects such as cracks are generated on the layered surface due to inconsistent hydration reaction time between the interfaces. This is the initial damage ( $D_n$ ) which is governed by the idea of macroscopic phenomenological damage mechanics. Therefore, the initial damage based on the elastic modulus for layered CTB is defined as (Fu et al., 2020):

$$D_n = 1 - \frac{E_n}{E_0} \quad (5.13)$$

Where  $E_0$ ,  $E_n$  and  $n$  respectively stand for the initial elastic modulus of intact CTB, the elastic modulus of the layered CTB and the layer number. In this study, the elastic modulus of CTB is defined as follows:

$$E_n = dn^{-w} \quad (5.14)$$

Therefore, the constitutive models can be summarised as:

$$\sigma = (dn^{-w}) \varepsilon \exp \left[ - \left( \frac{\varepsilon}{x} \right)^m \right] \quad (5.15)$$

$$D_n = 1 - \frac{dn^{-w}}{E_0} \exp \left[ - \left( \frac{\varepsilon}{x} \right)^m \right] \quad (5.16)$$

When substituting Equation (5.16) into Equation (5.10), the equation is now redefined as:

$$\sigma = -E \varepsilon \frac{dn^{-w}}{E_0} \quad (5.17)$$

Note that these empirical models are derived from the experimental results produced from the following domain:  $7 \text{ days} \leq t \leq 28 \text{ days}$  and  $1 \leq n \leq 3$ . Beyond these limits, suitable models may have to be developed. This is because the curve fitting functions substituted in the mode are limited within three data points. The lack of suitable laboratory equipment and financial resources to carry out extensive laboratory experiments brought about this limitation.

#### 5.4 Determination of the parameters of the damage constitutive model

The model parameters are determined through the derivation of Equation (5.15), and the assumptions made are (1)  $\varepsilon = \varepsilon_{pk}$ , (2)  $\sigma = \sigma_{pk}$ , and (3)  $d\sigma/d\varepsilon = 0$  where  $\varepsilon_{pk}$  and  $\sigma_{pk}$  are respectively the peak strain and peak strength. Therefore, from Equation (5.12):

$$\frac{d\sigma}{d\varepsilon} = E\varepsilon \left[ 1 - m \left( \frac{\varepsilon}{x} \right)^m \right] \exp \left[ - \left( \frac{\varepsilon}{x} \right)^m \right] \quad (5.18a)$$

When condition (3) is applied, the following condition is derived:

$$E \varepsilon \left[ 1 - m \left( \frac{\varepsilon}{x} \right)^m \right] \exp \left[ - \left( \frac{\varepsilon}{x} \right)^m \right] = 0 \quad (5.18b)$$

Where  $E \varepsilon$  and  $\exp \left[ - \left( \frac{\varepsilon}{x} \right)^m \right]$  cannot be equal to zero, Equation (5.18b) can be simplified as:

$$1 - m \left( \frac{\varepsilon}{x} \right)^m = 0 \quad (5.19)$$

Therefore, when Equations (5.12) and (5.19) are solved simultaneously, the following equation is generated.

$$\left( \frac{\varepsilon}{x} \right)^m = -\ln \left( \frac{\sigma}{E \varepsilon} \right) \quad (5.20)$$

When Equation (5.20) is substituted into Equation (5.19), the constant  $m$  is defined as:

$$m = -\frac{1}{\ln \left[ \frac{\sigma}{(dn^{-w})\varepsilon} \right]} \quad (5.21)$$

Equation (5.21) is substituted into Equation (5.19) to derive parameter  $x$ . Therefore, the term  $x$  can be estimated by:

$$x = \frac{\varepsilon}{m \sqrt{\frac{1}{m}}} \quad (5.22)$$

### 5.5 Validation of the constitutive model

To validate the proposed damaged model in this study, the experimental results are compared with those calculated using the proposed model. To quantify the deviation of the proposed model from the experiments, a percentage prediction error was calculated as given below (Wu et al., 1995):

$$Error = \left[ \frac{Measured\ Value - Predicted\ Value}{Measured\ Value} \right] \times 100\% \quad (5.25)$$

Wu et al. (1995) state that a percentage error of less than 5% is considered acceptable and not far from the measured value. Figure 5.5 compares the UCS results between the predicted value and the measured value. The percentage error of the non-layered, two-layered, and three-layered CTB samples are respectively 2.61%, 3.49% and 0.89%. The calculated and experimental results are in good agreement. The proposed solution confirms that the UCS of CTB decreases with the layering of backfill.

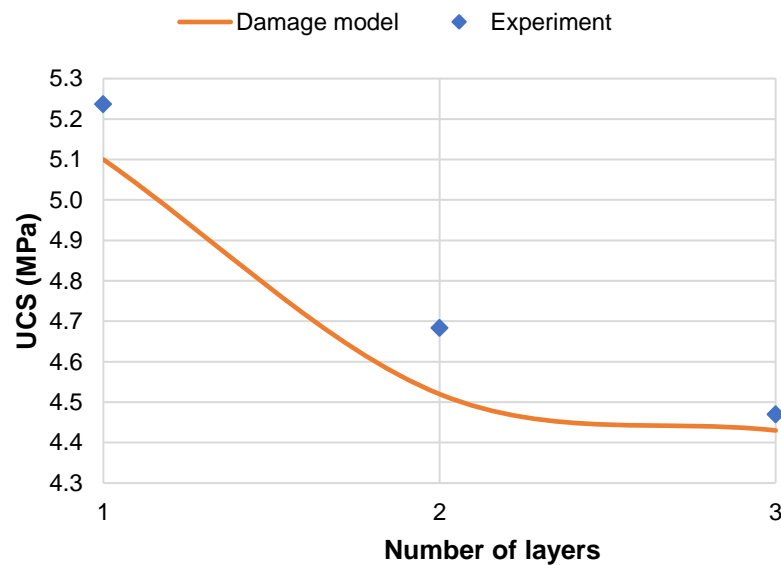


Figure 5.5 Comparison of the damage model and experimental UCS values of CTB samples after 7 curing days

As depicted in Figures 5.6, the UCS of CTB samples seems to be converging with that of the measured UCS. The cause of this trend is unknown. Moreover, the error percentages between the predicted value and experimental value are 1.70%, 2.87% and 1.27% respectively. The relative error [in %] also confirms the closeness of the predicted value to the measured value.

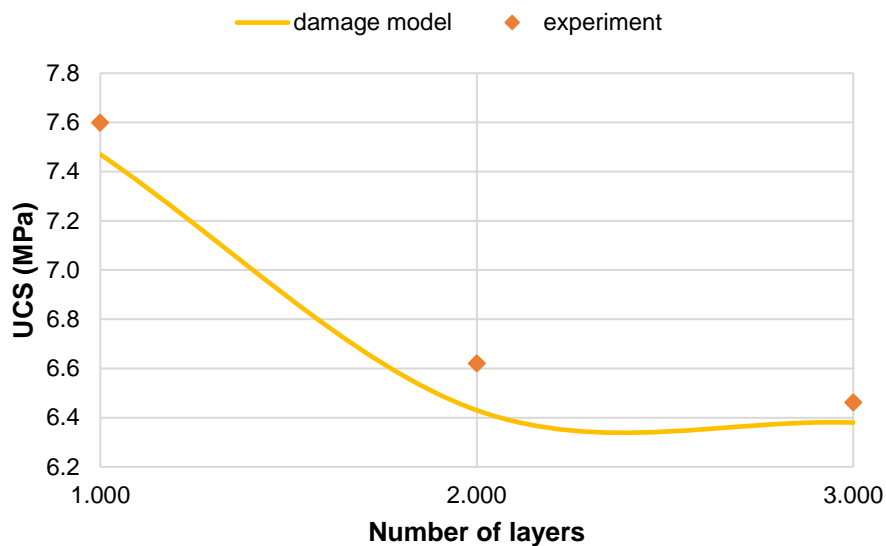


Figure 5.6 Comparison of the damage model and experimental UCS values of CTB specimens after 14 curing days

Figures 5.7 and 5.8 illustrate the predicted UCS after 21 and 28 days. After 21 and 28 days, the predicted strength seems to be gradually deviating from the measured value, however, the relative error is still less than 5%. That is 0.64%, 3.19% and 4.08% for the 21 curing days for non-layered, two-layered and three-layered samples. While the 28 days are recorded at 2.54%, 2.45%, and 4.37%. Therefore, the proposed solution can still be used to describe the mechanical properties of CTB, i.e., the *UCS* and elastic modulus of CTB.

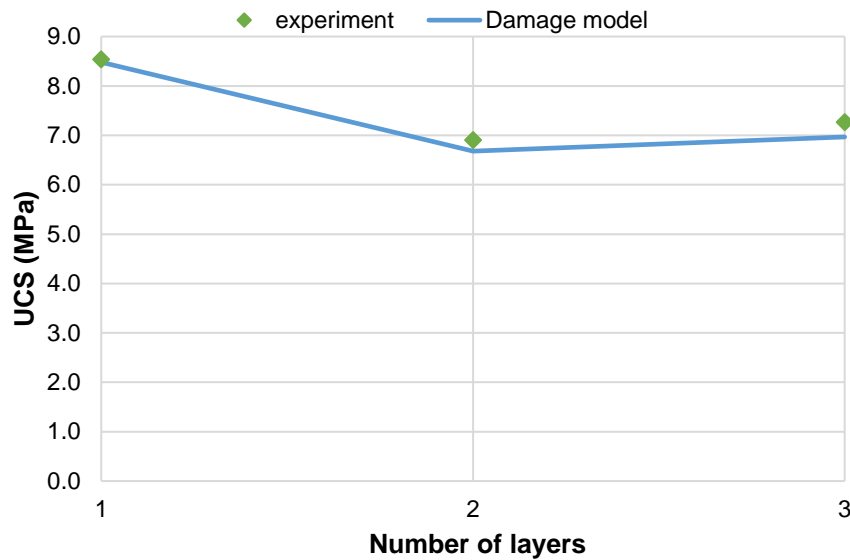


Figure 5.7 Comparison of the damage model and experimental UCS values of the CTB samples after 21 curing days

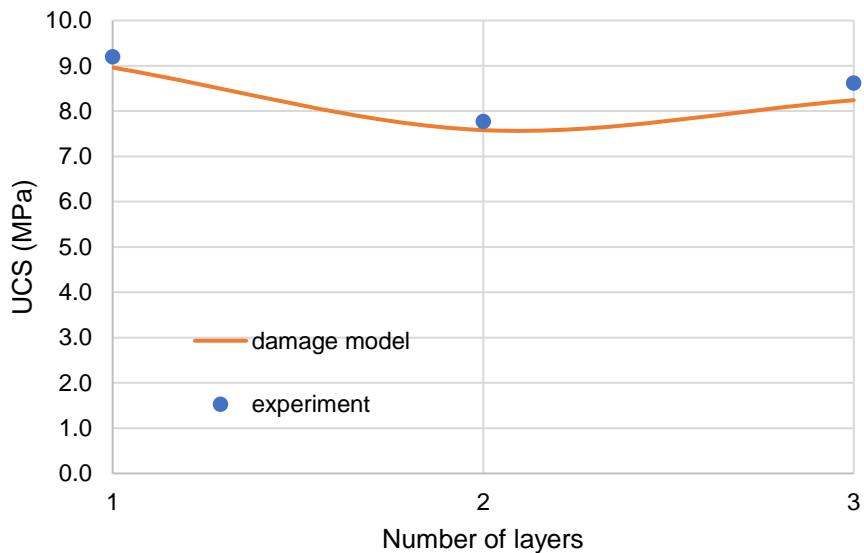


Figure 5.8 Comparison of the damage model and experimental UCS values of the CTB samples after 28 curing days

Based on the findings presented in this section, the UCS increases at first then decreases at a later stage with additional layers of CTB. Likewise, the deformation of the CTB samples increases then decrease with increasing number of layers. Chen et al. (2022b) studied the microdamage of layered CTB and found that the initial damage of CTB increase with increasing layers. The findings of Chen et al. (2022b) are supported by Fu et al. (2020). The CTB samples, therefore, demonstrate the elastoplastic criterion in Section 6.2. The same trend is observed in Figure 5.9, the damage variable, which was determined through Equation 5.19,

increases with increasing layers of backfill. Moreover, the damage seems to gradually reduces as more layers are added.

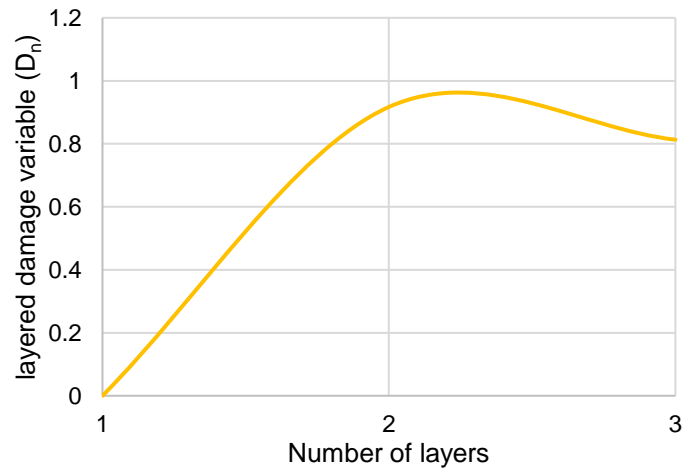


Figure 5.9 The evolution of the damage/deformation of CTB with layering.

### 5.6 Concluding remarks

A deformation model was developed in this section, based on the curve-fitting functions developed from the laboratory results. It is worth-noting that the curve-fitting functions are limited within three data points and between 7 to 28 days. That is, the prediction of the mechanical properties cannot be done beyond 3 layers of backfill. Therefore, the deformation model is also restricted to the same domain. Therefore, other models may have to be developed to address these limitations. The damage value of the layered CTB samples increases with the number of layers and then decreases gradually with the addition of more layers. The following chapter (i.e., Chapter 6) describes the stress-distribution around a backfilled stope through advanced numerical analysis.

## Chapter 6 Developing stress distribution charts in the vicinity of layered and unlayered backfill stopes.

### 6.1 Introduction

This chapter discusses the stress distribution of unlayered and layered backfilled stope. The basis of this chapter is numerical modelling conducted by using OPTUM G3 geotechnical analysis software. The development process of this model is discussed in Chapter 3; therefore, this chapter presents and discusses the results from the simulation. The numerical model follows a simulation of an underground backfilled stope by creating a 100 m block model with an excavation of a 20 m rectangular void. The void imitates an open stope in underground mining. The void is then filled with clay rock with defined backfill properties. The backfill material is backfilled in four different scenarios, i.e., complete filling, two-layered backfilling, three-layered backfilling, and four-layered backfilling. The stress distribution within the stope in all scenarios is studied and stress-strain curves are developed for each scenario. This chapter starts by outlining the governing equations for an elastoplastic model and thereafter, discusses the findings of the numerical analysis.

### 6.2 Governing equations for Mohr-Coulomb elastoplastic model

The model developed in this chapter obeys the Mohr-Coulomb failure criterion. As initially presented in Section 2.7 and Equation (2.5), the Mohr-Coulomb model is an elastic-plastic model which is usually used to simulate geomaterial behaviour, particularly soil. Two parameters from Hooke's law define the linear behaviour of the stress-strain curve, i.e., elastic modulus ( $E$ ) and Poisson's ratio ( $\nu$ ). The failure criterion of the material is defined by the friction angle ( $\phi$ ) and cohesion ( $c$ ) (Kok et al., 2009; Labuz and Zang, 2012). The associated flow rule for the material, which means the dilatancy angle ( $\psi$ ) used to model a realistic irreversible change in volume due to shearing is zero (Kok et al., 2009). It is said that material is elastic and perfectly plastic when it has reached a state of yield. The failure envelope of the Mohr-Coulomb elastoplastic model and the stress/strain curve is shown in Figures 7.1a and 7.1b (Wang et al., 2021b).



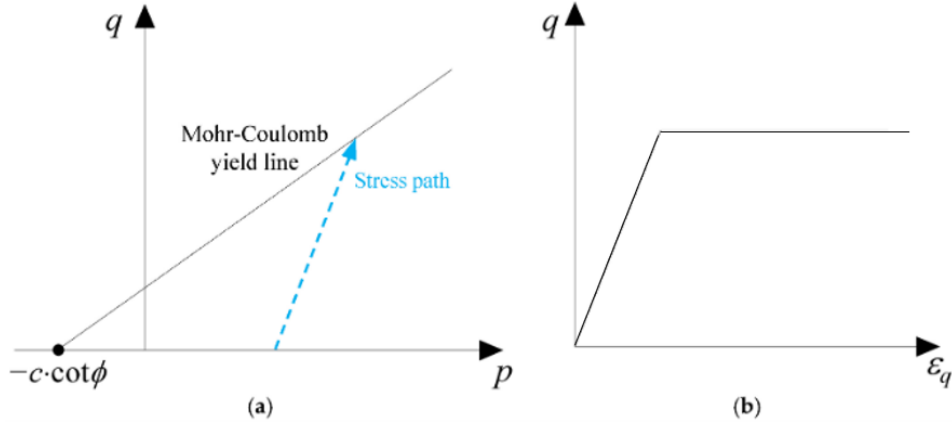


Figure 6.1 The theoretical Mohr-coulomb elastoplastic model: (a) Yield surface in the mean ( $p$ ) and deviatoric ( $q$ ) stress space; and (b) Stress-strain curve

The mean ( $p$ ) and deviatoric ( $q$ ) stresses are expressed as follows (Wang et al., 2021).

$$p = \frac{(\sigma_1 + \sigma_2 + \sigma_3)}{3} \quad (6.1)$$

$$q = \sqrt{\frac{(\sigma_1 - \sigma_2)^2 + (\sigma_2 - \sigma_3)^2 + (\sigma_3 - \sigma_1)^2}{2}} \quad (6.2)$$

where  $\sigma_1$ ,  $\sigma_2$ , and  $\sigma_3$  are the major, intermediate, and minor principal stresses, respectively.

Once the state of the stress has reached the yield level, infinite plastic shear strain occurs under a constant load. The relationship between the stress and strain in the elastic regime is expressed as (Wang et al., 2021b):

$$\varepsilon_1 = \frac{1}{E} [\sigma_1 - \nu(\sigma_2 + \sigma_3)] \quad (6.3)$$

$$\varepsilon_2 = \frac{1}{E} [\sigma_2 - \nu(\sigma_1 + \sigma_3)] \quad (6.4)$$

$$\varepsilon_3 = \frac{1}{E} [\sigma_3 - \nu(\sigma_1 + \sigma_2)] \quad (6.5)$$

Where  $\varepsilon_1$ ,  $\varepsilon_2$  and  $\varepsilon_3$  are the stress tensor components;  $\sigma_1$ ,  $\sigma_2$  and  $\sigma_3$  are the strain tensor components. And the equations can be rearranged for stress as:

$$\sigma_1 = \frac{2G}{1-2\nu} [(1-\nu)\varepsilon_1 + \nu(\varepsilon_2 + \varepsilon_3)] \quad (6.6)$$

$$\sigma_2 = \frac{2G}{1-2\nu} [(1-\nu)\varepsilon_2 + \nu(\varepsilon_1 + \varepsilon_3)] \quad (6.7)$$

$$\sigma_3 = \frac{2G}{1-2\nu} [(1-\nu)\varepsilon_3 + \nu(\varepsilon_1 + \varepsilon_2)] \quad (6.8)$$

Where  $G$  is the shear modulus which is denoted by:

$$G = \frac{E}{2(1+\nu)} \quad (6.9)$$

When plastic strain is considered, the total strain in the CTB is defined by two parameters: the reversible elastic strain ( $\varepsilon_e$ ) and the irreversible plastic strain ( $\varepsilon_p$ ). It is expressed as (Hasanzadehshooiili et al., 2012; Cui, 2017):

$$\varepsilon = \varepsilon_e + \varepsilon_p \quad (6.10)$$

The plastic strain increment is characterised by the flow rule as given below:

$$\Delta \varepsilon_i^P = \lambda \frac{\partial Q}{\partial \sigma_i} \quad (6.11)$$

Where  $\sigma_i$  represents the current stress component or initial stress state;  $\lambda$  is the plastic multiplier, and  $Q$  denotes the plastic potential defined by:

$$Q = J_2 - \xi F_0^2 f_\pi^2 \quad (6.12)$$

The coefficient  $\xi$  serves to control the plastic deviatoric and volumetric strain components. When  $\xi = 1$ , the plastic potential function is the same as the yield criterion, i.e.,  $Q = F$ , so the flow rule is associated. The term  $J_2$  is the second invariant of the deviatoric stress tensor given by (Tao et al., 2022; Zeng, et al., 2022):

$$J_2 = \frac{[(\sigma_1 - \sigma_2)^2 + (\sigma_2 - \sigma_3)^2 + (\sigma_3 - \sigma_1)^2]}{6} \quad (6.13)$$

The plastic behaviour of the CTB is governed by the Drucker-Prager yield criterion (Cui, 2017; Tao et al., 2022):

$$f = \alpha_p I_1 + \sqrt{J_2} - k_p \quad (6.14)$$

Where  $I_1$  is the first stress invariant ( $I_1 = \sigma_1 + \sigma_2 + \sigma_3$ );  $\alpha_p$  and  $k_p$  are the material parameters of the Drucker-Prager criterion or the internal friction angle and cohesion respectively. They can be expressed as follows (Tao et al., 2022):

$$\alpha_p = \frac{\sin \phi}{\sqrt{3}\sqrt{3+\sin^2 \phi}} \text{ and } k_p = \frac{3c \cos \phi}{\sqrt{3}\sqrt{3+\sin^2 \phi}} \quad (6.15)$$

In this study, the effect of the mechanical parameters on binder hydration products is neglected. Therefore, the relationship between the cohesion, friction angle, and

binder hydration is not discussed. Both parameters were kept constant during the modelling process.

The equations presented in Section 6.2 are the governing equations for material that obeys elastoplastic criterion. The manual for the OPTIMUM G3 software does not specifically state the exact governing equations used to develop their software, however, it also provides the basic governing equations for elastoplastic criterion. The simulation model presented here was developed as per the steps discussed in Section 3.4.

### 6.3 Results and discussions

This section presents and discusses the numerical analysis developed using OPTUM G3 software. An open stope in a 1000 m deep mine was simulated to study the stress distribution around the stope as compared to a backfilled stope with different layers. The section starts by discussing the stress distribution around an open stope. Thereafter, the first backfilling strategy to be analysed is the single pour, followed by the double-layered fill to the four-layered backfill. The rockmass and the backfill properties inserted in the software as indicated in Tables 3.3 – 3.4. The results show the compressive principal stress, strain, displacements, and shear dissipation within the stope.

#### 6.3.1 Case 1: Open stope

After the excavation of the stope, the numerical analysis shows that the principal stress is higher at the outer boundaries of the rock mass as shown in Figure 6.2. The major principal stress only was presented with exclusion of the intermediate and minor principal stress because the change in stress was similar. Additionally, the main purpose of the numerical analysis was to study the change in stress in general within the stope, therefore, as it was observed that the major, intermediate, and minor principal stresses change in a similar fashion, it became irrelevant to present all of them. The major principal stress was selected because it is the highest magnitude. The same reasoning applies to the exclusion of intermediate and minor principal strain.

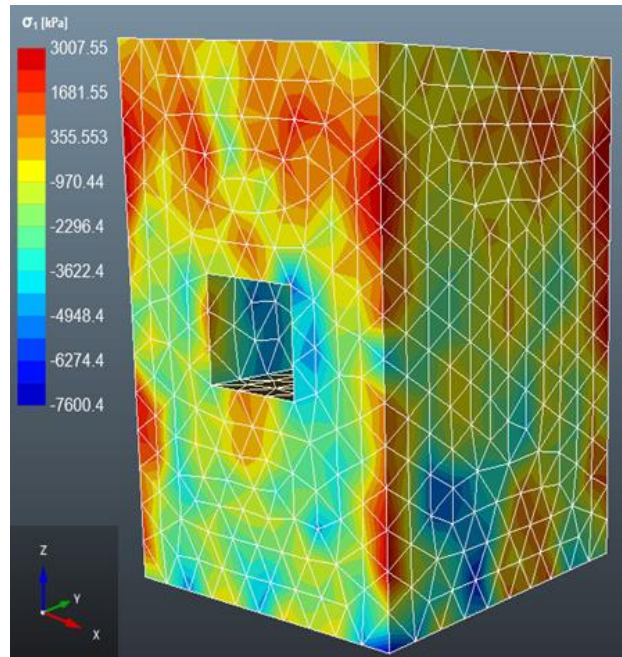


Figure 6.2 Distribution of the major principal stress ( $\sigma_1$ ) in the open stope

Whereas the principal stress is low at the boundaries of the excavation. Moreover, the principal stress is very high at the top of the rock mass, this may be due to the stope closure triggered by the excavation activity (Sobhi and Li, 2017). The principal stress, after excavation, is at least 3 MPa, lower than the overburden stress. The stress distribution around the opening is distributed to accommodate the disturbance in the stress field (Newman, 2018).

### 6.3.2 Case 2: Non-layered backfilled stope

This section discusses the findings of the unlayered backfilled stope. To simulate the backfilling process, the 20 m open stope was filled with 20 m clay rock that obeys MC criteria and the properties of the material was defined as per the backfill material. Figure 6.3 depicts a stress transfer from the rock mass to the backfill material. The principal stress is high at the top of the rock mass and the backfill material. Meanwhile, a rapid stress decrease is observed continuously towards the bottom of the rock mass. The stress level is completely low at the bottom of the rock mass, signifying the presence of stress transfer between the backfill and the rock mass (Newman, 2018). Therefore, failure will be expected at the backfill pillar. The rock located at the bottom of the backfill is also experiencing some stress as it is also carrying the load from the settlement of the backfill. However, the major principal stress has declined from 3 MPa to 0.132 MPa (95.6% decrease). The

results show that there is negative compressive strain, meanwhile, the lateral strain is sitting at 0.0012. This may be an indication of confinement to the backfill from the sidewalls due to the horizontal stress (Al-Heib et al., 2010). Although the strain is almost negligible, it seems to intensify in the rock mass and the upper part of the backfill. Whilst the bottom part of the fill is the least strained, thus, the change in the volume of material would be expected on the upper part of the backfill. Moreover, there is evident shear dissipation along the interface between the backfill and the rock mass. The negative stress and strain within the rock mass and the slope is due to compressive stress whilst the positive stress and strain signify tensile stress. Therefore, as shown in Figure 6.3, the bottom part of the backfill is highly compressed as compared to the other areas of the backfill.

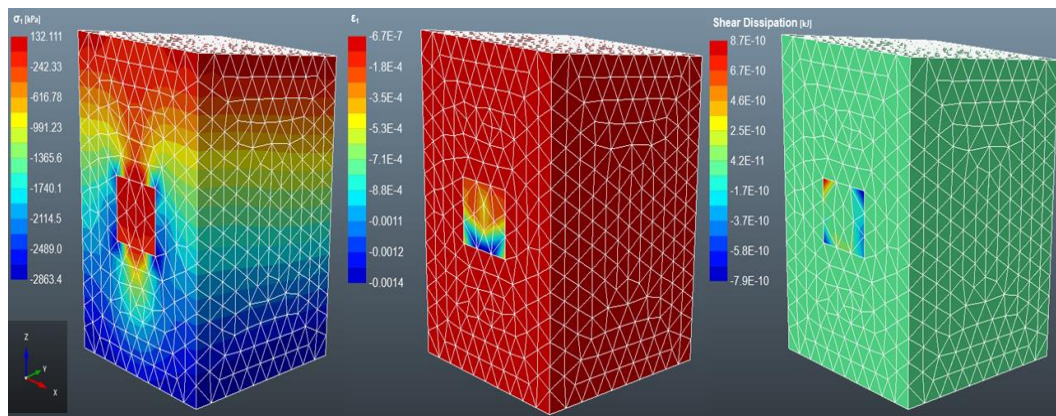


Figure 6.3 Distribution of the major principal stress ( $\sigma_1$ ), major strain stress ( $\epsilon_1$ ), and shear dissipation in a non-layered backfilled slope

The backfill material seems to have experienced the most displacement due to the deformations than the rock mass (see Figure 6.4). This is because the stress is highly concentrated in the backfill mass. The displacement in the x-, y- and z-directions are 0.00046 m, 0.000059 m, and 0 m respectively. Without effective regional support, the displacement along the z-direction would be larger than the x- and y-displacements due to gravity (Wang et al., 2013). However, a zero displacement in the z-direction indicates that the backfill support is resisting the slope closure. According to Al-Heib et al. (2010), backfill reduces vertical stress and increases horizontal stress which improves the stability of the slope. Thus, the horizontal displacement is due to the horizontal stress exerted on the backfill. Furthermore, the evidence of the displacement in the x- and y-directions is visible in the rock-fill interfaces.

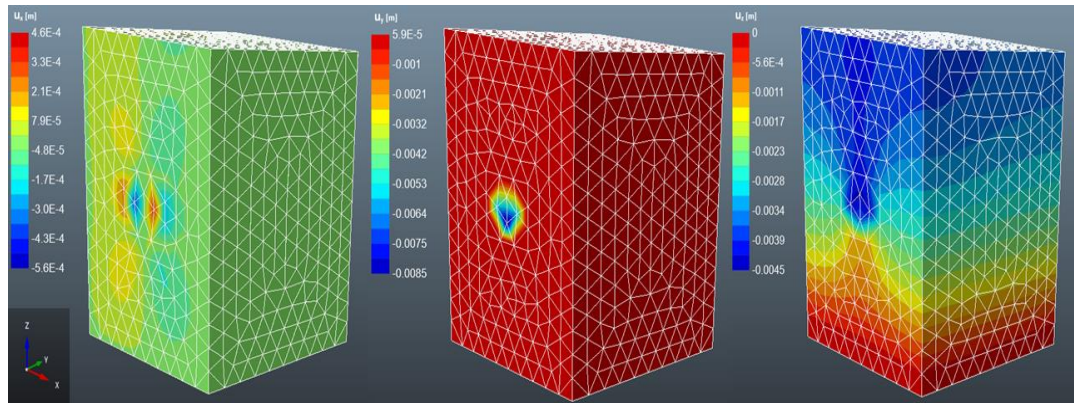


Figure 6.4 Displacement of the backfilled slope in the x-, y- and z-directions

### 6.3.3 Case 3: Double layered backfilling

A two-layered backfill slope was simulated by filling the open slope with two equal layers of 10 m of backfill, the properties remain the same. Once the properties are defined from the first stages of simulation, there is no further action to define the properties. The software keeps the same properties, unless the user wants to change them. The stress distribution in a two-layered backfill is similar to single-layered backfill (see Figure 6.5). However, the major principal stress has declined from 3 MPa to 0.134 MPa, which is only a 1.51% difference from the single-layered backfill. Therefore, there is only a slight decrease in the strength of the backfill from no layering to two layers. Similarly, there is very little to no strain in the vertical direction in two-layered backfill. Although, there is some negligible strain from the upper part of the backfill towards the middle of the backfill material. Meanwhile, for non-layered backfill, the shear dissipation was along the interfaces between the rock mass and backfill. Whereas in two-layered backfill, the shear dissipation is visible at the bottom rock-fill interface. The settlement of the backfill generates shear stress at the rock-fill interface, the shear stress is determined by the level of friction at the interface (Koupouli et al., 2016).

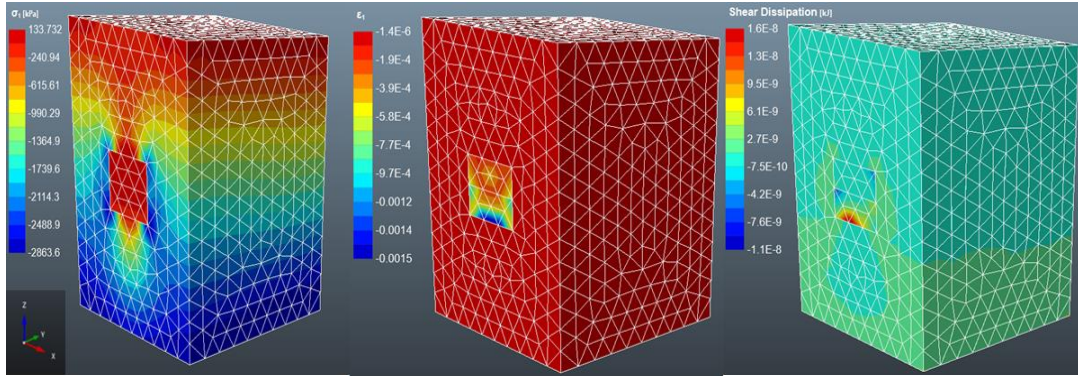


Figure 6.5 Distribution of the major principal stress ( $\sigma_1$ ), major strain stress ( $\epsilon_1$ ), and shear dissipation in a two-layered backfilled slope

According to Figure 6.6, the displacements in the x-, y- and z-directions are 0.0005 m, 0.000068 m, and 0 m respectively. The displacement of the two-layered backfill has slightly increased by 8.70%, 15.25% and 0%, respectively, as compared to the non-layered backfill.

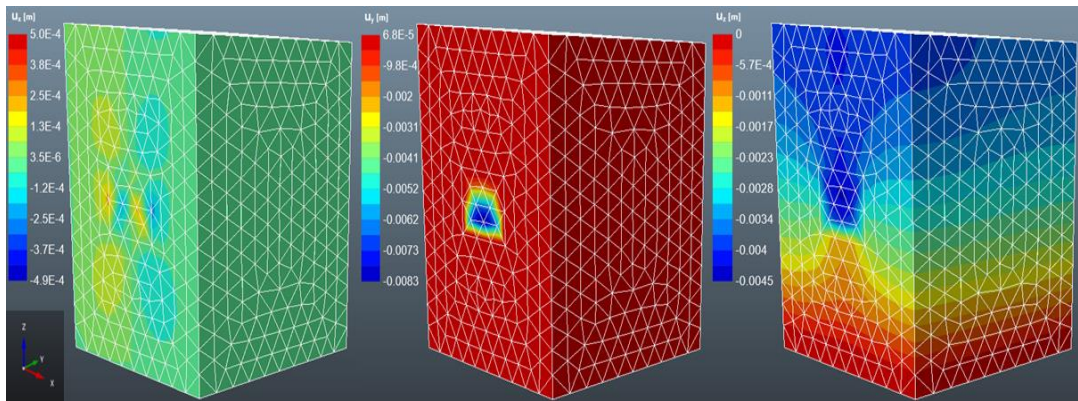


Figure 6.6 Displacement of the two-layered backfilled slope in the x-, y- and z-directions respectively

#### 6.3.4 Case 4: Three-layered backfilling

The three-layered backfill was simulated by filling the open slope with three layers of backfill (clay rock). The thicknesses of the layers are respectively 6 m, 6 m, and 7 m. The 7 m backfill layer is to fill up the 20 m slope. According to Figure 6.7, the major principal stress and strain increase exponentially with an increase in layering. The major principal stress after the filling is 0.141 MPa, i.e., a 6.38% and 4.96% increase from the non-layered and two-layered backfill. While the stress distribution is the same as the non-layered and two-layered backfilled slope, there is no evidence of shear dissipation in the three-layered backfill. It is worth noting though that the layers for the three-layered backfilling strategy are not equal in

length, unlike in other cases. The slope was filled with two 7 m layers plus one 6 m layer to a reach 20 m slope. Similarly, Chen et al. (2022) investigated the mechanical properties of layered backfill. The group of researchers observed a decline in the strength of the samples as the number of layers increased. Additionally, Chen et al. (2022) postulate that the strength of layered backfill samples did not always decrease with an increase in the number of layers. When the number of layers exceeded 3, the change in the strength of the layered samples is negligible.

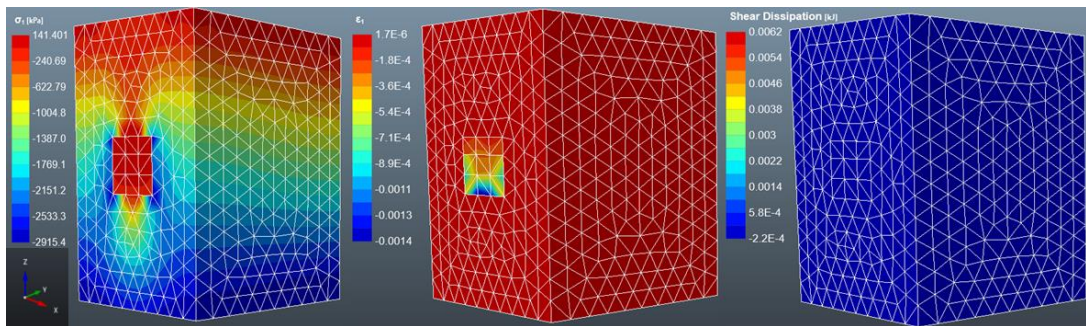


Figure 6.7 Distribution of major principal stress ( $\sigma_1$ ), major strain stress ( $\epsilon_1$ ), and shear dissipation in a three-layered backfilled slope

As depicted in Figure 6.8, the displacements in the x-, y- and z-directions are 0.00069 m, 0.000068 m, and 0 m respectively. When comparing to the non-layered backfill, the three-layered backfill has been displaced 33.33% higher in the x direction than the non-layered backfill. However, similar to two-layered backfill, the y- and z-displacement have increased by 15.25% and 0%. Thus, there is not much difference in the lateral confinement occurring in both two and three-layered backfill material.

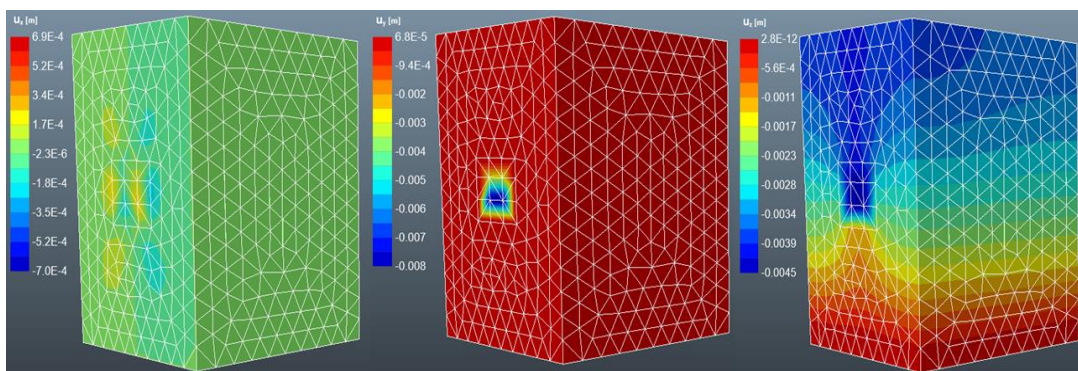


Figure 6.8 Displacement of the three-layered backfilled slope in the x-, y- and z-directions respectively



### 6.3.5 Case 5: Four-layered backfilling

The 20 m slope was filled by four equal layers of 5 m. In the case of four-layered backfill, the major principal stress, major strain and shear dissipation have increased significantly compared to non-layered backfill (see Figure 7.9). The numerical analysis shows that the stress within the stope is 233.555 MPa. This is a 77.27% increase compared to the non-layered backfill. And the strain increased by 14.93%. Meanwhile the shear dissipation seems to have spread to the lower boundaries of the rock mass. The strain also intensifies towards the inner parts of the backfill, but it does not affect the bottom part of the fill body. These results are supported by Chen et al. (2022b), the authors used a micro-mechanism technique to study the damage of layered backfill samples. They report that as the number of layers increases, there is excessive accumulation of damage in the middle layer. Therefore, the load is not transferred to the bottom of the backfill body and thus, maintains a certain strength.

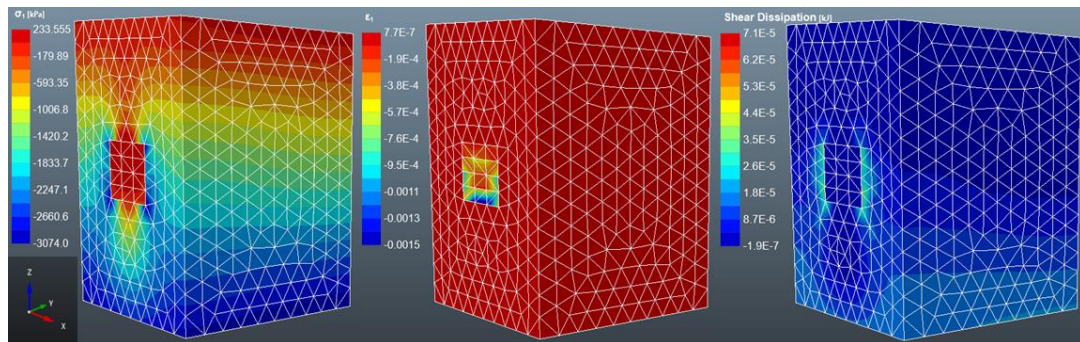


Figure 6.9 Distribution of major principal stress ( $\sigma_1$ ), major strain stress ( $\epsilon_1$ ), and shear dissipation in a four-layered backfilled stope

Although the x-, y- and z-displacements of the four-layered backfill seem to have decreased (17.39%, 7.35% and 0%) compared to the three-layered fill, the displacement is high in the backfill material compared to the rock mass. Unlike in the previous cases where the displacement was visible in the rock mass. Thus, the rock mass has transferred most of the strain to the backfill material (see Figure 7.10).

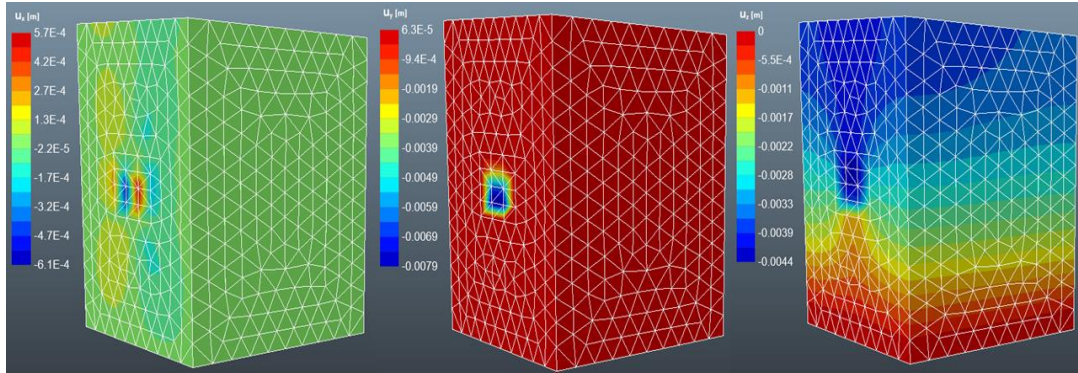


Figure 6.10 Displacement of the four-layered backfilled slope in the x-, y- and z-directions respectively

#### 6.4 Deformation curves

The stress-strain behaviour of the backfill is consistent with the observations made by several authors (Liu and Fall 2022; Tan et al., 2020; Zhao et al., 2022). The deformation of the CTB can be divided into four stages:

- Micro-pore compaction stage (A): At the beginning of the curve, a concave shape is observed, which indicates the compaction of the internal pores of the CTB structure under compressive pressure. It is at this stage that the curve becomes a straight line, and the deformation enters the linear elastic stage.
- Linear elastic stage (B): This stage is denoted by the strain line curve. This is where the internal pores of the CTB are further compacted as the confining pressure continues to increase. However, the pressure does not cause any cracks in the CTB, and this stage is representing the elastic modulus of the material.
- Plastic yield stage (C): In this stage, cracks are generated when the stress reaches its highest peak. The inner cracks expand gradually and worsen until the rapture. As a result, the curve exhibits a convex upward shape.
- Post-peak stage (D): The microcracks continue to expand and gradually evolve into primarily visible cracks. Thus, as the cracks propagate, the load-bearing capacity of the CTB decreases. Consequently, the CTB structure has become fully damaged.

According to Figure 6.11, the deformation behaviour of nonlayered CTB seems to shift from ductile to brittle behaviour (CD). Similar findings are recorded by Liu and Fall (2022). This phenomenon is known as the strain hardening/softening behaviour (Cui and Fall, 2016; Fall et al., 2007). The authors attribute this deformation behaviour to the increased stiffness of the CTB structure. The increase in confining pressure results in a change in the mode of failure of the CTB at peak stress (Cui and Fall, 2016; Fall et al., 2007). The elastic modulus of the backfill was measured by calculating the gradient of slope AB.

The deformation curve of the two-layered backfill does not differ much from the non-layered backfill. Even the stress in the backfilled slope increased by 1.51% from non-layered to two-layered backfill. As shown in Figure 6.11, the last stage displays a minor fluctuation in the deformation curve. This may be caused by the undamaged second layer of the backfill. When the first layer has failed, the second layer remains intact as observed during the laboratory experiments (Wang et al., 2019). Similar findings were observed by Wang et al. (2020c) in their experimental investigation of the mechanical behaviour and damage evolution of layered backfill. According to the group of authors, when the load exceeds the maximum pressure-bearing capacity of the sample, the sample becomes unstable and deformed. However, due to the residual strength of the sample, the stress-strain curve does not decrease rapidly but advances slowly forward. The elastic modulus for the two-layered backfill is lower than the non-layered fill.

On the other hand, the three-layered backfill perfectly obeys the elastoplastic deformation behaviour. The deformation behaviour of three-layered backfill goes through four different stages as discussed previously. Initially, the interface of the different layers in the CTB remains intact under the continuous load and the internal cracks are continuously compacted. This stage is denoted by the concave shape at the beginning of the stress-strain graph. Furthermore, the layered backfill gradually exhibits elastic properties as the pores are further compacted. The linear growth in the graph demonstrates this behaviour. When the material has reached the peak strength, the stress-strain curve shows a slow decrease trend after the peak. Thus, the CTB material indicates a ductile failure pattern (Zhang et al., 2022).

The deformation curve of the four-layered backfilled depicts loading and unloading failure characteristics (Gao et al., 2022a; Wang et al., 2020c). The post-peak point (CD) depicts a zigzagged shape, i.e., the peak stress experiences the rise and fall

pattern. The initial stress increase is due to the instability of the top layer then the stress reduces due to the elastic deformation of the next layer. Eventually, when the next layer goes through the crack propagation stage, the stress rises again, and the process repeats itself. Zhang et al. (2020) reported similar deformation behaviour. However, the authors investigated the deformation behaviour of CTB in a sub-zero temperature environment. The UCS rise and fall were attributed to the hydration process at an early age and the effect of freeze-thaw, respectively. This deformation cycle may eventually lead to the deterioration of the CTB structure. The four-layered backfill has the lowest elastic modulus.

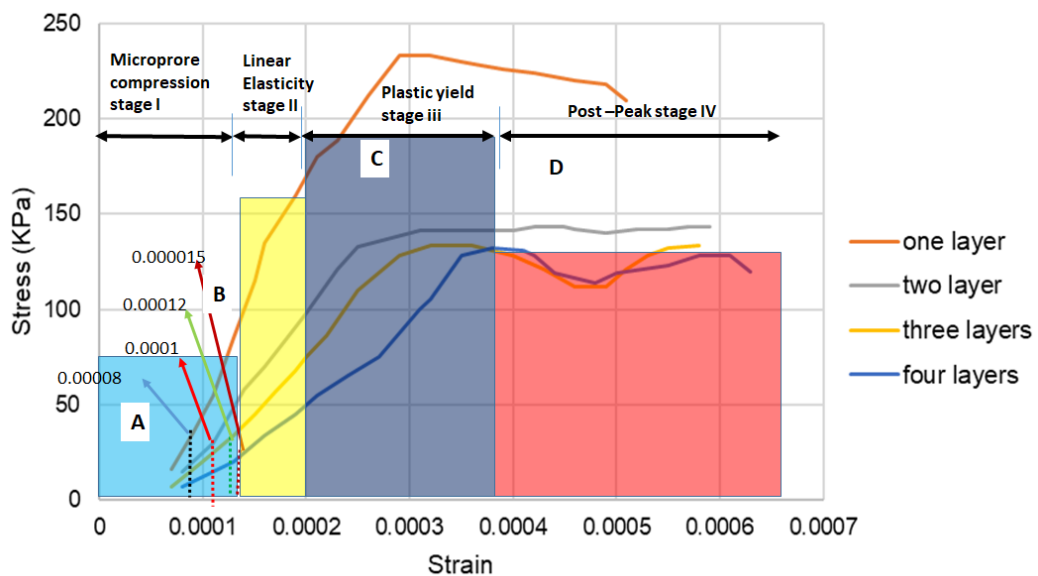


Figure 6.11 Stress vs strain curves for layered backfill.

Further analysis was to look into deformation stages presented by the model with regards to the CTB material within the slope. It was denoted that the deformation has shown four deformation behaviour of the CTB, these results correlate very well with some of the recent studies such as those of Chen et al., (2022). Following that, Chen et al., (2022) four deformation stages were presented, and those stages include “(I) a micro-pore compression stage, (II) a linear elastic stage, (III) a plastic yield stage, and (IV) a post-peak stage” similar results were observed as denoted by Figure 6.11. Indeed, one may point out that the non-layered backfill has demonstrated very low deformation in stage I as compared to the various layered backfill support system. A similar trend has been observed by Chen et al., (2022) and others as documented in the previous sections. It is believed that the introduction of layered CTB has contributed largely to the micro-pore compression

stage of the stress–strain curve which changes to the micro-pore and this micro-pore initiates crack quicker as compared to the non-layered backfill. One may also denote that the effect of shearing may also have played some cardinal role in the deformation process of layered backfill.

In stage II the simulation validated the laboratory results as well. In this regard, the non-layered backfill appeared to present a high elastic modulus yet the layered backfill system appeared to experience a low elastic modulus. Indeed, one may point out that elastic modulus is directly proportional to the stress, yet the increase in stress required to deform non-layered backfill is always higher than the layered backfill support system. Looking into elastic deformation the layered backfill support system presents large deformation as compared to the non-layered, these results correlate very well with studies such as Li et al. (2022) and Gao et al. (2022b). These results provide confidence that a non-layered backfill system should be expected to perform better as compared to a layered backfill system. Following that, a significant observation has been made and it was deduced that the increase in layers has an impact on elastic deformation, in fact, the increase in layering also contributes largely to the elastic deformation of the backfill support system. Scientifically, it has been argued by various authors such as Xu et al. (2019a), and Zhang et al. (2022) that despite the fact that backfill support system cures with time but the stratified backfill does not necessarily cure with similar duration as non-stratified, this leads into micro-pore remaining open while crack propagation occurs quicker when tested (see stage III in Figure 6.11). However, the understanding of how duration affects the performance of the two backfill systems is not well established, yet it could be considered for future research. Lastly, at the post-peak stage, it is evident that layered backfill reaches the post-peak stage faster than non-layered backfill. Thus, layered backfill is more prone to failure than non-layered backfill support system.

## 6.5 Conclusion and future outlook

The numerical simulations presented in this chapter provided a detailed analysis of the stress distribution and interaction between the backfill and the rock mass. Additionally, the change in the strength of the slope as the backfill layers increase has been demonstrated. The numerical simulation results reveal that upon the first layer of backfilling, the stress within the slope is transferred to the backfill.

Furthermore, the load is distributed to the lower layers as backfilling continues. Now, in terms of the effectiveness of the backfill; the principal stress is reduced by 95.6% when the stope is completely backfilled. When considering the effect of layering, the stress increases from 0.132 MPa for a non-layered backfill to 0.134 MPa, 0.141 MPa and 0.234 MPa, as the layers increase to four. That is a percentage increase of 1.51%, 6.81%, and 77.27%, respectively. The relationship between the compressive strain and layering is not that significant, with the highest increase of at most 15% in four-layered backfill. Although the most strained portion is the upper and middle layers of the backfill, the bottom layer remains unaffected. Similarly, the displacement of the stope is also very minimal. Lastly, the shear dissipation is visible at the rock-fill interface for all types of backfilling strategies except for the three-layered backfill. The cause of this discrepancy is still unknown.

It is worth noting that this modelling process is not time-dependent, i.e., it does not consider the 24-h backfilling period as practised in the industry. It is assumed in this modelling procedure that the backfill is drained and fully cured during the simulation process. Additionally, the simulated stope is assumed to be a 'blind stope', i.e., there is no access to fill from the top. Therefore, the stope is tight-filled, and no gap is left in the model to simulate the poor hanging rock-fill contact. These factors may be considered for future research endeavours.

Chapter 7 discusses the procedure followed to develop an analytical solution to assess the stability of exposed layered backfilled stope.

## Chapter 7 Development of an analytical solution to assess the stability of exposed vertical layered backfill.

### 7.1 Introduction

This chapter proposes a solution to assess the stability of backfill stopes with consideration of the effect of layering. When it is required that pillars must be left as primary support, production loss is incurred since the pillars are part of the orebody. Thus, the use of backfill support significantly improves the ore recovery rate. When a mine stope is extracted, the void is filled before mining the secondary stope. Therefore, the man-made pillar (backfilled stope) must have a minimum strength to remain stable when mining the adjacent secondary stope. Hence, it is of paramount importance to assess the stability of the backfilled stope to determine its stability during the extraction of the recently blasted stope and cause dilution. As discussed in Chapter 2, the first analytical solution was proposed by Mitchell et al. (1982) based on limit equilibrium analysis. Since then, the Mitchell solution is widely accepted and has been applied to determine the required strength of CTB, leading to a reduction in cement consumption in the mining industry.

Li and Aubertin (2012) reviewed and modified the solution proposed by Mitchell et al. (1982) to overcome some limitations of the original solution. One of the limitations was that the solution could not be applied to both high and low height-to-width aspect ratios. Then, Li (2014b) developed an improved solution to address the limitations imposed by Mitchell's solution. Li (2014b) solution considered the shear strength contributed by the friction along the backfill-rock mass interfaces. For example, Li and Aubertin (2014) proposed another solution that incorporates friction and cohesion along the potential sliding planes. Furthermore, the shearing along the interfaces between the backfill and rock walls is also considered. Another solution that overcomes the solutions of the authors considers the effect of effective friction angle and Poisson's ratio (Yang et al., 2017). Yang et al. (2017) considers the tension cracks within the backfill support.

The stability analysis of stratified backfill has rarely been done. Although, there is evidence of shearing that occurs along the interfaces between the rock mass and the backfill (Li and Aubertin, 2014), and also the backfill layers. The main objective

of this chapter is to develop a solution to assess the stability of stratified backfill body. To achieve the objective of the study, this study developed a solution to estimate the safety factor of stratified CTB. The solution was developed by relooking at Mitchell et al. (1982) and Li and Aubertin (2012) (MM's) existing solutions. These solutions were improved by incorporating the effect of layering through the inclusion of shear force due to the backfill layers. Moreover, the friction force that resist the sliding of the wedge block according to Newton second law is considered. The CTB material is considered to obey Mohr's Coulomb criterion, therefore, the cohesion and friction angle of the CTB material are the main parameters of the solution.

## 7.2 Development of the proposed solution

Figure 7.1 illustrates the forces acting upon the backfill pillar. The upper block is submitted to a surcharge,  $p_0$  which is the corresponding pressure due to the surcharge), shear ( $S_s$ ) forces along the interfaces between the backfill and side walls, and shear force ( $S_b$ ) along the interface between the backfill layers. The force  $P_1$  is the corresponding pressure at the boundary between the upper and lower blocks), which supports the base of the upper block, and constitutes a surcharge for the lower wedge.

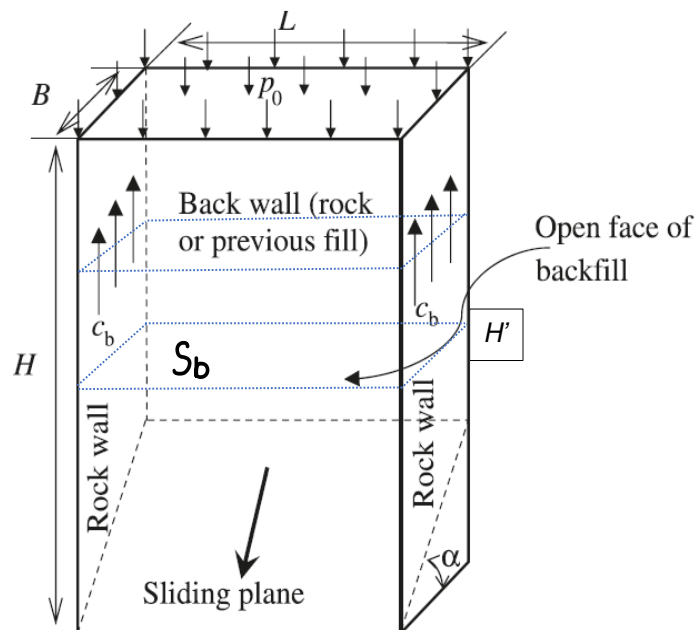


Figure 7.1 Decomposition of the forces acting on the layered backfill model (adapted from Li, 2014)



The following assumptions are made in this study:

- The stope is high but narrow and multiple backfilling strategies are considered in the block model.
- The shear stress along the interfaces between backfill and the backwall is ignored.
- Both cohesion and friction contribute to the shear resistance along the interface of the backfill-rockmass sidewall. The interface cohesion (adherence) between the backfill and the side walls,  $c_b$ , is also expressed as a ratio of the backfill cohesion,  $c$  (Li and Aubertin, 2014):

The backfill body is considered to obey the Mohr-Coulomb criterion. Therefore, the shear strength acting along the sidewalls and back walls is characterised by:

$$\tau_s = c_s + \sigma_h \tan \delta \quad (7.1)$$

$$c_b = r_b c \quad (7.2)$$

where  $r_b$  is a parameter for the interface cohesion between the backfill and the side walls ( $0 \leq r_b \leq 1$ ). Furthermore, the horizontal stress  $\sigma_h$  acting on the sidewalls at a certain depth  $h$  is obtained through Equation (7.3).

$$\sigma_h = \frac{\gamma L}{2 \tan \delta} \left[ 1 - \exp \left( -2 K \tan \delta \frac{h}{L} \right) \right] + K p_0 \exp \left( -2 K \tan \delta \frac{h}{L} \right) \quad (7.3)$$

Where  $\gamma$  is the unit weight of backfill;  $K = (1 - \sin \phi) / (1 + \sin \phi)$  is Rankine's active pressure coefficient;  $\delta$  is the friction angle of the rock mass; and  $\phi$  is the friction angle of backfill (Yang et al., 2017).

The shear forces  $S_s$  as a result of shear strength along the sidewalls can be estimated as follows:

$$\begin{aligned} S_s = \int_0^{H'} \tau_s B dh + \int_1^H \tau_s \frac{H-h}{\tan \alpha} dh = B \left( r_b c + \frac{\gamma L}{2} \right) \left( H - \frac{B \tan \alpha}{2} \right) - \frac{BL}{2} \left( \frac{\gamma L}{2K \tan \delta} - P_0 \right) \\ + \frac{L^2}{4K \tan \delta \tan \alpha} \left( \frac{\gamma L}{2k \tan \delta} - p_0 \right) \left[ \exp \left( -\frac{2K \tan \delta}{L} H' \right) - \exp \left( -\frac{2K \tan \delta}{L} H \right) \right] \quad (7.4) \end{aligned}$$

Where  $H'$  equates to  $H - B \tan \alpha$  and  $P_0$  denotes the pressure endured by the backfill body due to equipment of newly deposited backfill.

Note that in Equation (7.4), the shear force  $S_a$  due to the shear strength along the backfill-back wall interface being ignored. And in order to incorporate the shear

force due to the shear strength along the interface between the backfill layers,  $S_b$ , the following equation is used:

$$s_b = c + \sigma_h \tan \phi \quad (7.5)$$

The weight of the wedge block above the sliding plane (backfill),  $W$  is expressed as:

$$W = \gamma B L H' \quad (7.6)$$

Now, the net weight  $W_n$  of the sliding wedge block is given as

$$W_n = P_0 + W - 2S_s - nS_b \quad (7.7)$$

Where  $n$  is the coefficient corresponding to the number of layers that are associated with the shear force  $S_b$  along the backfill interfaces. For example, if the backfill material is a four-layered structure, thus,  $n$  will be 3 since there are now three interfaces between the backfill layers. Similarly, the factor 2 before  $S_s$  in Equation (7.7) denotes the two interfaces between the backfill and the two sidewalls.

According to Newton's second law, there is also a force that is resisting the sliding of the wedge block called force of kinetic friction,  $F_k$ . The force of kinetic friction can be estimated as (Kelemenová et al., 2020):

$$F_k = \mu W \cos \alpha \quad (7.8)$$

Where  $\mu$  is the coefficient of kinetic friction and is written as:

$$\mu = \frac{W \sin \alpha}{W \cos \alpha} \quad (7.9)$$

When Equation (7.9) is substituted to Equation (7.8), the kinetic friction is now reduced to:

$$F_k = W \sin \alpha \quad (7.10)$$

When replacing the relevant terms by their corresponding expression, the factor of safety ( $FoS$ ) of the sliding wedge block is therefore expressed as:

$$FoS = \frac{\text{Resisting forces}}{\text{Driving forces}}$$

$$FoS = \frac{\tan \phi}{\tan \alpha} + \frac{2CBL + F_k}{\sin 2\alpha [P_0 + W - 2S_s - nS_b]} \quad (7.11)$$

The required backfill cohesion is then expressed as follows:

$$c = \frac{(S_b + P_0 + \gamma H')/2}{[FS - \tan \phi / \tan \alpha] \sin 2\alpha}^{-1} + r_b H' / L \quad (7.12)$$

### 7.3 Validation of analytical solution

Sample applications of the proposed solution (Equation 7.11) are presented. Results obtained by the application of the original solution by Mitchell et al. (1982) and the modified Mitchell's solution by Li and Aubertin (2012) are also plotted for comparison. Figure 7.2 illustrates the variation of FoS when the slope height  $H = 40$  m,  $B = 10$  m,  $L = 10$  m,  $\gamma = 18$  kN/m<sup>3</sup>,  $\phi = \delta = 30^\circ$  and  $r_b = r_s = 0.5$  for different values of  $P_0$ . The results show that as the surcharge overload increase, the factor of safety of the backfilled decreases. The solution by Mitchell et al (1982) seems to be constant throughout because the solution neglects the effect of the surcharge in the equation. This causes the solution to be non-conservative when additional pressure is applied on top of the backfill, which is inevitable in underground mining. Therefore, for large stopes where the backfill height exceeds the exposed face, the possibility of failure is high (Li and Aubertin, 2012; Wang et al. 2021). Thus, the solution by Mitchell et al. (1982) may result in the overestimation of the stability index of the stope with dire consequences.

Figure 7.2 demonstrates the stability of the backfill when the surcharge increases, and the proposed solution predicts a dwindling safety factor as the surcharge pressure increases. Similar findings are reported by Li (2014b) who developed an analytical solution to evaluate the stability of backfill with a plug pour. These results are also corroborated by Li and Aubertin (2009), their study assessed the normal stress along the horizontal and vertical axes of backfilled stopes with the effect of a surface load on the fill. Li and Aubertin (2009) report an increase of the vertical stress in the backfill stope as the surface load increases.

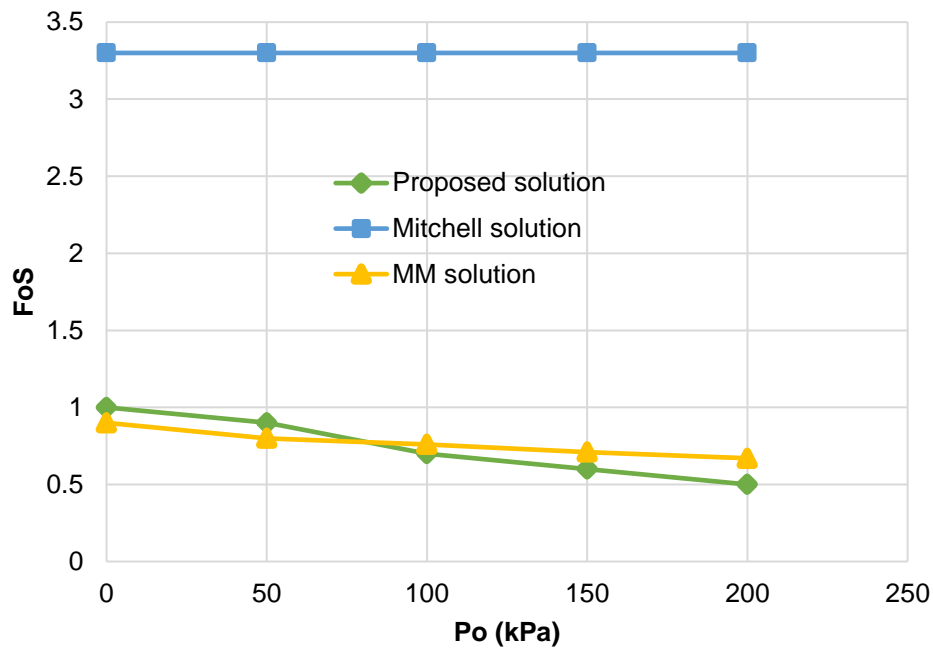


Figure 7.2 Variation of safety factor with overload pressure. Calculations done with  $c = 80$  kPa,  $H = 40$  m,  $L = 10$  m  $\gamma = 18$  kPa,  $r_s = 0.5$ .

The effect of stope height is illustrated in Figure 7.3, as can be seen, the stability of the backfill deteriorates with increasing stope height. The Mitchell et al (1982) solution tends to overestimate the safety factor as compared to the MM's solution and the proposed solution. Nasir and Fall (2010) and Yilmaz (2018) reported an increase in the strength of CTB with increasing stope size, however, these findings are based on the undrained behaviour of CTB at an early age. Indeed, binder hydration plays a major role in the strength development of CTB at an early age. The precipitation of hydration products is reported to result in the refinement of the pore structure of CTB, which reduces its porosity and consequently improves the strength of CTB with curing time (Du et al., 2021; Hou et al., 2022). Nonetheless, the proposed solution of this study and the other authors (e.g. Li, 2012; Li and Aubertin, 2012; Mitchell et al., 1982) applies to fully drain CTB structure. The findings of this study are supported by Jahanbakhshzadeh et al. (2017), whose study entails the development of an analytical solution to characterize the stress state within an inclined backfilled stope. Their study shows that both the vertical and horizontal stresses within the stope increase with the stope height. The increase in stope height results in more backfill layers being added. This is because when the stope height increases during ore extraction, backfilling occurs to stabilise the stope. Thus, increasing the pressure on the existing layers, consequently diminishing the stability of the backfill structure. Similar findings were

reported by Pirapakaran and Sivakugan (2006) that vertical stress within the backfill slope increases with the stope height.

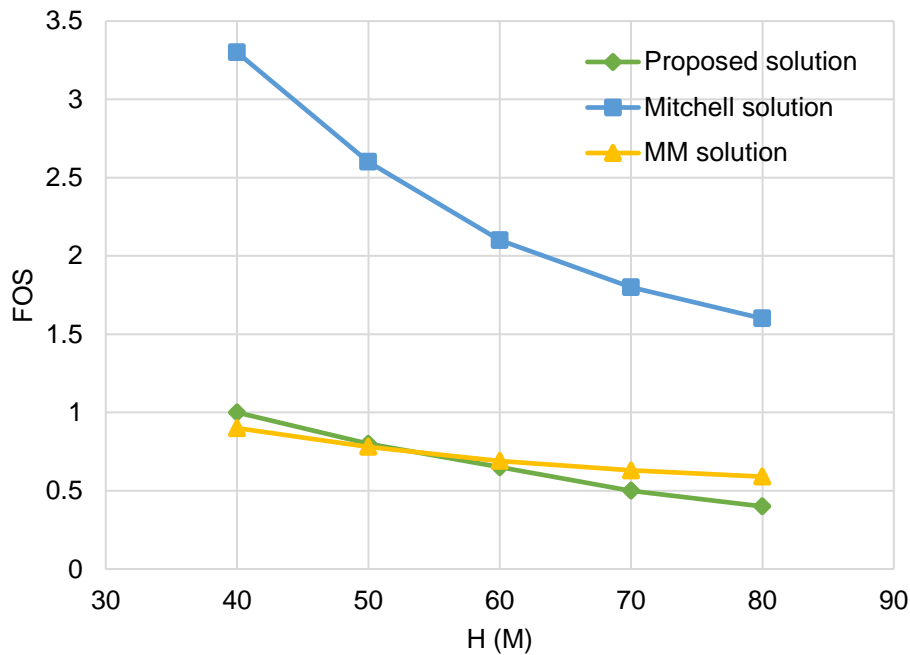


Figure 7.3 Variation of safety factor with stope height. Calculations done with  $c = 80 \text{ kPa}$ ,  $L = 10 \text{ m}$ ,  $\gamma = 18 \text{ kPa}$ ,  $r_s = 0.5$ .

Figure 7.4 shows the impact of stope length  $L$  on the safety factor of the backfill. Seemingly, the safety factor of the backfill decreases when the stope becomes longer. Thus, the value of the safety factor is sensitive to a variation in the size of the exposed backfill face. Similar findings were reported by Li and Aubertin (2012) through the MM's solution. The MM solution also predicts a declining safety factor as the length of the stope increases. However, Li and Aubertin (2012) only restricted the length of the stope to 12 m because the solution is for high aspect ratios which are similar to the proposed solution of this study. This study went as far as 30 m because there was a very slight change in the safety factor with less than 20 m. For example, at 10 m, the safety factor is 1.0 then at 20 m, the safety factor is 1.1. Therefore, since this solution is for narrow stopes, the value of the safety factor may be unrealistic as the stope widens.

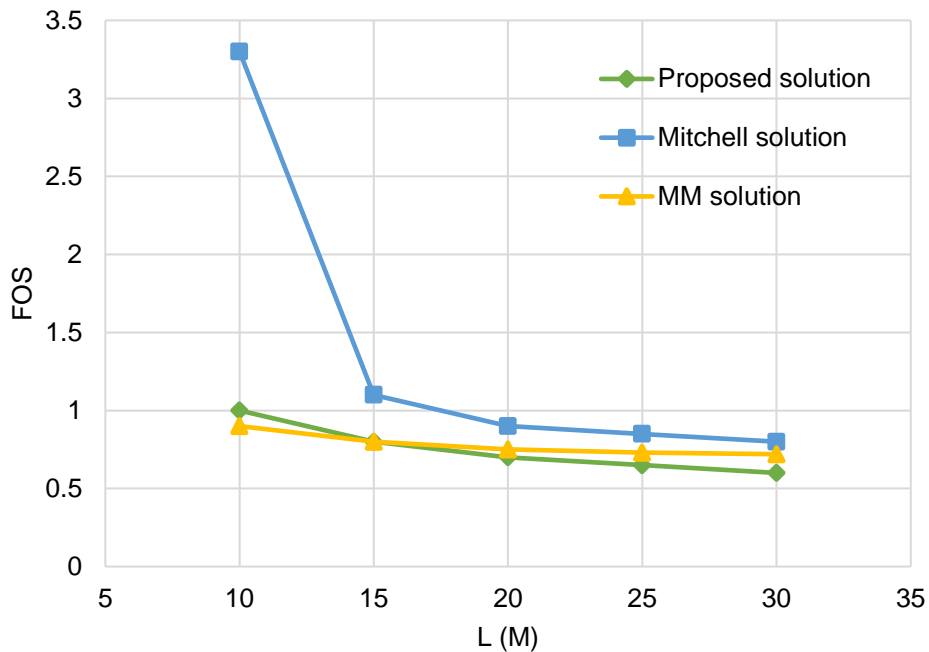


Figure 7.4 Variation of FoS with different values of stope length

The evolution of the value of the safety factor with the influence of the adherence ratio  $r_s$  is illustrated in Figure 7.5. The adherence ratio is positively correlated with the safety factor, i.e., the stability of the backfill increases nonlinearly with the adherence ratio. This is because an increase in the adherence ratio increases the roughness and cohesion of the rock mass. The findings by Li and Aubertin (2014) and Yang et al. (2017) also reveal that the stability of backfill increases with the adherence ratio. In support of the above analysis, Koupouli et al. (2016) add that the stiffness of the CTB-rock interface is higher than that of the CTB-CTB interfaces at high normal stress levels. Belem et al. (2000) also attest that an increased cohesion increases the strength of CTB.

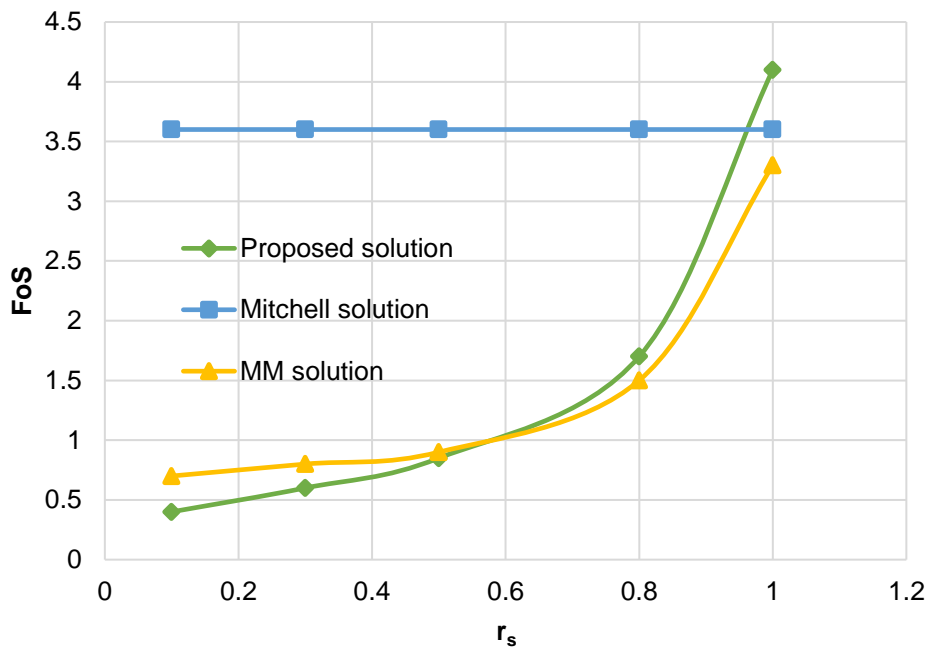


Figure 7.5 Variation of safety factor with different values of adherence ratio  $r_s$ . Calculations done with  $c = 80$  kPa,  $H = 40$  m,  $\gamma = 18$  kPa,  $r_s = 0.5$ ,  $\phi = \delta = 30^\circ$ .

Figure 7.6 depicts the effect of layering on the stability of the backfill stope. Backfilling in layers becomes necessary in large stopes to minimise the pressure on the barricade. The common practice in the mining industry is a 24-hour gap of filling each layer (Fu et al., 2020; Wang et al., 2020c; Zhang et al., 2022). Thus, the layering on the backfill structure becomes visible. Furthermore, Koupouli et al. (2016) posit that shear stress is higher for CTB-CTB interfaces compared with CTB-rock interfaces, thus, the significance of studying its effect. So far, the documented analytical solutions to assess the stability of exposed backfill do not incorporate the effect of shearing along the interfaces of the CTB-CTB layers. Therefore, the solution proposed in this study predicts the stability of a backfill stope considering the layering effect.

As can also be seen in Figure 7.6, the safety factor of the backfill decrease as more layers add added to the solution. However, the safety does not always decline with increasing layers, eventually, the graph becomes constant. Qi et al. (2022) simulated the stress distribution in a backfilled layered stope. Their findings indicate that the stress within the stope increases with the number of layers. Similarly, Chen et al. (2022) and Xu et al. (2019), in the experimental studies of the mechanical properties of CTB, found that the strength of CTB decreases with an increasing number of layers.

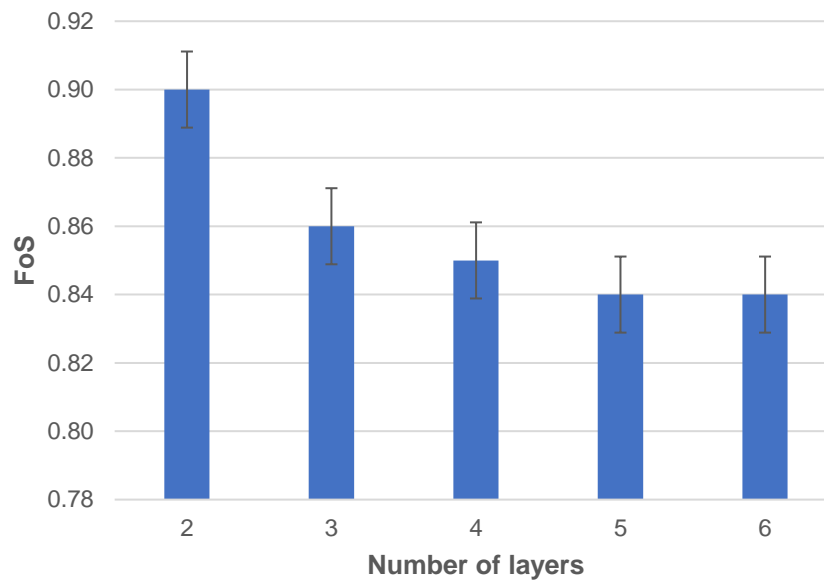


Figure 7.6 Variation of safety factor with the number of layers. Calculations done with  $c = 80$  kPa,  $H = 40$  m,  $\gamma = 18$  kPa,  $r_s = 0.5$ .

Based on the findings presented above, the effect of layering on the stability of backfill cannot be ignored. Depending on the size of the orebody, mining large stopes imposes the need for backfilling layer by layer. It is also evident that increasing stope height has a negative impact on the safety factor of backfill. Thus, the inclusion of the shearing force along the backfill layers interface cannot be further emphasised. It is worth noting that the properties of backfill also are beyond the control of men, for example, the properties of tailings depend on the rock mass and orebody characteristics. This makes the prediction of the stability of backfill a complex exercise as there are many factors involved. Therefore, the use of the solution may provide different results for a mining stope in a highly stressed environment or moderately stressed environment. Furthermore, the consumption of more cement may arise depending on the unique condition of that mine. Overall, industry workers can only work with what they have and use it to their advantage.

#### 7.4 Final remarks

The study of the interaction between the CTB-rock and CTB-CTB interfaces is a complex concept. Therefore, simple assumptions are adopted to develop solutions to study such relations. Several assumptions made in this study were adopted from the solutions developed by previous well-established authors such as Mitchell et al. (1982) and Li and Aubertin (2012). However, the common limitation with all the



other documented solutions is the inconsideration of the shear stress along the CTB-CTB layers interface. Even when literature reveals that the shear stress between the CTB-CTB is higher in a high-stress environment such as underground mining. The well-known solution by Mitchell et al. (1982) and the MM solution overestimate the stability of backfill. Although the overestimation of the safety factor of backfill may reduce cement consumption costs, it will, however, result in an improper design of the backfill and compromise the safety of mine workers. Another implication of the failure of the backfill pillar is the dilution of the blasted ore and loss of production targets. Since the strategy of backfilling in layers cannot be avoided, it is, therefore, necessary for the mining industry to have a solution that will cater for its needs. Another aspect that should be considered to further improve the existing solutions is the seepage of water through the backfill layers that may have the potential to disintegrate the backfill structure gradually until the deformation of the fill. Therefore, a long-term seepage effect must be considered for future research endeavours.

## Chapter 8 Conclusions and recommendations

The main objective of this doctoral study was to assess the effect of layering on the stability of backfill support system. Experimental methods and numerical analysis were used for the purpose. This chapter summarises the findings of the thesis, the conclusion, and recommendations for future research.

### 8.1 Summary of the thesis

There are several methods and solutions documented in the literature that can be used to evaluate the stability of backfill. Some apply to backfill support in general without special consideration of the mine layout or stope geometry. However, when the latter is considered, it often comes with the need to analyse the effect of the external surroundings on the strength of the backfill. Indeed, backfilling strategies vary with the type of mining layout/method. As such, a one-size-fit-all solution to backfill behaviour would inevitably be limited in terms of prediction ability. The output also may be deemed conservative to assess support systems unique to every mine layout. In the case of large stopes, backfilling the excavation at once is always almost impossible. Instead, layer-by-layer backfilling is preferred with the number of layers of the backfill system increasing as stope height increases. The stratification is expected to affect the mechanical properties and failure mode of backfill support differently. This is what the present doctoral study attempted to explore with the aim of developing an analytical solution to the behaviour of layered backfill support and an associated damage model.

To achieve this, experimental tests were conducted on a gold-mine tailings material for plasticity, chemical composition, and particle size distribution. Cemented tailings backfill (CTB) specimens were then prepared as one-, two-, and three-layered cubes. The various CTB specimens were cured and tested for compressive strength. The findings revealed that the strength of CTB decreases with an increasing number of layers of backfill. The damage of the layered CTB became significant with increased layers, a further emphasis on the negative effect of layering. The modelled factor of safety (FoS) of the backfilled stope also increases when the effect of layering was considered. On the other hand, the

estimated FoS decreased as the stope height increased. The subsections below provide a summary of the key findings.

### *8.1.1 Laboratory experiments*

Atterberg's tests were done on samples of the tailings material to determine its plasticity. Based on the values of Atterberg's limits obtained, the tailings batch was classified as a low plastic clay material. This information was later used to set the constitutive model (elastoplastic model) behind the numerical simulation work done in this doctoral study.

In terms of particle size analysis, results showed that the tailings material used is well-graded for use in the preparation of CTB. The tailings material was also found to have high contents of quartz, lime, and aluminium oxide. Quartz is known to increase the viscosity of CTB paste and impart great loading capacity. As such, the tailings stockpile can potentially be reclaimed and be used for backfilling.

Finally, in terms of the UCS tests, results revealed that the strength of CTB samples increases with curing period and cement content, regardless of the number of layers. Growth in strength was significant at early age due to higher production of hydration products and probably high quartz content in the tailings. Higher cement content also increased the rate of production of hydration products; and consequently, the strength of cubes. Non-layered samples exhibited higher strength than their two- and three-layered counterparts. Lastly, the two-layered samples consistently displayed higher strain and greater damage at failure.

### *8.1.2 Numerical modelling*

The numerical analysis was performed using the OPTUM G3 software. The simulations were run from single-layered to four-layered backfilled stopes. The analysis revealed that the stress in the backfilled stope increases with the number of layers. The stress in the simulated stope increased by more than 77% when the number of layers was increased from one to four. The stress-strain curves developed from the simulations indicates an elastic-plastic behaviour of the backfill. The stress-strain curves of the simulated stopes showed evidence of the fact that the layered stopes quickly migrated from the elastic stage into the peak-stress region. In turn, the peak-stress region of simulated stopes increased with

the number of layers. Another note is that the layered slope developed a cyclic loading and unloading behaviour due to the number of layers. In other words, the deformation of the backfill is likely to occur at the top and middle layers of the backfill while the stress distribution within the bottom layer is unaffected. Thus, making the mechanical behaviour of backfill layered slopes a bit complex to describe than the typical ones. Just like the experimental results, the numerical analysis showed that the strength of cemented backfill decreases with increasing backfill layers. Thus, the numerical results were successfully correlated with the experimental results.

### *8.1.3 Development of a damage model*

The damage model developed in this study is based on the constitutive damage theory. A set of regression models were produced from the experimental results and used to derive the input parameters of the proposed damage model.

The damage model showed that the strength of CTB decreases when the layering of backfill increases. On the other hand, the deformation of the CTB increased with increasing backfill layers. In a sense, the effect of layering on the stability of the CTB structure was captured by this model. Most importantly, the damage model was successfully validated against the experimental results with errors less than 5% for all curing days. Therefore, until an improved damage model is available, the proposed can be used to characterize the mechanical properties of CTB. The damage model is also limited to a range of boundaries, i.e., the model can only be applied to backfill samples cured between 7 to 28 days and a maximum of three layers of backfill. Due to limited data points, additional laboratory tests are required to improve the model. The challenge met in this study was lack of financial resources to perform the laboratory work in a well-advanced laboratory with sufficient equipment.

### *8.1.4 Analytical solution for vertical exposed backfilled slope*

The analytical solution for vertical exposed backfilled slopes developed by Mitchell et al. (1982) is generally considered to be limited in scope. For example, the solution cannot be applied to low and wide slopes. The solution also considers the cohesion along the interfaces between the backfill and rock mass to be equal. It

finally does not incorporate the shear strength along the backwall, sidewalls, and backfill interfaces. Some of these limitations were addressed elsewhere by including the surcharge pressure and the shear strength along the interfaces between the backfill and sidewalls (see Li and Aubertin, 2012; Li, 2014; and Li and Aubertin, 2014). Yang et al. (2017) further improved the solution by incorporating the tension cracks formed in the exposed face of the backfilled stope. However, their proposed solutions, if used to assess the stability of layered backfill, would underestimate the FoS of the stope. This study also looked at the problem and developed a solution that incorporates the shear strength along the layers of the backfill body. The findings from the proposed solution are summarised as follows:

- the stability of the layered backfill is lower compared to the non-layered backfill. Additionally, the stability of layered backfill deteriorates with increasing backfill layers.
- The stability of the backfill decreases with increasing height. Whereas an increase in the stope height means more layers. Therefore, the stability of the backfill is further compromised.
- The stability of the backfill declines with increasing overload pressure, which is unavoidable in underground mining.

The proposed solution also has its own limitations, that is, it can only be applied to high and narrow stopes. The shear force between the backfill and sidewalls is ignored. Lastly, the solution ignores several intrinsic and extrinsic factors that affects the behaviour of backfill such as the properties of the tailings, chemical composition of the mixing water, environmental conditions and other internal factors.

## 8.2 Conclusion of the thesis

The main objective of this study was to evaluate the effect of layering on the stability of large, backfilled stopes. Laboratory experiments, numerical analysis and mathematical modelling were relied on to achieve this objective. An analytical model for the strength of a backfill was developed and shown to be sensitive to the number of backfill layers. This solution can also be used to estimate the safety factor of stratified CTBs. A numerical model was also explored which enabled to

gain insights into stress distribution within a stratified backfilled stope. Finally, a damage model was developed for the prediction of the strength of backfill in large open stopes. And although, the strength of the CTB body was seen to increase with the number of layers, there is still a lot of development required as part of future endeavours.

### 8.3 Recommendations for future work

Based on the scope of the work covered in this thesis, the following research ideas are recommended for future studies:

- The macroscopic study of the transfer of heat from the surrounding rock mass to the stope and vice versa, between the backfill layers as well as in the rock mass-stope-backfill system.
- The inclusion into the analytical solution of internal factors that affect the strength of CTB. This would address the current limitations of this study.
- The use of neuro-fuzzy system to develop improved solutions capable of assessing the stability of backfilled stopes.
- The development of advanced numerical simulations of backfill support from which stability charts can be produced that may predict the waiting time required before the extraction of the adjacent stope.
- The development of an analytical solution to assess the stability of layered backfill with incorporation of the seepage of water, which may deteriorate the conditions of the backfill overtime.
- The development of a model that will provide guidance of the experiments suitable for the problem statement and successfully validate the model. A more advanced data analysis software is recommended for a better presentation of the results.

## List of references

Adoko, A. C., Vallejos, J., Trueman, R., 2020. Stability assessment of underground mine stopes subjected to stress relaxation. *Mining Technology: Transactions of the Institutions of Mining and Metallurgy*, vol. 129, no. 1, pp. 30 – 39

Akkaya, U.G., Cinku, K., Yilmaz, E., 2021. Characterization of strength and quality of cemented mine backfill made up of Lead-Zinc processing tailings. *Frontiers in Materials*, vol. 8, p. 740116

Al-Heib, M.M., Didier, C., Masrouri, F., 2010. Improving short- and long-term stability of underground gypsum mine using partial and total backfill. *Rock Mechanics and Rock Engineering*, vol. 43, pp. 447 – 461

ASTM D4318, 2010. Standard test methods for liquid limits, plastic limit, plasticity index of soils. American Society for Testing and Materials, West Conshohocken, PA

Atterberg, A., 1911. Die Plastizität der Tone. *Internationale Mitteilungen für Bodenkunde*, vol. 1, pp. 435 – 461

Balegh, B., Sellaf, H., Hadjmostefa, A., 2020. Effect of ceramic waste on mechanical and geotechnical properties of tuff treated by cement. *Case Studies in Construction Materials*, vol. 13, p. 00368

Belem, T., Aatar, O. E., Bussiere, B., Benzaazoua, M., 2016. Gravity-driven 1-D consolidation of cemented paste backfill in 3-m-high columns. *Innovative Infrastructure Solutions*, vol. 1., p. 37

Benzaazoua, M., Ouellet, J., Servant, S., Newman, P., Verburg, R., 1999. Cementitious backfill with high sulfur content Physical, chemical, and mineralogical characterization. *Cement and Concrete Research*, vol. 29, no. 5, pp. 719 – 725

Benzaazoua, M., Fall, M., Belem, T., 2004. A contribution to understanding the hardening process of cemented paste fill. *Minerals Engineering*, vol. 17, no. 2, pp. 141 – 152

Boger, D.V., 2012. Personal perspective on paste and thickened tailings: a decade on. *Mining Technology*, vol. 121, no. 1, pp. 29 – 36

- Brekailo, F., Pereira, E., Pereira, E., Farias, M.M., Medeiros-Junior, R.A., 2022. Red ceramic and concrete waste as replacement of Portland cement: Microstructure aspect of eco-mortar in external sulfate attack. *Cleaner Materials*, vol. 3, p. 100034
- Cao, S., Yilmaz, E., Song, W., 2018. Evaluation of viscosity, strength and microstructural properties of cemented tailings backfill. *Minerals*, vol. 8, no. 8, p. 352
- Celestin, J. C. H., Fall, M., 2009. Thermal conductivity of cemented paste backfill material and factors affecting it. *International Journal of Mining, Reclamation and Environment*, vol. 23, no. 4, pp. 274 – 290
- Chang, B., Du, C., Chu, X., Zhang, L., 2021. Study on the optimization of filling ratio and strength variation characteristics of cemented backfills containing fly ash. *Frontiers in Materials*, vol. 8, p. 764410
- Chen, L., Lin, D., 2009. Stabilization treatment of soft subgrade soil by sewage sludge ash and cement. *Journal of Hazardous Materials*, vol. 162, no. 1, pp. 321 – 327
- Chen, X., Shi, X., Zhou, J., Chen, Q., Li, E., Du, X., 2018. Compressive behavior and microstructural properties of tailings polypropylene fibre-reinforced cemented paste backfill. *Construction and Building Materials*, vol. 190, pp. 211 – 221
- Chen, X., Shi, X., Zhou, J., Du, X., Chen, Q., Qiu, X., 2019. Effect of overflow tailings properties on cemented paste backfill. *Journal of Environmental Management*, vol. 235, pp. 133 – 144
- Chen, X., Shi, X., Zhang, S., Chen, H., Zhou, J., Yu, Z., Huang, P., 2020. Fibre-reinforced cemented paste backfill: The effect of fibre on strength properties and estimation of strength using nonlinear models. *Materials*, vol. 13, no. 3, p. 718
- Chen, S., Jin, A., Zhao, Y., Li, H., Wang, J., 2022a. Mechanical properties and deformation mechanism of stratified cemented tailings backfill under unconfined compression. *Construction and Building Materials*, vol. 335, p. 127205
- Chen, X., Zhang, H., Wu, Y., Jiao, H., Yang, L., Wang, Q., Zhang, W., 2022b. Micro-mechanism of uniaxial compression damage of layered cemented backfill in underground mine. *Materials*, vol. 15, no. 14, p. 4846



- Cheng, H., Wu, S., Zhang, X., Wu, A., 2020a. Effect of particle gradation characteristics on yield stress of cemented paste backfill. *International Journal of Minerals, Metallurgy and Materials*, vol. 27, pp. 10 – 17
- Cheng, H., Wu, S., Li, H., Zhang, X., 2020b. Influence of time and temperature on rheology and flow performance of cemented paste backfill. *Construction and Building Materials*, vol. 231, p. 117117
- Cheng, K., Tu, B., Liu, L., Zhang, B., Qiu, H., 2021. Damage strengthening constitutive model of cemented paste backfill. *Advances in Civil Engineering*, vol. 2021, Article ID 5593983.
- Cihangir, F., Ercikdi, B., Kesimal, A., Turan, A., Deveci, H., 2012. Utilisation of alkali-activated blast furnace slag in paste backfill of high-sulphide mill tailings: Effect of binder type and dosage. *Minerals Engineering*, vol. 30, pp. 33 – 43
- Clark, L.M., Pakalnis, R.C., 1997. An empirical approach for estimating unplanned dilution from open stope hanging walls and footwalls. In: *Proceedings of the 99<sup>th</sup> Annual General Meeting*. Canadian Institute of Mining, Metallurgy and Petroleum CIM (CD-ROM), Vancouver, BC
- Craig, R.F., 2004. *Craig's Soil Mechanics*, 7<sup>th</sup> Edition. CRC Press, London
- Cui, L., Fall, M., 2016. An evolutive elasto-plastic model for cemented paste backfill. *Computers and Geotechnics*, vol. 71, pp. 19 – 29
- Cui, L., Fall, M., 2018. Multiphysics modeling and simulation of strength development and distribution in cemented tailings backfill structures. *International Journal of Concrete Structures and Materials*, vol. 12, p. 25
- Dalce, J.B., Li, L., Yang, Y., 2019. Experimental study of uniaxial compressive strength (UCS) distribution of hydraulic backfill associated with segregation. *Minerals*, vol. 9, no. 3, p. 147
- Ding, K., Ma, F., Guo, J., Zhao, H., Lu, R., Liu, F., 2018. Investigation of the mechanism of roof caving in the Jinchuan Nickel Mine, China. *Rock Mechanics and Rock Engineering*, vol. 51, pp. 1215 – 1226
- Dong, Q., Liang, B., Jia, L., Jiang, L., 2019. Effect of sulfide on the long-term strength of lead-zinc tailings cemented paste backfill. *Construction and Building Material*, vol. 200, pp. 436 – 446

Du, Z., Chen, S., Wang, S., Liu, R., Yao, D., Mitri, H. S., 2021. Influence of binder types and temperature on the mechanical properties and microstructure of cemented paste backfill. *Advances in Underground Mine backfill*, Article ID 6652176

Ercikdi, B., Cihangir, F., Kesimal, A., Deveci, H., 2017. Practical importance of tailings for cemented paste backfill. In: Yilmaz E., Bakir, C. (Eds.), pp. 7 – 32. *Mine Tailings Management*, Cham: Springer

Ercikdi, B., Kesimal, A., Cihangir, F., Deveci, H., Alp, I., 2009. Cemented paste backfill of sulphide-rich tailings: Importance of binder type and dosage. *Cement and Concrete Composites*, vol. 31, no. 4, pp. 268 – 274

Ercikdi, B., Cihangir, F., Kesimal, A., Deveci, H., Alp, I., 2010. Utilization of water-reducing admixtures in cemented paste backfill of sulphide-rich mill tailings. *Journal of Hazardous Materials*, vol. 179, no. 1 – 3, pp. 940 – 946

Fall, M., Benzaanzoua, M., Ouellet, S., 2005. Experimental characterization of the influence of tailings fineness and density on the quality of cemented paste backfill. *Minerals Engineering*, vol. 18, no. 1, pp 41 – 44

Fall, M., Belem, T., Samb, S., Benzaazoua, M., 2007. Experimental characterization of the stress-strain behaviour of cemented paste backfill in compression. *Journal of Material Science*, vol. 42, pp. 3914 – 3922

Fall, M., Benzaazoua, M., Saa, E.G., 2008. Mix proportioning of underground cemented tailings backfill. *Tunnelling and Underground Space Technology*, vol. 23, no. 1, pp. 80 – 90

Fall, M., Adrien, D., Celestin, J.C., Pokharel, M., Toure, M., 2009. Saturated hydraulic conductivity of cemented paste backfill, *Minerals Engineering*, vol. 22, no. 15, pp. 1307 – 1317

Fall, M., Samb, S.S., 2009. Effect of high temperature on strength and microstructural properties of cemented paste backfill. *Fire Safety Journal*, vol. 44, no. 4, pp. 642 – 651

Fall, M., Nasir, O., 2010. Mechanical behavior of the interface between cemented tailings backfill and retaining structures under shear loads. *Geotechnical and Geological Engineering*, vol. 28, no. 6, pp. 779 – 790

Fall, M., Celestin, J.C., Pokharel, M., Touré, M., 2010. A contribution to understanding the effects of curing temperature on the mechanical properties of mine cemented tailings backfill. *Engineering Geology*, vol. 114, no. 3 – 4, pp. 397 – 413

Fall, M., Pokharel, M., 2010. Coupled effects of sulphate and temperature on the strength development of cemented tailings backfills: Portland cement-paste backfill. *Cement and Concrete Composition*, vol. 32, no. 10, pp. 819 – 828

Fang, K., Fall, M., Cui, L., 2021. Development of Mode I and Mode II fracture toughness of cemented paste backfill: Experimental results of the effect of mix proportion, temperature and chemistry of the pore water. *Engineering Fracture Mechanics*, vol. 258, p. 108096

Feng, P., Garboczi, E., Miao, C., Bullard, J., 2015. Microstructural origins of cement paste degradation by external sulfate attack. *Construction and Building Materials*, vol. 96, 391 – 403

Fourie, A., Helinski, M., Fahey, M., Ismail, M., 2007. Assessment of the self-desiccation process in cemented mine backfills. *Canadian Geotechnical Journal*, vol. 44, no. 10, pp. 1148 – 1156

Festugato, L., Fourie, A., Consoli, N., 2013. Cyclic shear response of fibre-reinforced cemented paste backfill. *Géotechnique Letters*, vol. 3, no. 1, 5 – 12

Fu, J., Wang, J., Song, W., 2020. Damage constitutive model and strength criterion of cemented paste backfill based on layered effect considerations. *Journal of Materials Research and Technology*, vol. 9, no. 3, pp. 6073 – 6084

Gao, X., Liu, S., Zhao, C., Yin, J., Fan, K., 2022. Damage evolution characteristics of back-filling concrete in gob-side entry retaining subjected to cyclical loading. *Materials*, vol. 15, no. 16, p. 5772

Ghirian, A., Fall, M., 2014. Coupled thermos-hydro-mechanical-chemical behaviour of cemented paste backfill in column experiments. Part II: Mechanical, chemical and microstructural processes and characteristics. *Engineering Geology*, vol. 170, pp. 11 – 23

Ghirian, A., Fall, M., 2016. Strength evolution and deformation behaviour of cemented paste backfill at early ages: Effect of curing stress, filling strategy and

drainage. *International Journal of Mining Science and Technology*, vol. 26, no. 5, pp. 809 – 817

Gholami, R., Fakhari, N., 2017. Support vector machine: Principles, parameters, and applications. In: *Handbook of Neural Computation*, pp. 515 – 535, Elsevier

Ghoreishi-Madiseh, S.A., Hassani, F., Abbasy, F., 2015. Numerical and experimental study of geothermal heat extraction from backfilled mine stopes. *Applied Thermal Engineering*, vol. 90, pp. 1119 – 1130

Gielen, D., Boshell, F., Saygin, D., Bazilian, M.D., Wagner, N., Gorini, R., 2019. The role of renewable energy in the global energy transformation. *Energy Strategy Reviews*, vol. 24, pp. 38 – 50

Godugu, A.K., Sekhar, S., Porathur, J., Bhargava, S., 2021. Stability analysis and design of cemented backfill wall for underground hard-rock mines using numerical modelling. *Current Science*, vol. 121, no. 7, pp. 920 – 928

Gonzalez, A., Parraguez, A., Corvalan, L., Correa, N., Castro, J., Stuckrath, C., Gonzalez, M., 2020. Evaluation of Portland and Pozzolanic cement on the self-healing of mortars with calcium lactate and bacteria. *Construction and Building Materials*, vol. 257, p. 119558

Grabinsky, M., Bawden, W., Thompson, B., 2021. Required plug strength for continuously poured cemented paste backfill in longhole stopes. *Mining*, vol. 1, pp. 80 – 99

Guo, L., Chen, Q., Wu, Y., Zhang, Qi, C., 2022. Numerical simulation of adjacent stope interaction and parametric analysis of the creep behavior of rock mass. *Journal of Materials Research and Technology*, vol. 19, pp. 2063 – 2076

Hadjigeorgiou, J., Leclair, J., Potvin, Y., 1995. An update of the stability graph method for open stope design. 97<sup>th</sup> Annual General Meeting, Canadian Institute of Mining, Metallurgy and Petroleum (CIM), pp. 154 – 161, Halifax, Nova Scotia

Han, B., Zhang, S., Sun, W., 2019. Impact of temperature on the strength development of the tailing-waste rock backfill of a gold mine. *Advances in Civil Engineering*, vol. 2019, p. 4379606

- Hasanzadehshooili, H., Lakirouhani, A., Medzvieckas, J., 2012. Evaluating elastic-plastic behavior of rock materials using Hoek-Brown failure criterion. *Journal of Civil Engineering and Management*, vol. 18, no. 3, pp. 402 – 407
- Helinski, M., Fahey, M., Fourie, A., 2007. Numerical modelling of cemented mine backfill deposition. *Journal of Geotechnical and Geoenvironmental Engineering*, vol. 133, no. 10, pp. 1308 – 1319
- Henning, J.G., Mitri, S.H., 2007. Numerical modelling of ore dilution in blasthole stoping. *International Journal of Rock Mechanics and Mining Sciences*, vol. 44, no. 5, pp 692 – 703
- Hong, C.S., Shackelford, C.D., Malusis, M.A., 2012. Consolidation and hydraulic conductivity of Zeolite-amended soil-bentonite backfills. *Journal of Geotechnical and Geoenvironmental Engineering*, vol. 138, no. 1, pp. 15 – 25
- Hu, J., Zhao, F., Ren, Q., Kuang, Y., Zhou, T., Luo, Z., 2019. Microscopic characterization and strength characteristics of cemented backfill under different humidity curing conditions. *Royal Society Open Science*, vol. 6, no. 12, p. 191227
- Huang, Y., Wang, G., Rao, Y., Liu, W., 2021. Mechanical properties and damage mode of cemented tailings backfill in an acidic environment. *Journal of the Southern African Institute of Mining and Metallurgy*, vol. 121, no. 6, pp. 317 – 324
- Huynh, L., Beattie, D. A., Fornasiero, D., Ralston, J., 2006. Effect of polyphosphate and naphthalene sulfonate formaldehyde condensate on the rheological properties of dewatered tailings and cemented paste backfill. *Minerals Engineering*, vol. 19, no. 1, pp. 28 – 36
- Islam, S., 2021. A study on the mechanical behaviour of three different fine-grained mine tailings. *Journal of King Saud University – Engineering Sciences*, DOI: [10.1016/j.jksues.2021.04.001](https://doi.org/10.1016/j.jksues.2021.04.001)
- Jang, H., 2014. Unplanned dilution and ore-loss optimisation in underground mines via cooperative neuro-fuzzy network. PhD thesis, Curtin University, Australia
- Jahanbakhshzadeh, A., Aubertin, M., Li, L., 2018. Analysis of the stress distribution in inclined backfilled stopes using closed-form solutions and numerical simulations. *Geotechnical and Geological Engineering*, vol. 36, pp. 1011 – 1036

- Jaouhar, E.M., Li, L., 2019. Effect of drainage and consolidation on the pore water pressures and total stresses within backfilled stopes and on barricades. *Advances in Civil Engineering*, vol. 2019, p. 1802130
- Jiang, H., Fall, M., 2017. Yield stress and strength of saline cemented tailings in sub-zero environments: Portland cement paste backfill. *International Journal of Mineral Processing*, vol. 160, pp. 68 – 75
- Jiang, D., Li, X., Jiang, W., Li, C., Lv, Y., Zhou, Y., 2020a. Effect of tricalcium aluminate and sodium aluminate on thaumasite formation in cement paste. *Construction and Building Materials*, vol. 259, p. 119842
- Jiang, H., Han, J., Li, Y., Yilmaz, E., Sun, Q., Liu, J., 2020b. Relationship between ultrasonic pulse velocity and uniaxial compressive strength for cemented paste backfill with alkali – activated slag. *Nondestructive Testing and Evaluation*, vol. 35, no. 4, pp. 359 – 377
- Jiang, H., Yi, H., Yilmaz, E., Liu, S., Qiu, J., 2020c. Ultrasonic evaluation of strength properties of cemented paste backfill: Effects of mineral admixture and curing temperature. *Ultrasonics*, vol. 100, p. 105983
- Jones, M., 2018. Virgin rock temperatures and geothermal gradients in the Bushveld Complex. *Journal of the Southern African Institute of Mining and Metallurgy*, vol. 118, no. 7, pp. 671 – 680
- Kang, Z., Qing, W., Yajing, Y., Xiang, Y., Jungqiang, W, Shuai, C., 2019. Optimization calculation of stope structure parameters based on Mathew's stabilization graph method, *Journal of Vibroengineering*, vol. 21, no. 4, pp 1227 – 1239
- Kamiakin, V., 2017. Example problems related to soil identification and classification. In: *Soil Mechanics*, Kaliakin, V.N. (Eds.), Butterworth-Heinemann
- Kasap, T., Yilmaz, E., Sari, M., 2022. Physico-chemical and micro-structural behavior of cemented mine backfill: Effect of pH in dam tailings. *Journal of Environmental Management*, vol. 314, p. 115034
- Ke, X., Hou, H., Zhou, M., Wang, Y., Zhou, X., 2015. Effect of particle gradation on properties of fresh and hardened cemented paste backfill. *Construction and Building Materials*, vol. 96, pp. 378 – 382

- Ke, X., Zhou, X., Wang, X., Wang, T., Hou, H., Zhou, M., 2016. Effect of tailings fineness on the pore structure development of cemented paste backfill. *Construction and Building Materials*, vol. 126, pp. 345 – 350
- Kelemenova, T., Dovica, M., Bozek, P., Kolarikova, I., Benedik, O., Virgala, I., Prada, E., Mikova, L., Kot, T., Kelemen, M., 2020. Specific problems in measurement of coefficient of friction using variable incidence tribometer. *Symmetry*, vol. 12, no. 8, p. 1235
- Kesimal, A., Yilmaz, E., Ercikdi, B., 2004. Evaluation of paste backfill mixtures consisting of sulphide-rich mill tailings and varying cement contents. *Cement and Concrete Research*, vol. 34, no. 10, pp. 1817 – 1822
- Kesimal, A., Yilmaz, E., Ercikdi, B., Alp, I., Deveci, H., 2005. Effect of properties of tailings and binder on the short- and long-term strength and stability of cemented paste backfill. *Materials Letters*, vol. 59, no. 28, pp. 3703 – 3709
- Koupouli, N.J.F., Belem, T., Rivard, P., Effenguet, H., 2016. Direct shear tests on cemented paste backfill–rock wall and cemented paste backfill–backfill interfaces. *Journal of Rock Mechanics and Geotechnical Engineering*, vol. 8, no. 4, pp. 472 – 479
- Kok, S., Huat, B., Noorzaei, J., Jaafar, M.S., Gue, S., 2009. A review of basic soil constitutive models for geotechnical application. *Electronic Journal of Geotechnical Engineering*, vol 14, pp. 1 – 18
- Kwan, A., Ng, P., Huen, K., 2014. Effect of fines content on packing density of fine aggregate in concrete. *Construction and Building Materials*, vol. 61, pp. 270 – 277
- Labuz, J.F., Zang, A., 2012. Mohr–Coulomb failure criterion. *Rock Mechanics and Rock Engineering*, vol. 45, pp. 975 – 979
- Landriault, D., 2006. They said “It will never work” – 25 years of paste backfill 1981 – 2006. *Proceedings of 9th International Seminar on Paste and Thickened Tailings*, pp. 277 – 292, Limerick, Ireland
- Lang, L., Song, K., Lao, D., Kwon, T., 2015. Rheological properties of cemented tailing backfill and the construction of a prediction model. *Materials*, vol. 8, pp. 2076 – 2092

- Lemaitre, J., 1984. How to use damage mechanics. *Nuclear Engineering and Design*, vol. 80, no. 2, pp. 233 – 245
- Lemos, M., Valente, T., Reis, P., Fonseca, R., Delbem, I., Ventura, J., Magalhaes, M., 2021. Mineralogical and geochemical characterization of gold mining tailings and their potential to generate acid mine drainage (Minas Gerais, Brazil). *Minerals*, vol. 11, no. 1, p. 39
- Li, B., Zhang, J., Yan, H., Zhou, N., Li, M., 2022. Experimental investigation into the thermal conductivity of gangue-cemented paste backfill in mine application. *Journal of Materials Research and Technology*, vol. 16, pp. 1792 – 1802
- Li, L., 2014a. Generalized solution for mining backfill design. *International Journal of Geomechanics*, vol. 14, no. 3, DOI: [10.1061/\(ASCE\)GM.1943-5622.0000329](https://doi.org/10.1061/(ASCE)GM.1943-5622.0000329)
- Li, L., 2014b. Analytical solution for determining the required strength of a side-exposed mine backfill containing a plug. *Canadian Geotechnical Journal*, vol. 51, pp. 508 – 519
- Li, L., Aubertin, M., 2009. A three-dimensional analysis of the total and effective stresses in submerged backfilled stopes. *Geotechnical and Geological Engineering*, vol. 27, no.4, pp. 559 – 569
- Li, L., Aubertin, M., 2012. A modified solution to assess the required strength of exposed backfill in mine stopes. *Canadian Geotechnical Journal*, vol. 49, no. 8, pp. 994 – 1002
- Li, L., Aubertin, M., 2014. An improved method to assess the required strength of cemented backfill in underground stopes with an open face. *International Journal of Mining Science and Technology*, vol. 24, pp. 549 – 558
- Li, L., Aubertin, M., Belem, T., 2005. Formulation of a three-dimensional analytical solution to evaluate stress in backfilled vertical narrow openings. *Canadian Geotechnical Journal*, vol. 42, no. 6, pp. 1705 – 1717
- Li, W., Fall, M., 2016. Sulphate effect on the early age strength and self-desiccation of cemented paste backfill. *Construction and Building Materials*, vol. 106, pp. 296 – 304



- Li, J., Yilmaz, E., Cao, S., 2020. Influence of solid content, cement/tailings ratio, and curing time on rheology and strength of cemented tailings backfill. *Minerals*, vol. 922, no. 10, p. 922
- Libos, I.L.S., Cui, L., 2020. Effects of curing time, cement content, and saturation state on mode-I fracture toughness of cemented paste backfill. *Engineering Fracture Mechanics*, vol. 235, p. 107174
- Libos, I.L.S., Cui, L., 2021. Time- and temperature-dependence of compressive and tensile behaviors of polypropylene fiber-reinforced cemented paste backfill. *Frontiers of Structural and Civil Engineering*, vol. 15, pp. 1025 - 1037.
- Liu, G., Li, L., Yang, X., Guo, L., 2016a. Stability analyses of vertically exposed cemented backfill: A revisit to Mitchell's physical model tests. *International Journal of Mining Science and Technology*, vol. 26, no. 6, pp. 1135 – 1144
- Liu, X.S., Ning, J.G., Tan, Y.L., Gu, Q.H., 2016b. Damage constitutive model based on energy dissipation for intact rock subjected to cyclic loading. *International Journal of Rock Mechanics and Mining Sciences*, vol. 85, pp. 27 – 32
- Liu, L., Fang, Z., Qi, C., Zhang, B., Guo, L., Song, K., 2018. Experimental investigation on the relationship between pore characteristics and unconfined compressive strength of cemented paste backfill. *Construction and Building Materials*, vol. 179, pp. 244 – 264
- Liu, Q., Liu, D., Tian, Y., Liu, X., 2017. Numerical simulation of stress-strain behaviour of cemented paste backfill in triaxial compression. *Engineering Geology*, vol. 231, pp. 165 – 175
- Liu, S., Fall, M., 2022. Fresh and hardened properties of cemented paste backfill: Links to mixing time. *Construction and Building Materials*, vol. 324, p. 126688
- Liu, L., Xin, J., Huan, C., Qi, C., Zhou, W., Song, K., 2020. Pore and strength characteristics of cemented paste backfill using sulphide tailings: Effect of sulphur content. *Construction and Building Materials*, vol. 237, p. 117452
- Liu, L., Yang, P., Zhang, B., Huan, C., Guo, L., Yang, Q., Song, K., 2021. Study on hydration reaction and structure evolution of cemented paste backfill in early-age based on resistivity and hydration heat. *Construction and Building Materials*, vol. 272, p. 121827

- Mathews, K., Hoek, E., Wyllie, D., Stewart, S., 1981. Prediction of stable excavation spans at depths below 1000m in hard rock mines. CANMET Report, DSS Serial No. OSQ80–00081
- Mawdesley, C., Trueman, R., Whiten, W., 2001. Extending the Mathews stability graph for open-stope design. *Mining Technology*, vol. 110, no. 1, pp. 27 – 39
- Mitchell, R., Olsen, R., Smith, J., 1982. Model studies on cemented tailings used in mine backfill. *Canadian Geotechnical Journal*, vol. 19, no. 1, pp. 14 – 28
- Mozaffaridana, M., 2011. Using thermal profiles of cemented paste backfill to predict strength. Master's dissertation, University of Toronto, Canada
- Naguleswaran, N., 2018. Cemented paste backfill modification using different types of binders and insight into its mechanical, micro-structure, and flow properties. PhD dissertation, James Cook University, Australia
- Nasir, O., Fall, M., 2009. Modeling the heat development in hydrating CPB structures. *Computers and Geotechnics*, vol. 36, no. 7, pp. 1207 – 1218
- Nasir, O., Fall, M., 2010. Coupling binder hydration, temperature and compressive strength development of underground cemented paste backfill at early ages. *Tunnelling and Underground Space Technology*, vol. 25, pp. 9 – 20
- Newman, C.R., 2018. Numerical analysis of stress distributions for multiple backfilled stopes. PhD thesis, University of Kentucky, Lexington, Kentucky
- Nickson, S.D., 1992. Cable Support Guidelines for Underground Hard Rock Mine Operations. Master's Thesis, University of British Columbia, Vancouver, BC, Canada
- Niroshan, N., Sivakugan, N., Veenstra, R.L., 2018. Flow characteristics of cemented paste backfill. *Geotechnical and Geological Engineering*, vol. 36, pp. 2261 – 2272
- Ouattara, D., Yahia, A., Mbonimpa, M., Belem, T., 2017. Effects of superplasticizer on rheological properties of cemented paste backfills. *International Journal of Mineral Processing*, vol. 161, pp. 28 – 40
- Ouattara, D., Mbonimpa, M., Yahia, A., Belem, T., 2018. Assessment of rheological parameters of high density cemented paste backfill mixtures incorporating superplasticizers. *Construction and Building Materials*, vol. 190, pp. 294 – 307

- Pan, A.N., Murray, W.F., Grabinsky, L.G., 2021. Shear properties of cemented paste backfill under low confining stress. *Advances in Civil Engineering*, vol. 2021, p. 7561977
- Papaioanou, A., Sourineni, F.T., 2016. Development of a generalised dilution-based stability graph for open stope design. *Mining Technology*, vol. 125, no. 2, pp. 121 – 128
- Paterson, A.J.C., 2012. Pipeline transport of high-density slurries: a historical review of past mistakes, lessons learned and current technologies. *Mining Technology*, vol. 121, no. 1, pp. 37 – 45
- Peng, X., Guo, L., Liu, G., Yang, X., Chen, X., 2021. Experimental study on factors influencing the strength distribution of in situ cemented tailings backfill. *Metals*, vol. 11, p. 2059
- Potvin, Y., 1988. Empirical open stope design in Canada. PhD thesis, University of British Columbia
- Potvin, Y., Milne, D., 1992. Empirical cable bolt support design. *Proceedings of International Symposium on Rock Mechanics*, Sudbury, ON, Canada
- Potvin, Y., Hadjigeorgiou, J., 2001. The stability graph method for open-stope design. In: *Underground Mining Methods: Engineering Fundamentals and International Case Studies*. Hustrulid, W.A. and Bullock, R.L. (Eds.), pp. 513 – 520, Society of Mining, Metallurgy, and Exploration, 8307 Shaffer Parkway, Littleton
- Qi, C., Chen, Q., Fourie, A., Zhang, Q., 2018. An intelligent modelling framework for mechanical properties of cemented paste backfill, *Minerals Engineering*, vol. 123, pp. 16 – 27
- Qi, C., Fourie, A., 2019. Cemented paste backfill for mineral tailings management: Review and future perspectives. *Minerals Engineering*, vol. 144, p. 106025
- Qi, C, Guo, L., Wu, Y., Zhang, Q, Chen, Q., 2022. Stability evaluation of layered backfill considering filling interval, backfill strength and creep behaviour. *Minerals*, vol. 12, no. 2, p. 271
- Qiu, J., Guo, Z, Yang, L., Jiang, H., Zhao, Y., 2020. Effect of packing density and water film thickness on the fluidity behaviour of cemented paste backfill. *Powder Technology*, vol. 359, pp. 27 – 35

Rankine, R.M., 2004. The geotechnical characterisation and stability analysis of BHP Billiton's Cannington Mine paste fill. PhD Thesis, James Cook University, Townsville, Australia

Raut, L., Constatin, M., Petre, I., Raduly, M., Radu, N., Gurban., Doni, M., Alexandrescu, E. Nicolae, C., Jecu, L., 2022. Highlighting bacteria with calcifying abilities suitable to improve mortar properties. *Materials*, vol. 15, no, 19, p. 6829

Rawlings, C.A., Phillips, H.R., 2001. Reduction of mine heat loads. Proceedings of the 7th International Mine Ventilation Congress, pp. 381 – 389, Huainan and Xi'an, China, 17 – 22 June 2001

Roylance, D., 2001. Stress-strain curves. Cambridge: Department of Materials Science and Engineering, Massachusetts Institute of Technology

Ruijie, W., Chong, L., Jinhai, X., Lijin, P., 2018. Development and verification of large deformation model considering stiffness deterioration and shear dilation effect in FLAC<sup>3D</sup>. *International Journal of Mining Science and Technology*, vol. 28, pp. 959 – 967

Sadrossadat, E., Basarir, H., Luo, G., Karrech, A., Durham, R., Fourie, A., Elchalakani, M., 2020. Multi-objective mixture design of cemented paste backfill using particle swarm optimisation algorithm. *Minerals Engineering*, vol. 153, p. 106385

SANS (South African National Standards) 2011. SANS 3001: Civil Engineering Test Methods, GR10. Pretoria: South African Bureau of Standards

Sasa, Z., Gaofeng, R., Xinping, L., Yujie, W., Ashraf, M., 2019. Proportion optimization of cemented tailing backfill and its interaction mechanism with rocks in room and pillar stope: A case study. *International Journal of Electrical Engineering and Education*, DOI: [10.1177/0020720919844208](https://doi.org/10.1177/0020720919844208)

Selah, H., Eskander, S., 2020. Innovative cement-based materials for environmental protection and restoration. In: Samui, P. (Eds.), *New Materials in Civil Engineering*, pp. 613 – 641, Butterworth-Heinemann

Shunman, C., Wu, A., Yiming, W., Wei, W., 2021. Coupled effects of curing stress and curing temperature on mechanical and physical properties of cemented paste backfill. *Construction and Building Materials*, vol. 273, p. 121746

- Simon, D., Grabinsky, M., Bawden, W., 2011. Effect of polycarboxylated acrylic acid polymer-based superplasticizer on cemented paste backfill. Proceedings of the Canadian Geotechnical Conference, 2 – 6 October 2011, Ontario, Canada
- Sellgren, A., Addie, G., Whitlock, L., 2005. Technical-economical feasibility of using centrifugal pumps in high-density thickened tailings slurry systems. Proceedings of the International Seminar on Paste and Thickened Tailings, Paste 2005, pp. 195 – 204, Australian Centre for Geomechanics, Perth
- Seneviratne, N. H., Fahey, M., Newson, T. A., Fujiyasu, Y., 1996. Numerical modelling of consolidation and evaporation of slurried mine tailings. International Journal of Numerical and Analytical Methods in Geomechanics, vol. 20, no. 9, pp. 647 – 671
- Sengani, F., Mulenga, F., 2020. A review on the application of particle finite element methods (PFEM) to cases of landslides, International Journal of Geotechnical Engineering, vol. 16, no. 3, pp. 367 – 381
- Sivakugan, N., Widisinghe, S., Wang, V., 2014. Vertical stress determination within backfilled mine stopes. International Journal of Geomechanics, vol. 14, no. 5, p. 06014011
- Sobhi, M.A., Li, L., 2017. Numerical investigation of the stresses in backfilled stopes overlying a sill mat. Journal of Rock Mechanics and Geotechnical Engineering, vol. 9, no. 3, pp. 490 – 501
- Suorineni, F.T., 2010. The stability graph after three decades in use: experiences and the way forward. International Journal of Mining, Reclamation and Environment, vol. 24, no. 4, pp 307 – 339
- Stacey, T.R., 2001. Best practice rock engineering handbook for "other" mines. The Safety in Mines Research Advisory Committee, Johannesburg, pp. 48 – 50
- Stewart, S. B. V., Forsyth, W. W., 1995. The Mathew's method for open stope design. CIM Bulletin, vol. 88, no. 992, pp. 45 – 53
- Tan, Y., Davide, E., Zhou, Y., Song, W., Meng, X., 2020. Long-term mechanical behavior and characteristics of cemented tailings backfill through impact loading. International Journal of Minerals, Metallurgy, and Materials, vol. 27, no. 2, p.140

- Tao, J., Yang, X., Ding, P., Li, X., Zhou, J., Lu, G., 2022. A fully coupled thermo-hydro-mechanical-chemical model for cemented backfill application in geothermal conditions. *Engineering Geology*, vol. 302, p. 106643
- Tariq, A., Yanful, E. K., 2013. A review of binders used in cemented paste tailings for underground and surface disposal practices. *Journal of Environmental Management*, vol. 131, pp. 138 – 149
- Tian, X., Fall, M., 2021. Non-isothermal evolution of mechanical properties, pore structure and self-desiccation of cemented paste backfill. *Construction and Building Materials*, vol. 297, p. 123657
- Trueman, R., Mawdsley, C., 2003. Predicting cave initiation and propagation. *CIM Bulletin*, vol. 96, no. 1071, pp. 54 – 59
- Veenstra, R.L., 2015. A methodology for predicting dilution of cemented paste backfill. In: Potvin, Y. (Eds.), *Proceedings of the International Seminar on Design Methods in Underground Mining. Design Methods 2015*, pp. 527 – 539, Australian Centre for Geomechanics, Perth
- Walske, M., McWilliam, H., Doherty, J., Fourie, A., 2015. The influence of curing temperatures and stress conditions on mechanical properties of cementing paste backfill. *Canadian Geotechnical Journal*, vol. 53, no. 1, pp. 148 – 161
- Wang, P., Li, H., Li, Y., Cheng, B., 2013. Stability analysis of backfilling in subsiding area and optimization of the stoping sequence. *Journal of Rock Mechanics and Geotechnical Engineering*, vol. 5, no. 6, pp. 478 – 485
- Wang, W., Lu, C., Yuan, G., Zhang, Y., 2017. Effects of pore water saturation on the mechanical properties of fly ash concrete. *Construction and Building Materials*, vol. 130, pp. 54 – 63
- Wang, Y., Cao, Y., Cui, L., Si, Z., Wang, H., 2020a. Effect of external sulfate attack on the mechanical behavior of cemented paste backfill. *Construction and Building Materials*, vol. 263, p. 120968
- Wang, J., Fu, J., Song, W., 2020b. Mechanical properties and microstructure of layered cemented paste backfill under triaxial cyclic loading and unloading. *Construction and Building Materials*, vol. 257, p. 119540

- Wang, J., Fu, J., Song, W., Zhang, Y., Wang, Y., 2020c. Mechanical behavior, acoustic emission properties and damage evolution of cemented paste backfill considering structural feature. *Construction and Building Materials*, vol. 261, p. 119958
- Wang, L., Li, Y., Wang, H., Cui, X., Wang, X., Lu, A., Gan, D., 2017. Weathering behavior and metal mobility of tailings under an extremely arid climate at Jinchuan Cu-Ni sulfide deposit, Western China. *Journal of Geochemical Exploration*, vol. 173, pp. 1 – 12
- Wang, J., Song, W., Cao, S., Tan, Y., 2019. Mechanical properties and failure modes of stratified backfill under triaxial cyclic loading and unloading. *International Journal of Mining Science and Technology*, vol. 29, no. 5, pp. 809 – 814
- Wang, S., Song, X., Wei, M., Liu, W., Wang, X., Ke, Y., Tao, T., 2021a. Strength characteristics and microstructure evolution of cemented tailings backfill with rice straw ash as an alternative binder. *Construction and Building Materials*, vol. 297, p. 123780
- Wang, H., Sun, X., Wang, J., Duan, Y., Zhang, C., Qiu, J, Guo, Z., 2021b. Effect of tailings fine content on the properties of cemented paste backfill from the perspective packing density. *Advances in Civil Engineering*, vol. 2021, p. 9947620
- Wang, R., Zeng, F., Li, L., 2021c. Stability analyses of side-exposed backfill considering mine depth and extraction of adjacent stope. *International Journal of Rock Mechanics and Mining Sciences*, vol. 142, p. 104735
- Wang, R., Zeng, F., Li, L., 2021d. Applicability of constitutive models to describing the compressibility of mining backfill: a comparative study. *Processes*, vol. 9, no. 12, p. 2139
- Wang, J., Zhang, C., Fu, J., Song, W., Zhang, Y., 2021e. Effect of water saturation on mechanical characteristics and damage behavior of cemented paste backfill. *Journal of Materials Research and Technology*, vol. 15, pp. 6624 – 6639
- Wang, Y, Wu, J., Ma., Yang, S., Yin, Q., Feng, F., 2022. Effect of aggregate size distribution and confining pressure on mechanical property and microstructure of cemented gangue backfill materials. *Advanced Powder Technology*, vol. 33, no. 8, p. 103686

- Wu, D., Fall, M., Cai, S. J., 2013. Coupling temperature, cement hydration and rheological behaviour of fresh cemented paste backfill. *Minerals Engineering*, vol. 42, pp. 76 – 87
- Wu, D., Fall, M., Cai, S., 2014. Numerical modelling of thermally and hydraulically coupled processes in hydrating cemented tailings backfill columns. *International Journal of Mining, Reclamation and Environment*, vol. 28, no. 3, pp 173 – 199
- Wu, J., Feng, M., Chen, Z., Mao, X., Han, G., Wang, Y., 2018. Particle size distribution effects on the strength characteristic of cemented paste backfill. *Minerals*, vol. 322, no. 8, p. 322
- Wu, D., Wang, Y., Qiu, Y., Zhang, J., Wan, Y., 2019. Determination of Mohr–Coulomb parameters from nonlinear strength criteria for 3d slopes. Article ID 6927654, DOI: [10.1155/2019/6927654](https://doi.org/10.1155/2019/6927654)
- Wu, D., Zhao, R., Xie, C., Liu, S., 2020. Effect of curing humidity on performance of cemented paste backfill. *International Journal of Minerals, Metallurgy and Materials*, vol. 27, pp 1046 – 1053
- Wu, W., Xu, W., Zuo, J., 2021. Effect of inclined interface angle on shear strength and deformation response of cemented paste backfill-rock under triaxial compression. *Construction and Building Materials*, vol. 279, p. 122478
- Xiu, Z., Wang, S., Ji, Y., Wang, F., Ren, F., 2022. Experimental study on the triaxial mechanical behaviors of the cemented paste backfill: Effect of curing time, drainage conditions and curing temperature. *Journal of Environmental Management*, vol. 301, p. 113828
- Xu, W., Tian, X., Cao, P., 2018a. Assessment of hydration process and mechanical properties of cemented paste backfill by electrical resistivity measurement. *Nondestructive Testing and Evaluation*, vol. 33, no. 2, pp. 198 – 212
- Xu, W., Cao, P., Tian, M., 2018b. Strength development and microstructure evolution of cemented tailings backfill containing different binder types and contents. *Minerals*, vol. 8, no. 4, p. 167
- Xu, W., Cao, Y., Liu, B., 2019a. Strength efficiency evaluation of cemented tailings backfill with different stratified structures. *Engineering Structures*, vol. 180, pp. 18 – 28



- Xu, W., Li, Q., Zhang, Y., 2019b. Influence of temperature on compressive strength, microstructure properties and failure pattern of fibre-reinforced cemented tailings backfill. *Construction and Building Materials*, vol. 222, pp. 776 – 785
- Xu, W., Liu, B., Wu, W., 2020. Strength and deformation behaviors of cemented tailings backfill under triaxial compression. *Journal of Central South University*, vol. 27, pp. 3531 – 3543
- Xu, W., Chen, W., Tian, M., Lijie, G., 2021. Effect of temperature on time-dependent rheological and compressive strength of fresh cemented paste backfill containing flocculants. *Construction and Building Materials*, vol. 267, p. 121038
- Xu, X., An, N., Fang, K., 2022. Experimental investigation into the temperature effect on the shear behavior of the fiber-reinforced interface between rock and cemented paste backfill. *Construction and Building Materials*, vol. 356, p. 129280
- Xue, G., Yilmaz, E., Song, W., Cao, S., 2019. Mechanical, flexural and microstructural properties of cement-tailings matrix composites: Effects of fibre type and dosage. *Composites Part B: Engineering*, vol. 172, pp. 131 – 142
- Xue, G., Yilmaz, E., Song, W., Cao, S., 2020. Fibre length effect on strength properties of polypropylene fiber reinforced cemented tailings backfill specimens with different sizes. *Construction and Building Materials*, vol. 241, p. 118113
- Yan, B., Jia, H., Yilmaz, E., Lai, X., Shan, P., Hou, C., 2022. Numerical study on microscale and macroscale strength behaviours of hardening cemented paste backfill. *Construction and Building Materials*, vol. 321, p. 126327
- Yang, Z., Zhai, S., Gao, Q., Li, M., 2015. Stability analysis of large-scale stope using stage subsequent filling mining method in Sijiyang iron mine. *Journal of Rock Mechanics and Geotechnical Engineering*, vol. 7, no.1, pp. 87 – 94
- Yang, P., Aubertin, M., 2017. A new solution to assess the required strength of mine backfill with a vertical exposure. *International Journal of Geomechanics*, vol. 17, no. 10, p. 04017084
- Yang, L., Xu, W., Yilmaz, E., Wang, Q., Q, J., 2020. A combined experimental and numerical study on the triaxial and dynamic compression behaviour of cemented tailings backfill. *Engineering Structures*, vol. 219, p. 110957

- Yi, X., Ma, G., Fourie, A., 2015. Compressive behaviour of fibre-reinforced cemented paste backfill. *Geotextiles and Geomembranes*, vol. 43, no. 3, pp. 207 – 215
- Yilmaz, E., Benzaazoua, M., Belem, T., Bussiere, B., 2009. Effect of curing under pressure on compressive strength development of cemented paste backfill. *Minerals Engineering*, vol. 22, no. 9 – 10, pp. 772 – 785
- Yilmaz, E., Belem, T., Bussiere, B., Benzaanzoua, M., 2011. Relationships between microstructural properties and compressive strength of consolidated and unconsolidated cemented paste backfills. *Cement and Concrete Composites*, vol. 33, no. 6, pp. 702 – 715
- Yilmaz, E., Belem, T., Benzaazoua, M., 2014. Effects of curing and stress conditions on hydromechanical, geotechnical and geochemical properties of cemented paste backfill. *Engineering Geology*, vol. 168, pp. 23 – 37
- Yilmaz, E., Belem, T., Benzaazoua, M., 2015. Specimen size effect on strength behavior of cemented paste backfills subjected to different placement conditions. *Engineering Geology*, vol. 185, pp. 52 – 62
- Yilmaz, E., Ercikdi, B., 2016. Predicting the uniaxial compressive strength of cemented paste backfill from ultrasonic pulse velocity test. *Nondestructive Testing and Evaluation*, vol. 31, no. 3, pp. 247 – 266
- Yilmaz, E., 2018. Stope depth effect on field behaviour and performance of cemented paste backfills. *International Journal of Mining, Reclamation and Environment*, vol. 32, no. 4, pp. 273 – 296
- Yin, S., Wu, A., Hu, K., Wang, Y., Zhang, Y., 2012. The effect of solid components on the rheological and mechanical properties of cemented paste backfill. *Minerals Engineering*, vol. 35, pp. 61 – 66
- Yin, S., Shao, Y., Wu, A., Wang, Z., Yang, L., 2020. Assessment of expansion and strength properties of sulfidic cemented paste backfill cored from deep underground stopes. *Construction and Building Materials*, vol. 230, p. 116983
- Yu, Q., Chen, X., Dai, Z., Nei, L., Soltanian, M.R., 2018. Numerical investigation of stress distributions in stope backfills. *Periodica Polytechnica Civil Engineering*, vol. 62, no. 2, pp. 533 – 538

Zeng, F., Li, L., Aubertin, M., Simon, R., 2022. Implementation of the non-associated elastoplastic MSDP<sub>u</sub> model in FLAC3D and application for stress analysis of backfilled stopes. *Processes*, vol. 10, no. 6, p. 1130

Zhang, J., Deng, H., Taheri, A., Deng, J., Ke, B., 2018. Effects of superplasticizer on the hydration, consistency, and strength development of cemented paste backfill. *Minerals*, vol. 8, no. 9, p. 381

Zhang, C., Tan, Y., Zhang, K., Zhang, C., Song, W., 2021. Rheological parameters and transport characteristics of fresh cement tailings backfill slurry in an underground iron mine. *Advances in Civil Engineering*. Vol. 2021, p. 7916244

Zhang, C., Fu, J., Song, W., Kang, M., Li, T., Wang, N., 2022. Analysis on mechanical behavior and failure characteristics of layered cemented paste backfill (LCPB) under triaxial compression. *Construction and Building Materials*, vol. 324, p. 126631

Zhang, C., Wang, J., Song, W., Fu, J., 2022. Pore structure, mechanical behavior and damage evolution of cemented paste backfill. *Journal of Materials and Research and Technology*, vol. 17, pp. 2864 – 2874

Zhang, X., Muyan, X., Liu, L., Huan, C., Zhao, Y., Qi, C., Song, K., 2020a. Experimental study on thermal and mechanical properties of cemented paste backfill with phase change material, vol. 9, no. 2, pp. 2164 – 2175

Zhang, S., Ren, F., Guo, Z., Qiu, J., Ding, H., 2020b. Strength and deformation behavior of cemented foam backfill in sub-zero environment. *Journal of Materials Research and Technology*, vol. 9, no. 4, pp. 9219 – 9231

Zhang, S., Zhao, Y., Ding, H., Qiu, J., Hou, C., 2021. Effect of sodium chloride concentration and pre-curing time on the properties of cemented paste backfill in a sub-zero environment. *Journal of Cleaner Production*, vol. 283, p. 125310

Zhang, Z., Li, J., 2021. Experimental investigation on strength and failure characteristics of cemented paste backfill. *Frontiers in Materials*, vol. 8, p. 792561

Zhao, L., 2021. Numerical investigation on the mechanical behaviour of combined backfill-rock structure with KCC model. *Construction and Building Materials*, vol. 283, p. 122782

- Zhao, Y., Taheri, A., Karakus, M., Deng, A., Guo, L., 2021a. The effect of curing under applied stress on the mechanical performance of cemented paste backfill. *Minerals*, vol. 11, no. 10, p. 1107
- Zhao, Y., Qiu, J., Ma, Z., 2021b. Temperature-dependent rheological, mechanical and hydration properties of cement paste blended with iron tailings. *Powder Technology*, vol. 381, pp. 82 – 91
- Zhao, K., Huang, M., Zhou, Y., Yan, Y., Wan, W., Ning, F., He, Z., Wang, J., 2022. Synergistic deformation in a combination of cemented paste backfill and rocks. *Construction and Building Materials*, vol. 317, p. 125943
- Zheng, J., Guo, L., Sun, X., Li, W., Jia, Q., 2018. Study on the strength development of cemented backfill body from lead-zinc mine tailings with sulphide. *Advances in Materials Science and Engineering*, vol. 2018, p. 7278014
- Zheng, J., Sun, X., Guo, L., Zhang, S., Chen, J., 2019. Strength and hydration products of cemented paste backfill from sulphide-rich tailings using reactive MgO-activated slag as a binder. *Construction and Building Materials*, vol. 203, pp. 111 – 119
- Zhou, X., Fourie, A., Qi, C., 2019. An analytical solution for evaluating the safety of an exposed face in a paste backfill stope incorporating the arching phenomenon. *International Journal of Minerals, Metallurgy, and Materials*, vol. 26, no. 10, pp. 1206 – 1216
- Zhou, X., Hu, S., Zhang, G., Li, J., Xuan, D., Gao, W., 2019. Experimental investigation and mathematical strength model study on the mechanical properties of cemented paste backfill. *Construction and Building Materials*, vol. 226, pp. 524 – 533
- Zou, D., Sahito, W., 2004. Suitability of mine tailings for shotcrete as a ground support. *Canadian Journal of Civil Engineering*, vol. 31, no. 4, pp. 632 – 636

## APPENDICES

### Appendix A: Ethical clearance certificate



#### UNISA SCHOOL OF ENGINEERING (SOE) RESEARCH ETHICS REVIEW COMMITTEE

08 March 2022

Dear Mrs Nhleko Monique Chiloane

**Decision: Ethics Approval from  
08/03/2022 to 08/03/2026  
[No humans involved]**

ERC Reference # :  
2022/CSET/SOE/008  
Name : Mrs Nhleko Monique  
Chiloane  
Student #: 11661895  
Staff #: N/A

**Researcher(s):** Name: Mrs Nhleko Monique  
E-mail address: chilonm@unisa.ac.za  
Telephone #: 083 611 4376

**Supervisor (s):** Name: Prof Francois Mulenga  
E-mail address: mulenf@unisa.ac.za  
Telephone #: 011 471 2692

**Co-Supervisor (s):** Name: Dr Fhatuwani Sengani  
E-mail address: Fhatuwani.sengani@ul.ac.za  
Telephone #: 015 268 3036

**Working title of research:**

**The effect of stope height and binder-to-tailing ratio on the strength development of cemented tailing backfill**

**Qualification:** PhD

Thank you for the application for research ethics clearance by the Unisa School of Engineering Research Ethics Review Committee for the above mentioned research. Ethics approval is granted for 5 years.

*The negligible risk application was reviewed by the School of Engineering Research*



University of South Africa  
Pretoria Street, Muckleneuk Ridge, City of Tshwane  
PO Box 392 UNISA, 0003 South Africa  
Telephone: +27 12 429 3111. Facsimile: +27 12 429 4150  
www.unisa.ac.za

## Appendix B: Sample of calculations from Chapter 7



research.pdf

## Appendix C Laboratory results

Batch one 2.5 C/T ratio 7 DAYS			
one layer	UCS	Strain (%)	Strain (mm)
sample 1	5.44	1	0.010
sample 2	4.96	2	0.020
sample 3	5.31	1	0.010
average	<b>5.23666667</b>	<b>1.33333333</b>	0.013
		E	<b>392.750</b>
2 layers	UCS	Strain	
sample 1	5	2	
sample 2	4.78	3	
sample 3	4.27	3	
average	<b>4.68333333</b>	<b>2.66666667</b>	
		E	<b>175.625</b>
3 layers	UCS	Strain	
	4.24	2.67	
	4.53	1.34	
	4.64	2.67	
Average	<b>4.47</b>	<b>2.22666667</b>	
		E	<b>200.749</b>

	First batch				2 Layers				3 layers			
1 Layer	UCS	Strain		2 Layers	UCS	Strain		3 layers	UCS	Strain		
sample 1	7.85	2.02	0.020202	sample 1	6.09	4.04	0.040404	1	6.34	2.01	0.020134	
sample 2	7.22	2.02	0.020202	2	6.59	3.00	0.03	2	5.99	1.34	0.013423	
sample 3	7.73	1.01	0.010101	3	7.18	2.02	0.020202	3	7.06	2.68	0.026846	
Average	<b>7.60</b>	<b>1.68</b>	<b>0.02</b>	average	<b>6.62</b>	<b>3.02</b>	<b>0.03</b>	Average	<b>6.46</b>	<b>2.01</b>	<b>0.02</b>	
E	<b>451.4</b>			E	<b>219.2574</b>			E	<b>320.963</b>			
1 Layer	2nd batch				2 Layers				3 Layers			
sample 1	7.87	1.01	0.010101	sample 1	6.95	2.00	0.02	sample 1	7.28	2.01	0.020134	
sample 2	9.65	1.01	0.010101	sample 2	7.17	2.04	0.020408	sample 2	6.76	2.00	0.02	
sample 3	8.76	1.01	0.010101	sample 3	7.18	2.04	0.020408	sample 3	7.40	2.00	0.02	
Average	<b>8.76</b>	<b>1.01</b>	<b>0.010101</b>	Average	<b>7.10</b>	<b>2.03</b>	0.020272	Average	<b>7.15</b>	<b>2.00</b>	<b>0.02</b>	
E	<b>867</b>			E	<b>350.3523</b>			E	<b>356.5541</b>			

first batch	21 days		
no of layers	UCS	Strain	E
1 layer	8.535	0.01	853.5
2 layers	7.553333	0.03	251.7778
3 layers	7.266667	0.02	363.3333
second batch			
no of layers	UCS (MPa)	Strain	E
1 layer	10.11333	0.01	1011.333
2 layers	7.8	0.030303	257.4
3 layers	7.4	0.026667	277.5

first batch	28 days		
no of layer	UCS	Strain	E
1 layer	9.193333	0.002	4596.667
2 layers	7.635	0.02	381.750
3 layers	8.616296	0.01	861.630
second batch			
no of layer	UCS	Strain	E
1 layer	10.69882	0.002	5349.411
2 layers	7.77	0.02	388.500
3 layers	8.955556	0.006667	1343.333

UCS	Strain	E	UCS	Strain	E	UCS
5.236667	0.002787	462.0588	6.313333	0.216667	315.6667	7.2
4.683333	0.026767	175.625	5.11	3.673401	139.1082	6.1
4.47	0.022267	200.7485	4.713333	2.222222	212.1	6.9
UCS (MPa) Strain E UCS (MPa) Strain E						
7.599327	0.016835	451.4	8.757576	1.01	867	10
6.20685	0.030202	205.5111	7.102381	2.027211	350.3523	9.8
6.462342	0.020134	320.963	7.163311	2.004474	357.3661	9.8
UCS Strain E UCS (MPa) Strain E						
8.535	0.01	853.5	10.11333	0.01	1011.333	12
7.553333	0.03	251.7778	7.8	0.030303	257.4	11.6
7.266667	0.02	363.3333	7.4	0.026667	277.5	12.4
UCS Strain E UCS Strain E						
9.193333	0.002	4596.667	10.69882	0.002	5349.411	15.7
7.635	0.02	381.75	7.77	0.02	388.5	12.8
8.616296	0.01	861.6296	8.955556	0.000667	1343.333	13.7

## Appendix D Data for the damage model

Time (days)	One layer	Two layers	Three layers
7	5.2	4.7	4.5
Calculated	5.1	4.5	4.4
14	7.6	6.6	6.5
calculated	7.470	6.430	6.380
21	8.535	6.900	7.267
Calculated	8.480	6.680	6.970
28	9.193	7.770	8.616
Calculated	8.960	7.580	8.240
error factor	2.61	3.49	0.89
	1.70	2.87	1.27
	0.64	3.19	4.08
	2.54	2.45	4.37

Parameters	<i>One layer</i>		<i>Two layers</i>		<i>Three layers</i>	
	<i>m</i>	<i>x</i>	<i>m</i>	<i>x</i>	<i>m</i>	<i>x</i>
<b>7 days</b>	54.67	0.014	3.433	0.028	2.327	0.03
<b>14 days</b>	5.808	0.027	156.038	0.031	158.066	0.021
<b>21 days</b>	243.357	0.095	162.59	0.031	218.456	0.021
<b>28 days</b>	1379.638	0.0021	217.692	0.021	528.107	0.011



## Appendix E Numerical analysis data for stress-strain graph

Four layers		Three-layers		Two-layers		One layer	
Stress	Strain	Stress	Strain	Stress	Strain	Stress	Strain
7	0.00008	7	0.00007	15	0.00008	16	0.00007
20	0.00013	20	0.0001	30	0.00011	35	0.00009
34	0.00016	34	0.00013	40	0.00012	55	0.00011
45	0.00019	45	0.00015	58	0.00014	85	0.00013
55	0.00021	57	0.00017	70	0.00016	115	0.00015
65	0.00024	68	0.00019	84	0.00018	135	0.00016
75	0.00027	75	0.0002	98	0.0002	160	0.00019
100	0.00031	86	0.00022	121	0.00023	180	0.00021
105	0.00032	110	0.00025	133	0.00025	189	0.00023
128	0.00035	128	0.00029	141.401	0.00031	212	0.00026
132	0.00038	133.732	0.00032	141.401	0.00035	233.555	0.00029
131	0.00041	133.732	0.00036	141.401	0.0004	233.555	0.00032
128	0.00042	128	0.0004	143.401	0.00042	230	0.00035
119	0.00044	121	0.00043	143.401	0.00045	228	0.00037
114	0.00048	112	0.00046	142	0.00046	226	0.00039
119	0.0005	112	0.00049	140	0.00049	224	0.00042
123	0.00055	121	0.000510	142.401	0.00052	222	0.00044
128	0.00058	128	0.000530	142.401	0.00055	220	0.00046
128	0.00061	132	0.00055	143.401	0.00057	218	0.00049
120	0.00063	133.732	0.00058	143.401	0.00059	210	0.00051

## Appendix F Solution to Equation (5.20)



Equation 5.20.pdf